

ALMA MATER STUDIORUM - UNIVERSITÀ DI
BOLOGNA

DOTTORATO DI RICERCA IN
GEOFISICA

Ciclo XXVI

Settore Concorsuale di afferenza: 04/A4

Settore Scientifico disciplinare: GEO / 10

EVALUATION OF SLOPE STABILITY
UNDER WATER AND SEISMIC LOAD
THROUGH THE MINIMUM LITHOSTATIC
DEVIATION METHOD

Presentata da : Maria Ausilia Paparo

Coordinatore Dottorato

Prof. Michele Dragoni

Relatore

Prof. Stefano Tinti

ESAME FINALE ANNO 2014

Declaration of Authorship

I, Maria Ausilia Paparo, declare that this thesis titled, 'Evaluation of slope stability under water and seismic load through the Minimum Lithostatic Deviation method' and the work presented in it are my own. I confirm that:

- This work was done wholly or mainly while in candidature for a research degree at this University.
- Where any part of this thesis has previously been submitted for a degree or any other qualification at this University or any other institution, this has been clearly stated.
- Where I have consulted the published work of others, this is always clearly attributed.
- Where I have quoted from the work of others, the source is always given. With the exception of such quotations, this thesis is entirely my own work.
- I have acknowledged all main sources of help.
- Where the thesis is based on work done by myself jointly with others, I have made clear exactly what was done by others and what I have contributed myself.

Bologna, 17 Marzo 2014

Abstract

The work carried out during my PhD was focused on the study of the numerical and mathematical methods of the analysis of the stability of a slope, in particular on the Minimum Lithostatic Deviation (MLD) method, a variant of the Equilibrium Limit method.

This thesis is organized as follows:

Chapter 1 - This chapter illustrates the principal features of landslides and outlines the essential terminology used in this thesis.

Chapter 2 - In this chapter we illustrate the main mathematical concepts and formulas on which the limit equilibrium method is based. In addition to the MLD method, we delineate, in broad line, even the most common methods used in the engineering and geological field, such as the methods of Fellenius, Bishop, Janbu and Morgenstern and Price. The purpose of this chapter is to highlight the differences between these methods and the MLD method.

Chapter 3 - In this chapter we test the limit equilibrium methods discussed in chapter two on a real case: the well-known Vajont landslide. The choice of this particular case is justified by the huge amount of available data obtained since the area was selected to build the dam, until the

night when the landslide occurred. This event is a dark page of the history of Italy due to the high number of victims, but even it is important on a global scale for the awareness about the risk assessment associated with landslides and the increase of the in-site inspections and the thorough investigations regarding the stability of slopes. Within the chapter, using the MLD method we go back, step by step, to the conditions that led to the landslide, focusing on the main features that destabilized the slope: the combination of clay layers and heavy rainfall that led to an increase of the pore pressure; after the rapid lowering of the basin level, the hydrostatic conditions failed causing the detachment of the mass.

Chapter 4 - In this chapter we show the application of the MLD method on two Norwegian cases provided by the Norwegian Geotechnical Institute of Oslo. The cases are selected in function of the dip angle: the first is a typical flat profile of the Norwegian continental margin, it is located off shore the Lofoten and Vesterålen peninsula and the inclination is about 4° - 5° . The second is a deep profile of the main scarp of the famous Storegga landslide: the inclination is about 30° and it is located on the edge of the continental shelf of Norway. The main goal is to obtain the present equilibrium conditions of both sites by means of the MLD method and to compare the results with the Morgenstern and Price method implemented into the software GeoStudio2012. Furthermore we make assessment on conditions that could destabilize the profile.

Chapter 5 - In the last chapter we used the MLD method to make a critical analysis of Taylor's and Mikalowski's stability charts.

The stability charts are a tool used in the engineering and geological field to assess the stability conditions of the slope. Usually they are used on slopes of geotechnical interest (dikes and embankment). Our purpose was first to understand if this tool can be exploited also to study the stability of slope of geophysical interest, and second, more important, to investigate the adequacy and accuracy of the stability charts.

Contents

Declaration of Authorship	1
Abstract	3
Contents	6
List of Figures	8
List of Tables	13
Abbreviations and Symbols	14
1 The Landslides	16
1.1 Material Classification	16
1.2 Landslide classification	18
1.3 Landslide features	20
2 The limit equilibrium method	22
2.1 Limit Equilibrium Method	22
2.1.1 Mohr-Coulomb criterion	25
2.2 Ordinary method	27
2.3 Method of Bishop	28
2.3.1 Bishop's simplified method	28
2.3.2 Bishop's generalized method	30
2.4 Method of Janbu	32
2.4.1 Janbu simplified method	33
2.4.2 Janbu generalized method	34
2.5 Method of Morgenstern and Price	34
2.6 Method of the Minimum Lithostatic Deviation	35
3 The Vajont	39
3.1 The Vajont case	39
3.1.1 Geological structure	40
3.1.2 Hydrostatic condition	41

3.2	Analysis of stability	43
3.2.1	Application of classical and MLD methods	45
3.2.2	Analysis of stability with the MLD method	47
3.3	Conclusions	51
4	Analysis of two Norwegian sites	52
4.1	The Lofoten and Vesterålen analysis	53
4.1.1	Homogeneous slope and circular surface without piezometric and basin levels	55
4.1.2	Homogeneous slope and circular surface with piezometric and basin levels	58
4.1.3	Homogeneous slope and circular surface changing the parameter r_u	59
4.1.4	Homogeneous slope and circular surface with seismic load	61
4.1.5	Summary of Lofoten and Vesterålen analysis	64
4.2	The Storegga Headwall analysis	65
4.2.1	Summary of the analysis of the Storegga headwall	73
5	The Stability Charts	74
5.1	Taylor's stability charts	75
5.1.1	The geometry of the slip surface	81
5.1.2	Analysis of Taylor's and Baker's charts	84
5.2	Michalowski's stability charts	92
5.2.1	Numerical results	94
5.3	Conclusion	100
A		102
A.1	The equilibrium equations	102
A.1.1	The horizontal equilibrium equation	103
A.1.2	The vertical equilibrium equation	107
A.2	The moment equation	109
B		115
B.1	The Ordinary method	115
B.2	The Bishop's method	117
	Bibliography	119
	Acknowledgements	125

List of Figures

1.1	The essential parts of a landslide, Varnes (1978)	21
2.1	(a) Geometric representation of a landslide body, delimited by two curves, $z_1(x)$ and $z_2(x)$, which identify the upper and lower surface; z_3 represents the upper surface of the reservoir; the end points of these two curves coincide $z_1(x_i) = z_2(x_i)$ and $z_1(x_f) = z_2(x_f)$. (b) Geometric representation of a single slice: dl_1 and dl_3 are the two vertical sides, while dl_2 and dl_4 are the upper and lower sides, characterized by the inclinations β and α with respect to the x-axis; dx is the width of the slice.	23
3.1	Daily precipitation (in mm) from 1960 to 1963 (Hendron and Patton, 1985)	41
3.2	Monthly precipitation (in mm) from 1960 to 1963 (Hendron and Patton, 1985)	42
3.3	Rate of movement from 1960 to 1963 (Hendron and Patton, 1985)	42
3.4	Map of the Vajont slide: the red line is the failure scar and the blue lines represent some discontinuity set along the crown. The main scarp can be divided in two parts: the upper one is composed mainly of micritic and cherty limestone with thin intercalation of green clay and marl, while the part near the deposit is constituted of alluvial and glacial deposits. The yellow arrow indicates the position of the dam.	43
3.5	Longitudinal profile 1 of Vajont (Paparo et al., 2013)	44
3.6	Longitudinal profile 2 of Vajont (Paparo et al., 2013)	44
3.7	Comparison of inter-slice forces $E(x)$ obtained by means of all different methods: all methods satisfy the boundary conditions, but the generalized Bishop method (see the second chapter) (Paparo et al., 2013).	46
3.8	Comparison of inter-slice forces $X(x)$ obtained by means of different methods: all methods satisfy the boundary conditions with the exception of the generalized Bishop method (Paparo et al., 2013).	46
3.9	Comparison of the moment $A(X)$ obtained by means of different methods: in this case the Bishop and Janbu methods do not satisfy the boundary conditions, while the <i>MLD</i> and <i>M&P</i> methods do (Paparo et al., 2013).	47
3.10	Values of F resulting from the different methods.	47

3.11	Trend of F for different cases for profile 1: in case 1 reservoir level increases; in case 2 reservoir and piezometric levels increase; in case 3 reservoir and piezometric levels increase and the cohesion varies from 20KPa to 10 KPa; in case 4 reservoir and piezometric levels increase and the angle of friction varies from 22° to 17° ; in case 5 reservoir and piezometric levels increase and the cohesion and the angle of friction vary. The red line highlights the critical condition of F equal to 1	49
3.12	Trend of F for different cases from 1 to 5 for the profile 2: see fig. 3.12	50
3.13	Trend of F for case 6, profile 1: we keep the reservoir level constant at 710 m and we raise the piezometric level to 790 m (Hendron and Patton, 1985), reaching the limit equilibrium. Lowering the level basin from 710 m to 700 m triggers the instability (red dot)	50
3.14	Trend of F for case 6, profile 2: as in profile 1, we keep the reservoir level constant at 710 m and we raise the piezometric level to 790 m (Hendron and Patton, 1985), reaching the limit equilibrium. Lowering the level basin from 710 m to 700 m triggers the instability (red dot).	51
4.1	Map of the Scandinavian Peninsula	53
4.2	Lofoten and Vesterålen area: the red square indicates the analyzed zone	54
4.3	Profile used to compare the results obtained by means of the (<i>M&P</i>) and the <i>MLD</i> methods. The red line indicates the post-landslide surface, while the dark brown line indicates the reconstructed top surface of the slope. The light brown line indicates a thin layer of overconsolidated clay	54
4.4	Cross-section and partition of the slide into 50 slices. The green line is the top of the slide and the red line is the trial circular slip surface	56
4.5	Comparison of the functions $X(x)$ obtained by means of the Morgenstern and Price and <i>MLD</i> methods	56
4.6	Comparison of the functions $E(x)$ obtained by means of the Morgenstern and Price and <i>MLD</i> methods	57
4.7	Comparison of the functions $P(x)$ obtained by means of the Morgenstern and Price and <i>MLD</i> methods	57
4.8	Comparison of the functions $S(x)$ obtained by means of the the Morgenstern and Price and <i>MLD</i> methods	58
4.9	Trend of the safety factor as a function of the basin level: in this case the level of the sea and the piezometric level are coincident	59
4.10	Trend of the safety factor as a function of the parameter r_u for a submerged slope	61
4.11	Trend of the safety factor as a function of the seismic coefficients k_h and k_v for a submerged slope.	61
4.12	Trend of the safety factor as a function of the seismic coefficients and the excess of pore pressure	62
4.13	Seismic Hazard Map of the Norway (USGS site: http://earthquake.usgs.gov/earthquakes/world/norway/gshap.php)	63
4.14	Acceleration time series of Nihanni: $k_h = 0.155$	64
4.15	Acceleration time series of Imperial Valley: $k_h = 0.204$	64

4.16	Acceleration time series of Friuli: $k_h = 0.220$	65
4.17	Map of the Scandinavian Peninsula.	66
4.18	Storegga area	66
4.19	Section of the headwall of Storegga and average angles of the slope	67
4.20	Trend of the safety factor obtained by changing the circular surface, that are numbered according to increasing radiuses. The blue and red highlighted points indicate the smallest value of F for the two methods: $F_{M\&P} = 1.59$ and $F_{MLD} = 1.17$	68
4.21	Circular trial surfaces: the red line is the critical surface for <i>M&P</i> , the blue dashed line is the circular surface n.102 with $F=1.17$ (<i>MLD</i>)	68
4.22	Comparison of the pore pressure $u(x)$	69
4.23	Comparison of the weight for every single slice	69
4.24	Normal pressure of the basin above the slope	70
4.25	Comparison of the functions $E(x)$	70
4.26	Comparison of the functions $X(x)$	71
4.27	Comparison of the functions $E(x)$ with simplified <i>MLD</i>	71
4.28	Comparison of the functions $X(x)$ with simplified <i>MLD</i>	72
4.29	Typical cross-section of the headwall of Storegga: the succession of layers is composed by glacial till (grey lines) and marine clay (brown lines). The blue and red lines represent the trial slip surface that passes through the clay layers.	73
5.1	Example of 2-D slope: simplification of a sliding body for building stability charts: H is the height, β is the inclination of the slope.	75
5.2	Taylor's stability chart for uniform slopes. The dashed lines are the Taylor's curve corresponding to a given value of ϕ_m . Colored lines delimit regions within which the critical slip surface takes a specific shape: between blue and green lines, slip surfaces are midpoint circles; between green and red lines, slip surfaces are deep toe circles and under the red line slip surfaces are shallow toe circles.	80
5.3	Shallow toe circle: $z_1(x)$ and $z_2(x)$ define respectively the bottom and upper curves of the landslide. R is the radius of the circular slip surface with center coordinates (X_c, Z_c) . H and β are the height and the inclination of the slope. T is the landslide toe, η is the inclination of the chord connecting the start- and end-point of the slip surface and 2ξ is the central angle of the chord AT (Baker, 2003).	81
5.4	Deep toe circles: see fig. 5.3 , (Baker, 2003).	82
5.5	Base circle: see fig. 5.3. The particularity in this failure mode is in the end-point C that lies beyond the toe. The friction circle shows how much the center of the sliding surface is moved with respect to the center of the slope M , (Baker, 2003)	82

- 5.6 The function $\xi(\beta, \phi_m)$. The dashed lines are the Baker's curves corresponding to different values of ϕ_m . The colored lines bound regions with different shapes of the critical slip surface: between blue and green lines one finds base or midpoint circles, between green and red lines one finds deep toe circles, while under the red line one finds shallow toe circles 83
- 5.7 The function $\eta(\beta, \phi_m)$: see fig 5.6 84
- 5.8 Circular rupture surfaces investigated for stability calculations. The gray points are the circumference centers. The center and the arc corresponding to the lowest value of F are in red. Notice that horizontal and vertical scales are different. 85
- 5.9 Comparison of the MLD results, colored points, with the curves of Taylor. The cases analyzed are in correspondence of $\beta = 30^\circ, 60^\circ$. We show that the resulting points do not fall exactly on the curves, also if they follow the curve's trend. The discrepancy grows with the increase of the inclination, from about 5% for $\beta = 30^\circ$, up to 10% for $\beta = 60^\circ$ 87
- 5.10 The three configurations with $\beta = 30^\circ$. The three marked points indicate the centers found through Baker's charts. The big rectangles (violet, blue and orange) are the areas explored to find MLD slip circle centers; the little rectangles (blue, red and green) are the zones swept to refine the MLD research. The last areas are shown in fig. 5.11 88
- 5.11 Rectangles (blue, red and green) shown in fig. 5.10. Each point in the rectangle represents the center coordinates of a set of trial slip surfaces with different radiuses. The value of F is the lowest value computed according to the MLD method. The first rectangle is for $H = 10 m$, the second for $H = 75 m$ and the third for $H = 130 m$. The slip surfaces are similar to the ones obtained by Taylor. The values of F are slightly smaller than those obtained with Taylor's chart 90
- 5.12 Numbers of stability obtained from values of F_{MLD} (blue dots) vs. $N_{sTaylor}$ (red dots). The cases explored are six: three corresponding to $\gamma = 15 KN/m^3$ and three corresponding to $\gamma = 25 KN/m^3$ and all sharing the same Taylor's $N_{sTaylor}$. The largest discrepancy is about 8% 91
- 5.13 Stability charts of Michalowski for unsaturated soil 93
- 5.14 Mikalowski's curve of $\beta = 15^\circ$ compared with our results (red crosses). Discrepancies range from 5% to 15%. 95
- 5.15 Mikalowski's curve of $\beta = 30^\circ$. The same as for Fig. 5.14 96
- 5.16 Mikalowski's curve of $\beta = 45^\circ$. Discrepancies range from 5% to 10%. 97
- 5.17 Mikalowski's curve of $\beta = 60^\circ$. Discrepancies range from 5% to 20%. 98
- 5.18 Chart of $\beta = 30^\circ$. Six different cases (red points) that should all correspond to the same point (blue dot) in Mikalowski's diagram. Discrepancies range from 2% to about 10%. 99
- 5.19 Chart of $\beta = 30^\circ$. We have selected 4 points and for each one we have defined 2 cases, varying the weight $\gamma = [15$ (green points) -25 (red points)] KN/m^3 . It seems that for a given value of the weight, the points are located along their own curve, that however is not the Michalowski curve. Discrepancies range from 5% to 15%. 100

5.20 Chart of $\beta = 60^\circ$ with horizontal seismic load. Discrepancies range from 5% to 35%.	101
---	-----

List of Tables

1.1	Landslide material types	17
1.2	The classification system of Varnes (1978)	20
3.1	Geotechnical parameters of section 1 (Hendron and Patton, 1985) . . .	45
3.2	Geotechnical parameters of section 2 (Hendron and Patton, 1985) . . .	45
4.1	Geotechnical parameters of the sediments	55
5.1	Ranges of the geotechnical and geometrical parameters used to study Michalowski's stability charts	94

Abbreviations and Symbols

2-D	Two dimensional
α	Slope of base of slice
a.s.l.	above sea level
β	Slope of the top of slice
δ	Coefficient of the minimum lithostatic deviation
BG	Bishop Generalized
BS	Bishop Simplified
c	Cohesion
c_m	Mobilized cohesion
D	Basin pressure
dl_1, dl_2, dl_3, dl_4	The four sides of the slice
dx	Width of the slice
F	Factor of safety
γ_w	Unit weight of the water
JG	Janbu Generalized
JS	Janbu Simplified
k_v and k_h	Vertical and horizontal coefficients of seismic load
λ and $f(x)$	Variable components which satisfy both force and moment equations in the <i>M&P</i> method
λ_1 and λ_2	Unknown coefficients of the Fourier sine expansion of the MLD method
LE	Limit Equilibrium
N_s	Stability number
M&P	Morgenstern and Price

MLD	Minimum Lithostatic Deviation
M_w	Moment magnitude
P	Normal stress
P'	Effective normal stress
PGA	Peak Ground Acceleration
q	Free coefficient of the Fourier sine expansion of the MLD method
r_u	Coefficient of the pore pressure
S	Shear stress
S_{max}	Shear stress mobilized
u	Pore pressure
ϕ	Friction angle
ϕ_m	Mobilized friction angle
x_i and x_f	Ends of the slope in x-axis
$z_1(x)$	Bottom curve that delimits the slide body
$z_2(x)$	Top curve that delimits the slide body

Chapter 1

The Landslides

In this first chapter, we introduce the most important soil characteristics connected with the landslide process. With the word *Landslide* we identify the ground movements, off-shore, coastal or onshore, when the equilibrium conditions of forces that act in the soil do not hold anymore: the state passes from stable to unstable. The principal conditions that generate this transition are linked to the soil morphology, the hydrostatic condition and the situation at the top surface of the mass such as vegetation or civil works. In the following sections we describe, under the geological point of view, what is a Landslide.

1.1 Material Classification

A landslide has often a heterogeneous composition which can be described by means of parameters characterizing the ground material and its mechanical properties, e.g. permeability, stiffness, strength. There are two principal types of ground:

- **Rock:** a hard and stiff material of igneous, sedimentary, or metamorphic origin, with a generally homogeneous matrix.
- **Soil:** a consolidation of solid particles, that can be of the same type or an aggregate of minerals and rocks. The soil class is divided in two subclasses based on

MATERIAL	CHARACTERISTIC
Rock	Strong Weak
Clay	Stiff Soft Sensitive
Mud	Liquid
Earth	Plastic
Silt Sand Gravel Boulders	Dry or Saturated or Partially saturated
Debris	Dry or Saturated or Partially saturated
Peat	
Ice	

TABLE 1.1: Landslide material types

their granular size: the **earth**, in which most of the particles are smaller than 2 mm diameter; the **debris** where the particles are larger than 2 mm.

Furthermore, the ground is not a compact and uniform solid, but there are some voids, called pores, that can be filled with air or water and their presence affects the mechanical response to stress, as will be shown in the chapter of this thesis where we treat the Vajont landslide case. The soil is said permeable if the water of interconnected voids can flow from points of high energy to points of low energy and the permeability is the coefficient that describes the capability of a material to be passed through by a fluid. The knowledge of permeability is important for the understanding of the mechanics and the hydraulic conditions that can influence the stable state of the slope.

Depending on the quantity of water, the ground can be:

- **Dry**, no wetness;
- **Moist**, contains some water, inside the connected pores, free to move; the mass is similar to a plastic solid;
- **Wet**, contains enough water to behave in part like a liquid, and water flows away from it;

- **Very wet:** contains enough water to flow like a liquid.

The water inside the ground produces the pressure that could destabilize the equilibrium conditions. It takes the name of pore pressure u and it is defined, according with the Bernulli's equation, as

$$u = \gamma_w h \quad (1.1)$$

where γ_w is the unit weight of water and h is the height to which a column of liquid rises against gravity. In the chapters 3 and 4 we show in depth this soil characteristic.

1.2 Landslide classification

There are different ways to classify landslides. The prevalent one is the classification of Varnes Varnes (1954, 1978), based on the movement and on the ground types (rock or debris). The classification system has frequently been reworked and improved because landsliding is a very complex process that is hard to classify into specific categories. Until today there are 32 different landslide types, evaluated on the basis of the geotechnical and geological features of the soil and in accordance with the behaviour of the mass movement (Highland and Bobrowsky, 2008, Hungr et al., 2013).

Based on the mass movement the following classes can be distinguished:

- **Fall:** a sudden movement of mass such as rocks that detaches from steep slopes. It occurs next to the fractures and discontinuities of the soil, in which the gravitational component has a significant influence, though it is caused by earthquakes and excess of water inside.
- **Topple:** a rotation of the mass around a fulcrum; the slope angle has to be high, between 45° and 90° and the movement is mainly driven by the gravity force, while the crack could be triggered by the saturation of fractures with water or by earthquakes.

- **Slide:** most movements of soil fit in this class. It is divided into two subclasses, the rotational slide and the translation slide. The first has a concave sliding surface and the movement occurs around a rotational axis. Usual for plastic rocks and homogeneous slope, it could be affected by the water pore pressure or the action of earthquakes.

The second subclass has a planar surface where the soil moves like a unique block. It is typical for homogeneous or stratified rocks where the upper part of the slope is marked out by the tension cracks.

- **Lateral spreading:** this is typical for very gentle slopes or flat terrain, subject to a stratification. When the soil becomes saturated, the pore pressure increases under layers with a low permeability and the sediments (usually sands and silts) are transformed from a solid into a liquefied state. The state transformation can be generated by an earthquake or also artificially.
- **Flow:** A lot of landslide types belong to this category, which frequently is divided in many subclasses. The most important are the *Debris flow* (caused by intense surface-water flow, composed by a large proportion of silt and sand), the *Earthflow* (the characteristic shape is an hourglass and it occurs in fine materials under saturated and dry conditions), the *Mudflow* (a particular earthflow that occurs when the material is wet and the movement is sudden), and the *Creep* (an imperceptible slow movement, in which the permanent deformation, for example due to seasonal changes, produces a small shear failure).
- **Complex:** the last category contains all landslide types that cannot be included in one of the preceding categories. Usually a combination of two or more types, like slide-earthflow or slide-debris, are used to describe the main features of one particular landslide.

Another way to describe the landslide type is based on the movement velocity, but this case is not deepened here for it does not fit the purpose of this work.

Movement type	Rock	Debris	Earth
Fall	Rock fall	Debris fall	Earth fall
Topple	Rock topple	Debris topple	Earth topple
Rotational sliding	Rock slump	Debris slump	Earth slump
Translational sliding	Rock slide	Debris slide	Earth slide
Lateral spreading	Rock spread		Earth spread
Flow	Rock creep	Talus flow Debris flow Debris avalanche Solifluction Soil creep	Dry sand flow Wet sand flow Quick clay flow Earth flow Rapid earth flow Loess flow
Complex	Rock slide-debris avalanche	Cambering, valley bulging	Earth slump-earth flow

TABLE 1.2: The classification system of Varnes (1978)

1.3 Landslide features

Within a particular landslide two essential parts are distinguished: the **sliding zone**, in which the mobilized material is located at lower altitudes than originally, and the **accumulation area**, in which the slide material lies down. Furthermore it is important to identify the principal parts of a landslide (figure 1.1):

- **Crown:** The upper edge that remains steady and is adjacent to the highest parts of the main scarp.
- **Main scarp:** the exposed slide surface caused by the movement of displaced material. It is often steep, but depends on the fracture mechanism of the landslide.
- **Head:** The upper parts of the landslide.
- **Minor scarp:** The lateral surfaces produced by differential movements that are visible along the landslide flanks.
- **Main body:** The part of the ground that slides on the slip surface.
- **Toe:** The lower part of the landslide that usually has a curved shape due to the amassed material of a landslide.
- **Foot:** The portion of the ground that has moved beyond the toe.

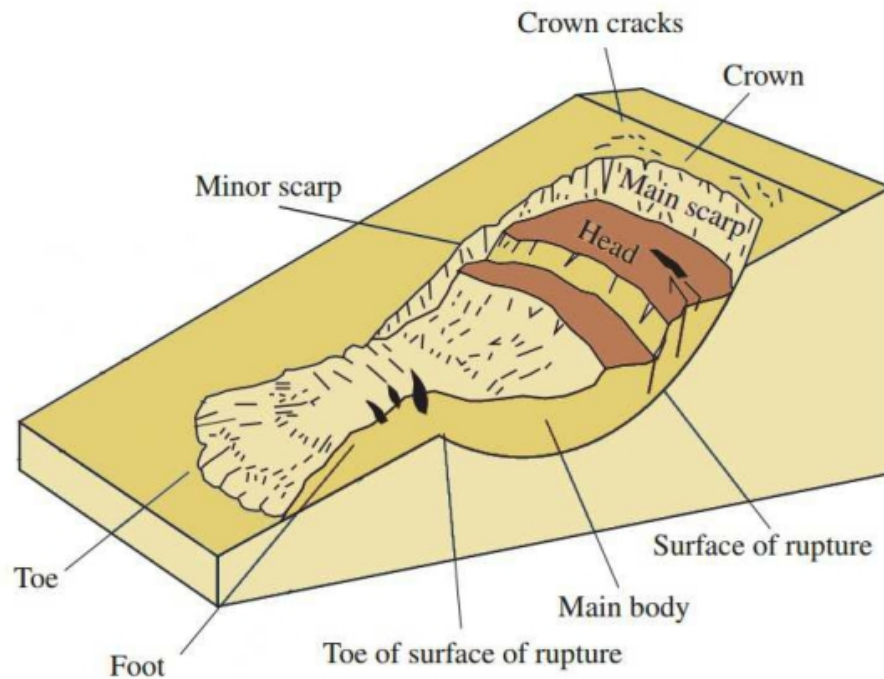


FIGURE 1.1: The essential parts of a landslide, Varnes (1978)

- **Surface of rupture:** The surface that defines the rupture zone and along which the ground slides; it is usually called slip surface.
- **Toe of the rupture's surface:** Intersection between the lower part of the slip surface and the ground level before of the landslide

Other important pieces of information are the dimension and the volume of the landslide. In our work we have considered the problem of stability in 2 dimensions, imposing a unitary width, and, as we show in the next chapter, the dip angle and the height have a fundamental role on the stability of a slope.

Chapter 2

The limit equilibrium method

Investigating the soil stability means to analyse the contributions of the forces acting on a slope and to examine the conditions of balance. The problem of slope stability is an important topic in the geological and engineering field, in continuous evolution, especially due to the continuous increase of computing power over time. The limit equilibrium is one of the main methods used for the stability analysis and the goal of this chapter is to show a 2-D mathematical elaboration of conventional methods found in the literature, in agreement with the formulation of the Minimum Lithostatic Deviation (*MLD*) method (Tinti and Manucci, 2006, 2008).

Some parts of the methods and their mathematical developments exposed in this chapter and in the Appendix A and B are the reworking of unpublished reports developed by Tinti and Manucci.

2.1 Limit Equilibrium Method

In our analysis, we consider a 2-D problem: the functions $z_1(x)$ and $z_2(x)$, where x indicates a point in the range $[x_i, x_f]$, represent the bottom and the top curves that delimit the slide body. Studying the equilibrium means analysing all the forces acting on the slope. To ease, the body is divided into an arbitrary number of vertical slices of width

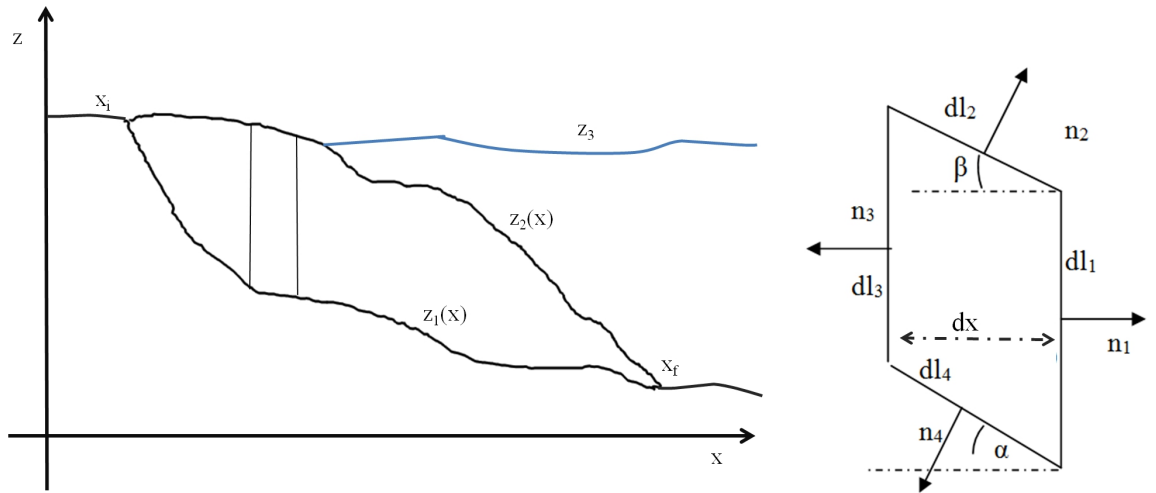


FIGURE 2.1: (a) Geometric representation of a landslide body, delimited by two curves, $z_1(x)$ and $z_2(x)$, which identify the upper and lower surface; z_3 represents the upper surface of the reservoir; the end points of these two curves coincide $z_1(x_i) = z_2(x_i)$ and $z_1(x_f) = z_2(x_f)$. (b) Geometric representation of a single slice: dl_1 and dl_3 are the two vertical sides, while dl_2 and dl_4 are the upper and lower sides, characterized by the inclinations β and α with respect to the x -axis; dx is the width of the slice.

dx (Fellenius, 1936). The horizontal component of the inter-slice forces $E(x)$ is defined as

$$E(x) = \int_{z_1(x)}^{z_2(x)} \sigma_{xx} dx \quad (2.1)$$

and the vertical component $X(x)$ is

$$X(x) = \int_{z_1(x)}^{z_2(x)} \sigma_{xz} dx \quad (2.2)$$

where σ is the matrix of stresses.

Since the thickness is zero at the beginning and at the end points of the slope, fig. 2.1, i.e.

$$z_2(x_i) = z_1(x_i) \quad (2.3)$$

$$z_2(x_f) = z_1(x_f) \quad (2.4)$$

the boundary conditions are

$$E(x_i) = E(x_f) = X(x_i) = X(x_f) = 0 \quad (2.5)$$

Supposing that the slope, in addition to the weight, may be subject to seismic and hydrostatic load, we express the horizontal equilibrium (see appendix A.1.1) as

$$\frac{dE}{dx} + P \tan \alpha - S - D \tan \beta + k_h w = 0 \quad (2.6)$$

and the vertical equilibrium (see appendix A.1.2) as

$$\frac{dX}{dx} + P + S \tan \alpha - D - (1 + k_v) w = 0 \quad (2.7)$$

where P and S are respectively the normal and shear stress along the bottom $z_1(x)$, linked to the slide material, D is the hydrostatic load of the water on the upper surface $z_2(x)$. The coefficients k_h and k_v express the ratio of the seismic load components to the magnitude of the gravitational acceleration.

In addition to the above two equations, we have a third equilibrium relationship relative to the mechanical moment, because the equilibrium of a body requires that all forces and all moments are equal to zero. There are different manners to express the moment of forces. In our method we impose the equilibrium of each slice, because, this condition is implied when the entire body is in equilibrium. The moment equation in our notations (see appendix A.2) is

$$\frac{dA}{dx} - z_1 \frac{dE}{dx} - X - (z_2 - z_1) D \tan \beta + k_h (z_B - z_1) w = 0 \quad (2.8)$$

where $A(x)$ is the moment of first order of the normal stress (Tinti and Manucci, 2006, 2008). In the next sections we show the relationships used in the classical methods to express the total moment and the equilibrium of the slope.

2.1.1 Mohr-Coulomb criterion

Another important relationship that takes into account the geotechnical property and the capacity of rupture of a soil is the failure criterion of Mohr-Coulomb (Nadai, 1950). It relates the normal and shear stress acting on the sliding surface as follows

$$S_{max} = c + P' \tan \phi \quad (2.9)$$

where S_{max} is the shear strength of the material, P' is the effective normal stress, c is the cohesion coefficient of the soil, ϕ is the friction angle. When the soil is saturated, the total normal stress at a point is the sum of the effective stress and pore water pressure u

$$P = P' + u \quad (2.10)$$

and the expression 2.9 becomes

$$S_{max} = c + (P - u) \tan \phi \quad (2.11)$$

The coefficient

$$F = \frac{S_{max}}{S} \quad (2.12)$$

represents a new parameter called Factor of Safety (F), whose value determines the equilibrium conditions of the slope: since S_{max} is the maximum value of shear stress beyond which the soil breaks and S is the effective shear stress acting along the slide

surface, when the value of F is less than 1 the slope is unstable, because the shear stress is greater than the limit value sustainable by the slope.

If we want to write 2.9 with 2.12

$$F = \frac{c + (P - u) \tan \phi}{S} \quad (2.13)$$

To simplify we pose

$$c^* = c - u \tan \phi \quad (2.14)$$

and the 2.13 becomes

$$F = \frac{c^* + P \tan \phi}{S} \quad (2.15)$$

It is worth pointing out that, even if we have four equations, 2.6, 2.7, 2.8, 2.15, and their boundary conditions that define the problem, the number of unknowns $E(x)$, $X(x)$, $S(x)$, $P(x)$ and F is greater than the number of equations and the system is underdetermined with an infinite number of solutions. So we must impose additional relations that allow us to uniquely solve the system.

Starting from this base, in the last century a large number of techniques have been developed, the most famous of which are the methods of Fellenius, Bishop, Janbu, Morgenstern and Price, Spencer, Sarma, and others, that we call classical methods.

In this chapter we show the most important and famous methods that today are still in use for the analysis of stability, and in the next chapter we compare the results obtained by the classical methods and the Minimum Lithostatic Deviation method.

2.2 Ordinary method

The Ordinary method is the first analytical and easiest method and was developed by Fellenius, (Fellenius, 1927, 1936). The Limit Equilibrium (*LE*) is introduced to study the stability of an infinite homogeneous slope, imposing that the inter-slice forces $E(x)$ e $X(x)$ have to be equal to zero

$$E(x) = X(x) = 0 \quad (2.16)$$

Solving the system of the two horizontal and vertical equations without external loads, the expression of F is

$$F = \frac{c^* + w \cos \alpha \tan \phi}{w \sin \alpha} \quad (2.17)$$

that represents an exactly and trivial solution for the slope. For a dry soil without cohesion it simplifies to

$$F = \frac{\tan \phi}{\tan \alpha} \quad (2.18)$$

The equation 2.18 indicates that the slope is stable, ($F > 1$), if the angle of slip is less than the friction angle, while it is unstable when the slip angle is greater than the friction angle.

In our work we calculate the value of F for a slope with a generic slip surface. The conditions are 2.16, but the system is composed of the equations 2.6 and 2.7. Without examining this in depth (more details can be found in the Appendix B.1), the final expression of F for a generic slip surface is:

$$F_O = \frac{\int_{x_i}^{x_f} [(x_O - x) \tan \alpha + (z_O - z_1)] (c^* + P \tan \phi) dx}{\int_{x_i}^{x_f} \left\{ -(x_O - x) [P - D - (1 + k_v)w] + (z_O - z_1) [P \tan \alpha - D \tan \beta + k_h w] + (z_2 - z_1) D \tan \beta - k_h w (z_B - z_1) \right\} dx} \quad (2.19)$$

that in case of a circular sliding surface simplifies to :

$$F_O = \frac{\int_{x_i}^{x_f} \left\{ \frac{c^*}{\cos \alpha} + [D \tan \beta \sin \alpha - k_h w \sin \alpha + [D + (1 + k_v)w] \cos \alpha] \tan \phi \right\} dx}{\int_{x_i}^{x_f} \{ [D + (1 + k_v)w] \sin \alpha - D \tan \beta \cos \alpha + k_h w \cos \alpha \} dx} \quad (2.20)$$

The subscript O indicates the Ordinary method and although it represents a simple solution, it is often used to make a quick evaluation of F and it is also the basis of the method of Bishop, as we will show in the following section.

2.3 Method of Bishop

The method of Bishop proposes a refined solution to the Ordinary method, because the inter-slice forces are not null and takes into account the equilibrium of moment (Bishop, 1955).

To solve the problem, this method needs the boundary conditions and, depending on the choice of these, there are two different methods of Bishop, called simplified and generalized methods. In both cases, the trial surface for the original method has to be circular, but in our work we formulate the Bishop theory even for a generic slide surface.

2.3.1 Bishop's simplified method

The simplified method assumes that the horizontal force is null. Solving the system between 2.7 and 2.9, and imposing that $X = 0$, P is calculated as

$$P = \frac{D - (k_v + 1)w - \frac{c^*}{F} \tan \alpha}{\left(1 + \frac{\tan \phi \tan \alpha}{F}\right)} \quad (2.21)$$

This allows one to find an expression for F , making the integral along the range $[x_i, x_f]$

$$F = \frac{\int_{x_i}^{x_f} [(x_O - x) \tan \alpha + (z_O - z_1)] (c^* + P \tan \phi) dx}{\int_{x_i}^{x_f} \left\{ -(x_O - x) [P - D - (1 + k_v)w] + (z_O - z_1) [P \tan \alpha - D \tan \beta + k_h w] + (z_2 - z_1) D \tan \beta - k_h w (z_B - z_1) \right\} dx} \quad (2.22)$$

The 2.22 can be applied to any type of slide surfaces. The simplification for a circular surface is

$$F = \frac{\int_{x_i}^{x_f} \frac{c^* + P \tan \phi}{\cos \alpha} dx}{\int_{x_i}^{x_f} [D + (1 + k_v)w] \sin \alpha dx + \frac{1}{R} \int_{x_i}^{x_f} [D \tan \beta (z_2 - z_O) - k_h w (z_B - z_O)] dx} \quad (2.23)$$

where R is the radius of the circular slip surface and z_0 is the vertical coordinate of the circular surface center (see Appendix B.2). Within the expression 2.21 there is F , and this suggests to use an iterative method to search for a solution, that is:

$$F_{BS}^n = \frac{\int_{x_i}^{x_f} \frac{1}{\cos \alpha} \left[c^* + \frac{D - (k_v + 1)w - \frac{c^*}{F^{n-1}} \tan \alpha}{\left(1 + \frac{\tan \phi \tan \alpha}{F^{n-1}}\right)} \tan \phi \right] dx}{\int_{x_i}^{x_f} [D + (1 + k_v)w] \sin \alpha dx + \frac{1}{R} \int_{x_i}^{x_f} [D \tan \beta (z_2 - z_O) - k_h w (z_B - z_O)] dx} \quad (2.24)$$

where BS is used to denote the Bishop's simplified method and n is the number of iterations: for convention the initial value of F

$$F^0 = F_O \quad (2.25)$$

coincides with the value of the Ordinary method, but it can be any initial value. For each n we find a new value of F_{BS} that, during the next step, is placed as the new F^n . If the process converges the solution could be expressed as

$$F_{BS}^n = \lim_{n \rightarrow \infty} F^{n-1} \quad (2.26)$$

but in practice a few iterations are sufficient to find the limit value.

2.3.2 Bishop's generalized method

The simplified method does not take into account all of the equations that define the problem, and therefore it does not satisfy all the boundary conditions. One attempt to overcome this drawback is to impose a dependency between the horizontal and vertical components of the inter-slice forces

$$X(x) = \lambda f(x)E(x) \quad (2.27)$$

where the function $\lambda f(x)$ is used to force the expression of X to satisfy the boundary conditions. This method has a double iteration cycle, the first is an internal loop and is identical to that shown to find the value of F_{BS} , while the second cycle concerns the relation

$$X^m(x) = \lambda f(x)E^{m-1}(x) \quad (2.28)$$

where m represents is the index of the external iteration. We assume the initial value $E^0 = 0$ and $\lambda f(x) = \tan \theta$, where θ is the angle between the inter-slice forces and the x -axis. The expression of P is

$$P_{n-1}^m(x) = \frac{D - \frac{dX^m}{dx} + (k_v + 1)w - \frac{c^*}{F_{n-1}^m} \tan \alpha}{\left(1 + \frac{\tan \phi \tan \alpha}{F_{n-1}^m}\right)} \quad (2.29)$$

and S is

$$S_{n-1}^m(x) = \frac{c^* + P^m \tan \phi}{F_{n-1}^m} \quad (2.30)$$

For a circular slip surface we have

$$F_n^m = \frac{\int_{x_i}^{x_f} \frac{1}{\cos \alpha} \left\{ \frac{c^* + D - \frac{dX^m}{dx} + (1 + k_v)w}{1 + \frac{\tan \phi \tan \alpha}{F_{n-1}^m}} \tan \phi \right\} dx}{\int_{x_i}^{x_f} [D + (1 + k_v)w] \sin \alpha dx + \frac{1}{R} \int_{x_i}^{x_f} [D \tan \beta (z_2 - z_0) - k_h w (z_B - z_0)] dx} \quad (2.31)$$

where F_0^m is the initial value that can be obtained through the Ordinary method or can be an arbitrary initial value as

$$F_0^m = \eta F_O^m \quad (2.32)$$

where η is an appropriate coefficient. The iteration finishes when F_n^m reaches a limit value

$$|F^m - F^{m+1}| < \varepsilon \quad (2.33)$$

where ε is sufficiently small.

In our work we have calculated the 2.31 for a generic slip surface, and without expliciting the 2.29, we have

$$F_n^m = \frac{\int_{x_i}^{x_f} [(x_0 - x) \tan \alpha + (z_0 - z_1(x))] (c^* + P_{n-1}^m) dx}{\int_{x_i}^{x_f} \left\{ [(x - x_0) + (z_0 - z_1(x)) \tan \alpha] P_{n-1}^m + (x_0 - x) [D + (1 + k_v)w] - (z_0 - z_2(x)) D \tan \beta + k_h w (z_0 - z_B(x)) \right\} dx} \quad (2.34)$$

2.4 Method of Janbu

The method of Janbu is similar to Bishop's, because it takes into account two of the three equations of the equilibrium problem, but the choice is on the horizontal and vertical forces expressions, overlooking the moment equation (Janbu, 1954).

In particular, Janbu takes into account the global horizontal equilibrium

$$E(x_f) - E(x_i) = \int_{x_i}^{x_f} \left\{ S - P \tan \alpha + D \tan \beta - k_h w \right\} dx = 0 \quad (2.35)$$

where

$$P = \frac{D - \frac{dX}{dx} + (k_v + 1)w - \frac{c^*}{F} \tan \alpha}{\left(1 + \frac{\tan \phi \tan \alpha}{F} \right)} \quad (2.36)$$

and

$$S = \frac{c^* + \frac{D - \frac{dX}{dx} + (k_v + 1)w - \frac{c^*}{F} \tan \alpha}{\left(1 + \frac{\tan \phi \tan \alpha}{F} \right)} \tan \phi}{F} \quad (2.37)$$

Imposing that F is a parameter, its value is

$$F = \frac{\int_{x_i}^{x_f} \left\{ c^* + \frac{D - \frac{dX}{dx} + (k_v + 1)w - \frac{c^*}{F} \tan \alpha}{\left(1 + \frac{\tan \phi \tan \alpha}{F}\right)} \tan \phi \right\} dx}{\int_{x_i}^{x_f} \left\{ \frac{D - \frac{dX}{dx} + (k_v + 1)w - \frac{c^*}{F} \tan \alpha}{\left(1 + \frac{\tan \phi \tan \alpha}{F}\right)} \tan \alpha - D \tan \beta + k_h w \right\} dx} \quad (2.38)$$

We see that 2.38 leads to an expression of F in terms of other unknowns, i.e. X and F itself. So, depending of the initial assumptions, it is classified as simplified or generalized.

2.4.1 Janbu simplified method

In the Janbu simplified method, the additional condition is

$$X = 0 \quad (2.39)$$

everywhere and with an iterative method it obtains the Factor of Safety assuming the initial value of F equal to F_0 . The result is

$$F_{JS}^n = \frac{\int_{x_i}^{x_f} \left\{ c^* + \frac{D + (k_v + 1)w - \frac{c^*}{F^{n-1}} \tan \alpha}{\left(1 + \frac{\tan \phi \tan \alpha}{F^{n-1}}\right)} \tan \phi \right\} dx}{\int_{x_i}^{x_f} \left\{ \frac{D + (k_v + 1)w - \frac{c^*}{F^{n-1}} \tan \alpha}{\left(1 + \frac{\tan \phi \tan \alpha}{F^{n-1}}\right)} \tan \alpha - D \tan \beta + k_h w \right\} dx} \quad (2.40)$$

and for a converging process leading to

$$F_{JS}^n = \lim_{n \rightarrow \infty} F^{n-1} \quad (2.41)$$

the iterations stop when the difference between two consecutive solutions has magnitude smaller than a given small number ε .

2.4.2 Janbu generalized method

In the same way as with the Bishop's generalized method, the Janbu generalized method imposes the relationship between the functions E and X equal to 2.27. With a double iteration in m and n , the solution is

$$F_{nJG}^m = \frac{\int_{x_i}^{x_f} \left\{ c^* + \frac{D - \frac{dX^m}{dx} + (k_v + 1)w - \frac{c^*}{F_{n-1}^m} \tan \alpha}{\left(1 + \frac{\tan \phi \tan \alpha}{F_{n-1}^m}\right)} \tan \phi \right\} dx}{\int_{x_i}^{x_f} \left\{ \frac{D - \frac{dX^m}{dx} + (k_v + 1)w - \frac{c^*}{F_{n-1}^m} \tan \alpha}{\left(1 + \frac{\tan \phi \tan \alpha}{F_{n-1}^m}\right)} \tan \alpha - D \tan \beta + k_h w \right\} dx} \quad (2.42)$$

and the iteration finishes when the value of F_{JG} gets sufficiently close to its own limit value.

The fundamental difference between the Bishop and the Janbu methods is in the slip surface used: in the first one, originally, it has to be circular (with our modification it can be used also for a generic slip surface), while the second method can be used for any slip surface.

2.5 Method of Morgenstern and Price

Morgenstern and Price developed a method that satisfies all the three equations and all the boundary conditions of the equilibrium problem. They improve the Bishop and the Janbu methods, combining them to find a solution for F . They keep the relation between the inter-slice forces

$$X(x) = \lambda f(x)E(x) \quad (2.43)$$

as viewed in Bishop and Janbu methods, but they allow the function $f(x)$ to assume different shapes. One of the more used is the half-sine function. Varying λ within an initial range, they find for each value of λ , two independent solutions of F from the expressions 2.34 and 2.42. In this way one can draw two curves, satisfying respectively the moment and the forces equilibrium. The solution for F is the value that coincides with the intersection of the two curves, (Fredlund, 1974, Fredlund and Krahn, 1977, Morgenstern and Price, 1965, 1967).

2.6 Method of the Minimum Lithostatic Deviation

The *MLD* method brings a new way of solving the *LE* problem, starting from the concept that the solution to the problem in its original formulation is not unique. In the *MLD* approach F is considered a known parameter. It has been already stressed that the *LE* system of equations is underdetermined and therefore there are infinite values of F that solve the problem. The *MLD* method introduces a criterion to identify the solution that best solves the equilibrium conditions of the body. In the *MLD* method $X(x)$ is a Fourier sine expansion truncated to the third term

$$X(x, \lambda; F, q) = q \sin \left[\frac{\pi (x - x_i)}{L} \right] + \lambda_1 \sin \left[\frac{2\pi (x - x_i)}{L} \right] + \lambda_2 \sin \left[\frac{3\pi (x - x_i)}{L} \right] \quad (2.44)$$

where q is a free parameter and λ_1 and λ_2 are unknown parameters. The choice to truncate the series to the third term is related to the performance of the code. Tests were conducted by using up to six terms: the end result is an exponential increase of the number of combinations to be analysed (and consequently a radical increase of the time spent by the program to complete the calculations), and since results change only in the fourth decimal place of the safety factor, the inclusion of more terms is not justified (Paparo, 2010). The boundary conditions for $X(x)$ are automatically satisfied.

On combining the vertical equilibrium equation with the Mohr-Coulomb criterion, we can derive the expressions for P

$$P(x, \lambda; F, q) = \frac{\frac{\pi}{L} \left\{ q \cos \left[\frac{\pi (x - x_i)}{L} \right] + 2\lambda_1 \cos \left[\frac{2\pi (x - x_i)}{L} \right] + 3\lambda_2 \cos \left[\frac{3\pi (x - x_i)}{L} \right] \right\}}{1 + \frac{\tan \alpha \tan \phi}{F}} \quad (2.45)$$

and for S

$$S(x, \lambda; F, q) = \frac{c^*}{F} + \frac{\frac{\pi}{L} \left\{ q \cos \left[\frac{\pi (x - x_i)}{L} \right] + 2\lambda_1 \cos \left[\frac{2\pi (x - x_i)}{L} \right] + 3\lambda_2 \cos \left[\frac{3\pi (x - x_i)}{L} \right] \right\}}{F \left(1 + \frac{\tan \alpha \tan \phi}{F} \right)} \tan \phi \quad (2.46)$$

After some mathematical manipulations one can further derive the expressions for the functions

$$E = (x, \lambda; q, F) = \frac{\pi}{L} q \int_{x_i}^x H \cos \left[\frac{\pi(x - x_i)}{L} \right] dx' + \frac{2\pi}{L} \lambda_1 \int_{x_i}^x H \cos \left[\frac{2\pi(x - x_i)}{L} \right] dx' + \frac{3\pi}{L} \lambda_2 \int_{x_i}^x H \cos \left[\frac{3\pi(x - x_i)}{L} \right] dx' + \int_{x_i}^x g(x; F) dx' \quad (2.47)$$

and

$$\begin{aligned}
A(x, \lambda_1, \lambda_2; q, F) = & \frac{L}{\pi} \left\{ q \left(1 - \cos \left[\frac{\pi(x-x_i)}{L} \right] \right) + \frac{1}{2} \lambda_1 \left(1 - \cos \left[\frac{2\pi(x-x_i)}{L} \right] \right) + \right. \\
& \left. \frac{1}{3} \lambda_2 \left(1 - \cos \left[\frac{2\pi(x-x_i)}{L} \right] \right) \right\} - \int_{x_i}^x (1+k_v) H(x; F) w(x) z_1(x) dx' - \\
& \int_{x_i}^x D H(x; F) z_1(x) dx' + \int_{x_i}^x H(x; F) z_1(x) \frac{d}{dx} X(x, \lambda_1, \lambda_2; q) dx' + \\
& \int_{x_i}^x D \tan \beta(x) z_2(x) dx' - \int_{x_i}^x k_h w(x) z_b(x) dx' \quad (2.48)
\end{aligned}$$

By imposing the boundary conditions for $E(x)$ and $A(x)$, we obtain two equations where everything is known, except the coefficients λ_1 and λ_2 . This is an algebraic system of two equations in two unknowns that can be solved. Finally, knowing the values of λ_1 and λ_2 , we can obtain all the expressions previously defined for each point of the slide. In this case the searching of the solution is carried out in a space of configurations that depends on the number of the trial values of q , ($2imax$), and of the trial safety factor F , (NF). The formula which gives the total number of configurations that are analyzed is

$$n = (NF + 1)(2imax + 1) \quad (2.49)$$

So how do we choose the right solution?

The *MLD* method introduces the new parameter called Lithostatic Deviation defined as

$$\delta = W^{-1} \left[\frac{1}{(x_f - x_i)} \int_{x_i}^{x_f} [E(X)^2 + X(x)^2] dx \right]^{\frac{1}{2}} \quad (2.50)$$

with

$$W = \frac{1}{(x_f - x_i)} \int_{x_i}^{x_f} w(x) dx \quad (2.51)$$

where δ is the average magnitude of the inter-slice forces normalized to the weight of the sliding mass. Notice that this parameter is equal to zero only if the functions $E(X)$ and $X(x)$ vanish everywhere, which is a condition that can be met only by a homogeneous uniform layer in lithostatic equilibrium on a constant slope. Therefore δ represents the value of the deviation from a state of lithostatic equilibrium, and then allows us to identify the state of equilibrium as the one which satisfies all the equilibrium equations and which in addition corresponds to the smallest value of δ . This was called the Minimum Lithostatic Deviation principle.

Chapter 3

The Vajont

In this chapter we show the results of applying the *MLD* method to the famous case of the Vajont landslide that occurred about fifty years ago, in the attempt of casting light on the causes that triggered this event and that led the slope to transit from stability to instability conditions. The analysis has been performed also by using the classical methods, mentioned in the previous chapter, and the results have been compared with those obtained by means of the *MLD* method. The choice of studying this case is linked to the complexity of the factors intervened in addition to the gravitational component, such as the pore pressure, the rise and decrease of the piezometric level, the stratigraphic sequence made of limestone and clay layers and the non-circular failure surface that has to be found along planes of weakness represented by clay beds (Paparo et al., 2013).

3.1 The Vajont case

The landslide of Vajont is one of the greatest catastrophes in Italy and occurred on October 9th, 1963: the mass detached from Mount Toc and flew into the reservoir at high speed, about 18 *m/s* (Zaniboni and Tinti, 2014, Zaniboni et al., 2013). It generated a water wave that totally destroyed a number of villages, including Longarone that turned out to be the most affected one. The end result is 1917 victims of which 1450

belonging to Longarone, 109 to Codissago and Castellavazzo, 158 to Erto and Casso and 200 employees, technicians and their families who were working on the dam.

In view of the large amount of data collected during the monitoring of the site since 1936, the year in which the Vajont site was selected for the construction of the dam, the case of Vajont is still today an important masterpiece for the study of stability, evolution and effects generated by a landslide.

3.1.1 Geological structure

The Vajont valley is positioned in the North of the Venetian Prealps and the torrent lined the gorge that runs along the valley axis with an *E – W* trending, eroded along a synclinal (Ghirotti, 1993, Giudici and Semenza, 1960, Semenza and Ghirotti, 2000): the widest part of the gorge is derived by the soil erosion during the Würmian glacialism and the deepest part during an intermediate or postglacial phase (Carli, 2011, Carloni and Mazzanti, 1964). The soil presents a complex structure of typical Jurassic-Cretaceous carbonate sequences where a succession of layers have been identified: the Jurassic sequence is composed of massive Vajont Limestone of the Fonzaso Formation and Ammonitico Rosso Formation, while the Cretaceous sequence is composed of the Soccher Limestone and the Scaglia Rossa Formation marl (Francese et al., 2013, Massironi et al., 2013).

The landslide involves the Soccher formation and the upper part of the Fonzaso limestone: this last zone is spaced by thin layers of clays (Genevois and M., 2005) and the presence of clay, as we will see later, plays a fundamental role in the slope stability. Unfortunately, for several years after the disaster, the presence of clay in the rock layers officially was not accepted (Broili, 1967, Müller, 1986), although many geological studies confirmed that the dolomitic limestone was fractured and a thin layer of clay was located along the slip surface (Rossi and Semenza, 1965, Semenza, 1965).

It was only through the studies conducted by Hendron and Patton (1985) that it was recognized the presence of clay and demonstrated its relevance among the causes and mechanisms that led to the landslide motion.

3.1.2 Hydrostatic condition

In addition to the geomorphological characteristics of soil, we must take into account the presence of water, not only as infiltration resulting from continuous lowering and raising of the dam basin, but also due to the persisting rainfalls that affected the area. Since 1961 the level of the water in the soil was measured by piezometers installed at different elevations (838, 860, 765, and 851 m) and borehole depths (220, 220, 140, and 180 m), and the precipitations were recorded by the station located in the town of Erto.

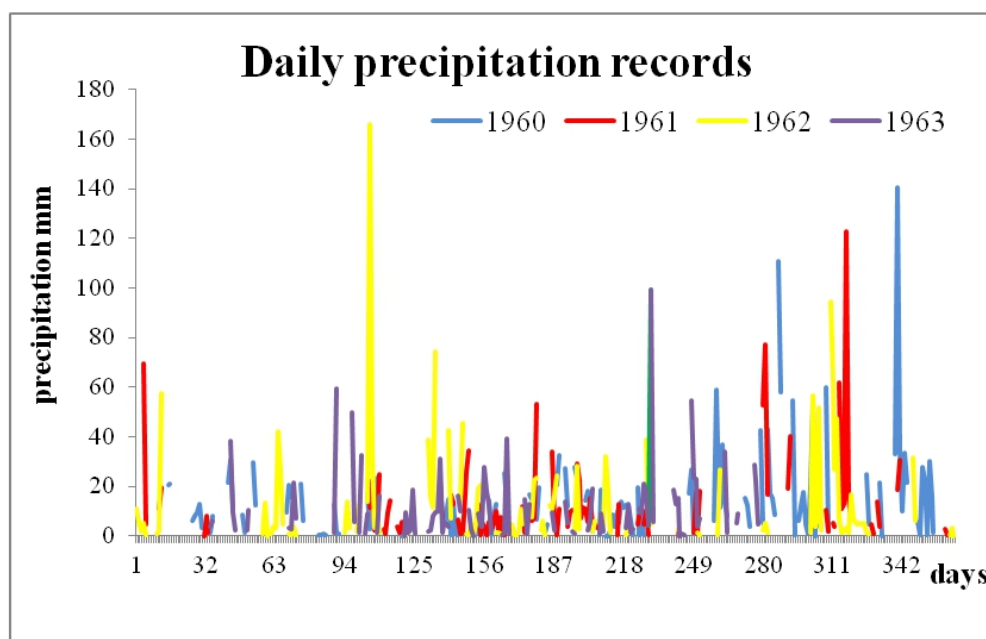


FIGURE 3.1: Daily precipitation (in mm) from 1960 to 1963 (Hendron and Patton, 1985)

The two phenomena (rainfall and variations of the piezometric level) were studied separately until Hendron and Patton: they correlated the daily precipitation with the piezometric records, under the hypothesis of the existence of an artesian aquifer located at the base of the landslide mass ("the lower permeability of the clay layers and the higher permeability of the intervening limestones and cherts must have combined to significantly increase the hydraulic conductivity along the bedding relative to that across the bedding. This effect results in a classic case of an inclined multiple-layer artesian aquifer system at and below the surface of sliding" (Hendron and Patton, 1985)).

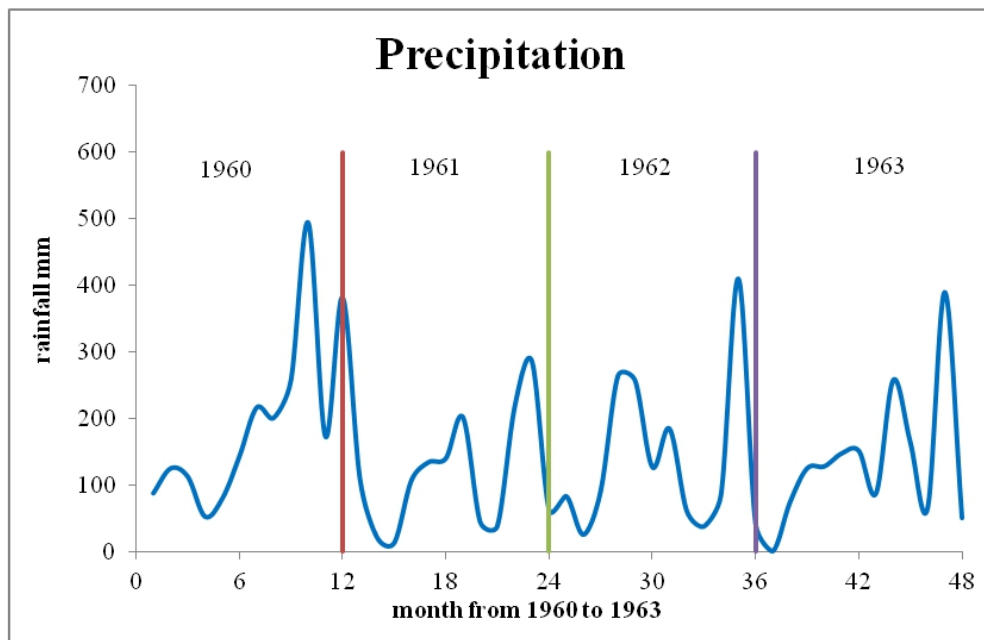


FIGURE 3.2: Monthly precipitation (in mm) from 1960 to 1963 (Hendron and Patton, 1985)

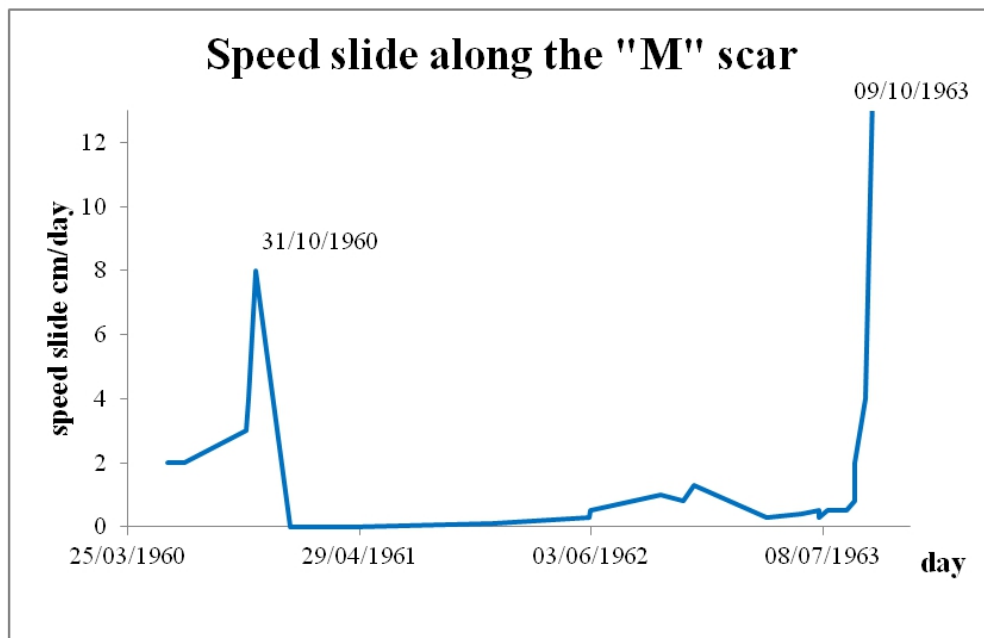


FIGURE 3.3: Rate of movement from 1960 to 1963 (Hendron and Patton, 1985)

The artesian aquifer has particular features that play a key role in the soil stability. The aquifer, confined by impermeable clay layer at the base of the slice, is under pressure exceeding that of atmospheric pressure due to the amount of rain. Every time the level

of the water basin quickly decreases, the hydrostatic conditions of the soil are missing causing a rise of the pore pressure and a decrease of the shear stress along the sliding surface (Crawford et al., 2008, Faukker and Rutter, 2000, Reep, 2009): the stability condition reaches a critical point that leads to the slipping of the mass.

In fact the first movement of the mass corresponds with the end of a very rainy year (1960), fig. 3.3 and we can correlate the increase in the piezometric level with the decrease of the safety factor (Kaneko et al., 2009).

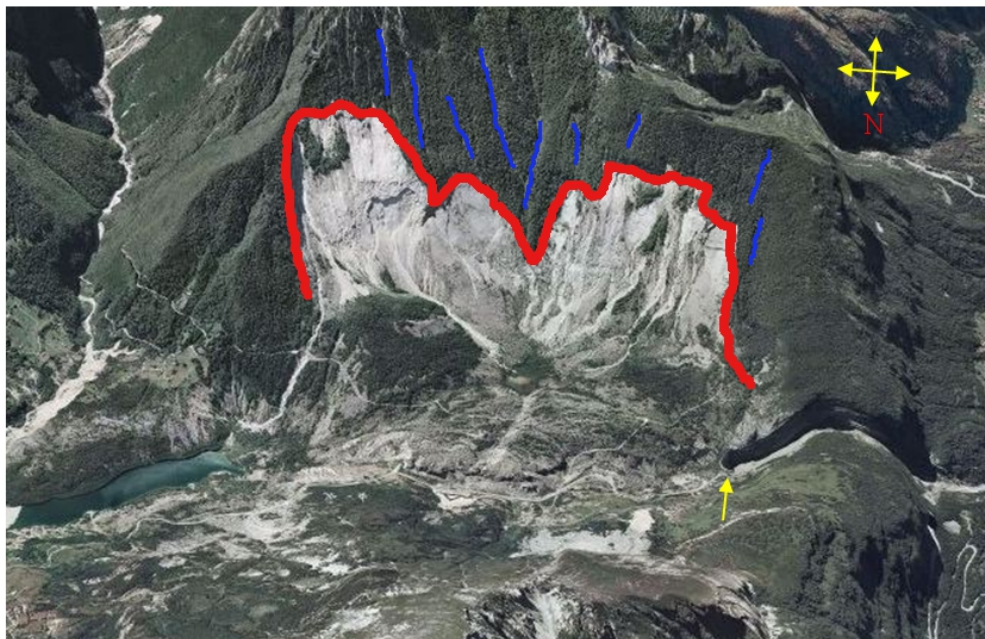


FIGURE 3.4: Map of the Vajont slide: the red line is the failure scar and the blue lines represent some discontinuity set along the crown. The main scarp can be divided in two parts: the upper one is composed mainly of micritic and cherty limestone with thin intercalation of green clay and marl, while the part near the deposit is constituted of alluvial and glacial deposits. The yellow arrow indicates the position of the dam.

3.2 Analysis of stability

Although the whole mass of the slide, approximately of 260 million m^3 , ran down at the same time, it is now well established that the failure mechanisms have not been the same along the entire sliding surface, so that we can talk of more slip sub-surfaces: in view of results coming from seismic tomography, numerical simulations of the slide

motion and comparison of pre- and post-landslide maps, the slip surface can be divided in two main areas (Francesse et al., 2013).

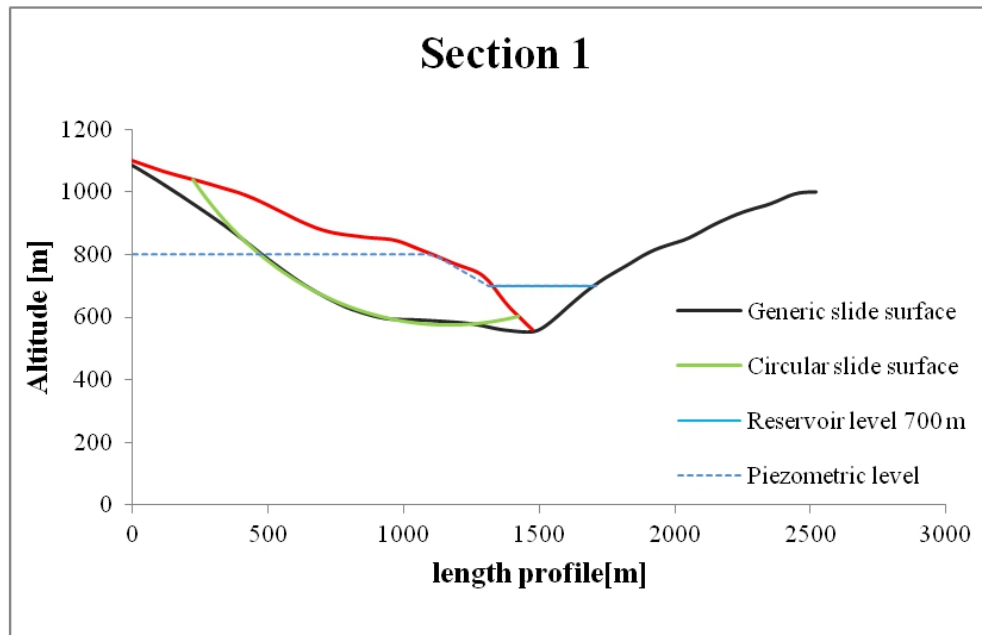


FIGURE 3.5: Longitudinal profile 1 of Vajont (Paparo et al., 2013)

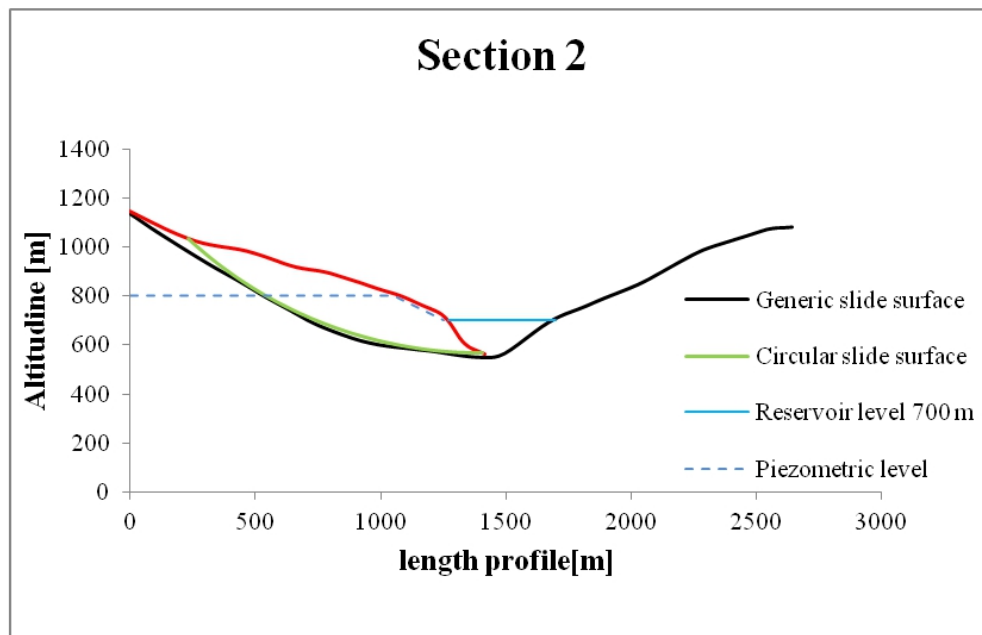


FIGURE 3.6: Longitudinal profile 2 of Vajont (Paparo et al., 2013)

For this reason we divide the landslide body into two parts (that can be named as the east and west part) and for each part we select one main profile, profile 1 fig. 3.5 and

Specific weight of the Vajont limestone	26 KN/m^3
Friction angle of fissured limestone	22°
Friction angle along the clay-limestone interface	8°
Coefficient of cohesion for a fractured rock matrix	20 KPa
Coefficient of cohesion along the clay-limestone interface	10 KPa

TABLE 3.1: Geotechnical parameters of section 1 (Hendron and Patton, 1985)

Specific weight of the Vajont limestone	26 KN/m^3
Friction angle of fissured limestone	22°
Friction angle along the clay-limestone interface	17°
Coefficient of cohesion for a fractured rock matrix	20 KPa
Coefficient of cohesion along the clay-limestone interface	10 KPa

TABLE 3.2: Geotechnical parameters of section 2 (Hendron and Patton, 1985)

profile 2 fig. 3.6. The analysis begins in steady condition and the parameters of the west (tab. 3.1) and the east zones (tab. 3.2) are changed until reaching the condition of the limit equilibrium. These soils, when saturated by water, lose significantly their shear strength and unconfined compressive strength, become fragile and their grains break down in water as observed in grain size analysis (Kim et al., 2004, Lee and De Freitas, 1989).

3.2.1 Application of classical and MLD methods

First we analyze the two profiles by means of all methods introduced earlier: in this case we assume a homogeneous unsaturated body composed of only fractured dolomitic limestone.

The figs. 3.7, 3.8 and 3.9 show the functions $E(x)$, $X(x)$, and $A(x)$ for each method: in line with the theory discussed in the second chapter, we observe that the Morgenstern and Price and MLD methods satisfy all three boundary conditions for the two components of the inter-slice forces and the moment.

In fig. 3.10 we can see that the F value varies in function of the used method: Janbu gives the lowest values of F , but it does not satisfy all the boundary conditions, and this is also true for the Bishop method. Only the methods of Morgenstern and Price and MLD satisfy all the conditions of problem.

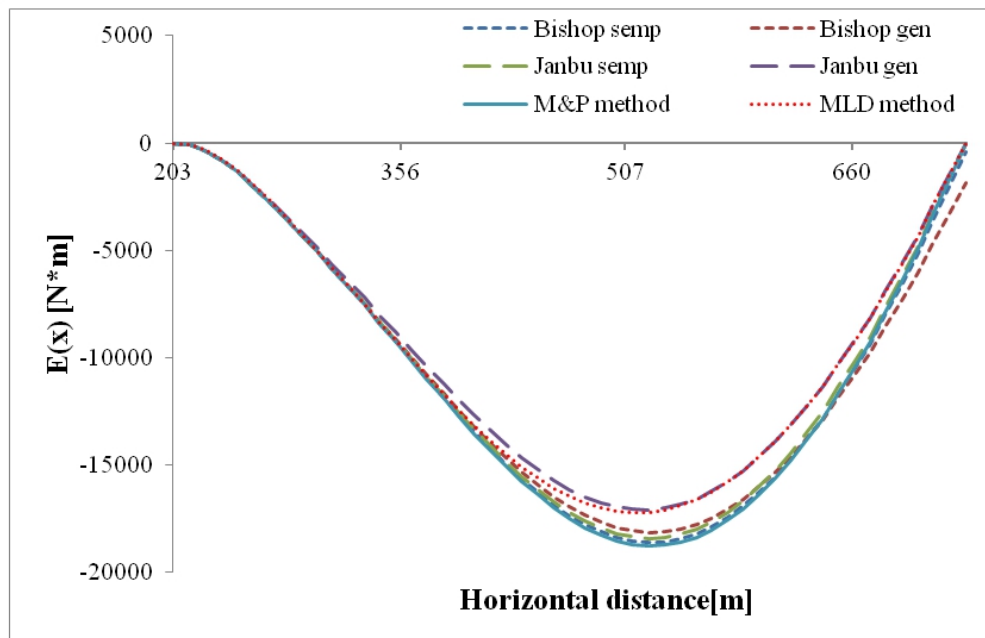


FIGURE 3.7: Comparison of inter-slice forces $E(x)$ obtained by means of all different methods: all methods satisfy the boundary conditions, but the generalized Bishop method (see the second chapter) (Paparo et al., 2013).

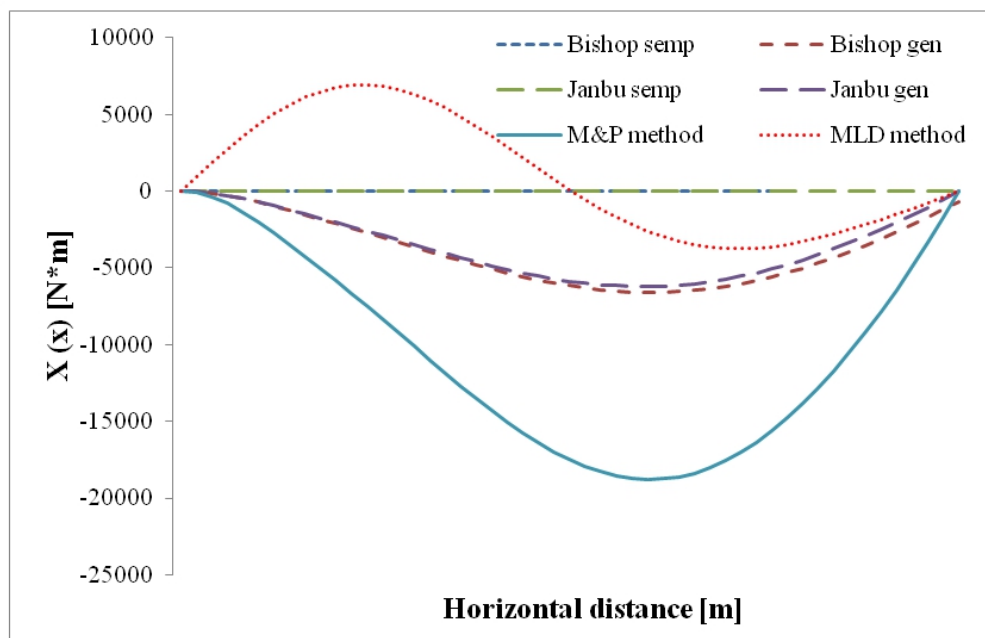


FIGURE 3.8: Comparison of inter-slice forces $X(x)$ obtained by means of different methods: all methods satisfy the boundary conditions with the exception of the generalized Bishop method (Paparo et al., 2013).

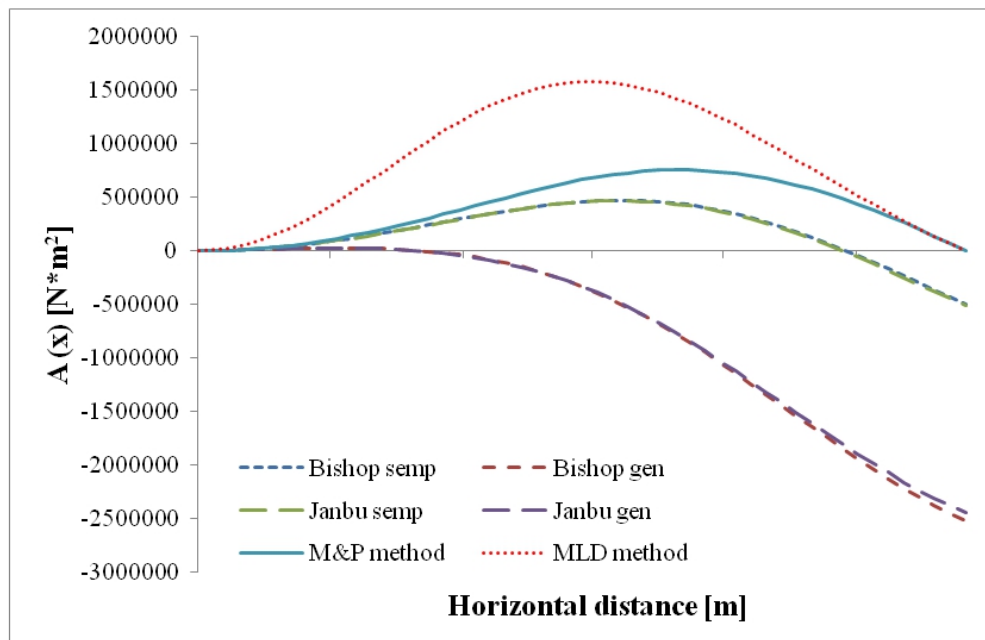


FIGURE 3.9: Comparison of the moment $A(X)$ obtained by means of different methods: in this case the Bishop and Janbu methods do not satisfy the boundary conditions, while the *MLD* and *M&P* methods do (Paparo et al., 2013).

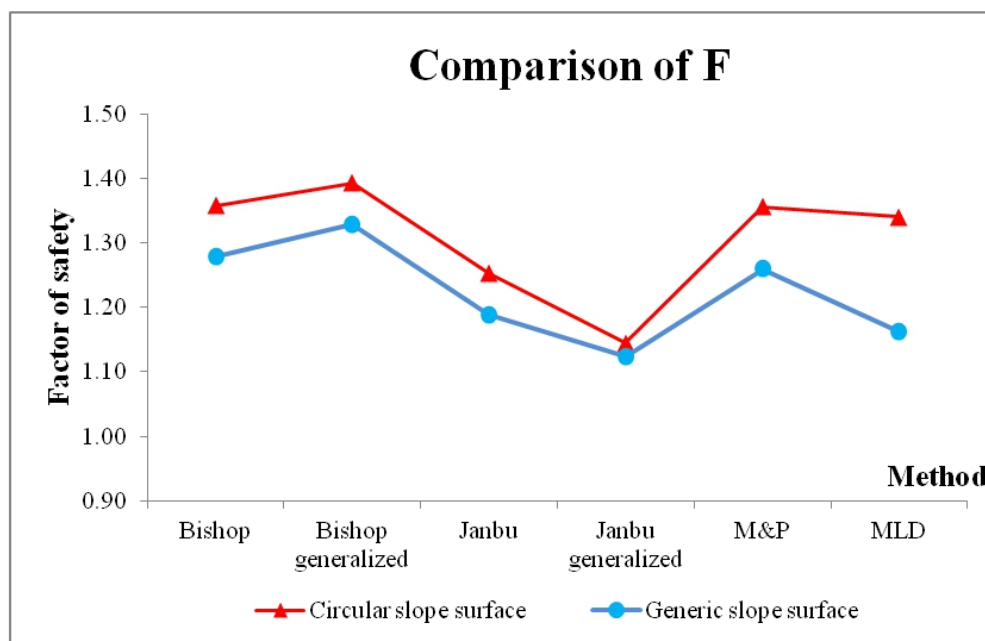


FIGURE 3.10: Values of F resulting from the different methods.

3.2.2 Analysis of stability with the MLD method

To deepen the analysis of the Vajont case we selected to use only the MLD method to reconstruct the conditions that led to the instability of the Mount Toc slope.

We can divide our analysis in six cases:

- Case 1: the soil is unsaturated and the basin level increases up to 710 m;
- Case 2: the level of the reservoir and the piezometric level increase both up to 710 m;
- Case 3: the reservoir and piezometric levels increase up to 710 m and the clay layer along the slip surface decreases its cohesion due to the rise of the pore pressure;
- Case 4: the level of the basin and of the piezometric line are as in the third case, but the friction angle decreases;
- Case 5: the level of the basin and of the piezometric line are as in the third case, and both the friction angle and cohesion change because of the rise of pressure in the soil;
- Case 6: the level of the reservoir is stable at 710 m and the piezometric level increases up to 790 m, the cohesion and the angle of friction change like in the fifth case.

Figs. 3.11 and 3.12 show that when the level of the reservoir increases also the value of F rises, since the load of the basin stabilizes the slope (Case 1). Following the geological analysis of post-landslide a series of layers of clay was identified, placed along the sliding surface of the landslide; the soil, above the critical surface, from unsaturated becomes saturated due to impermeability of clay and due to the rise of the piezometric level (Case 2). The piezometric level increased due to the increase of the level of the basin and due to the heavy rainfall: furthermore, the geotechnical parameters at the base of the failure surface also change, in particular the value of the cohesion and of the friction angle (Hendron and Patton, 1985, Müller, 1964) (Cases 3, 4 and 5).

In all of the cases the value of F does not reach the critical value of 1, but we can see, according to our analysis, that the predominant element for changing the safety factor is the angle of friction.

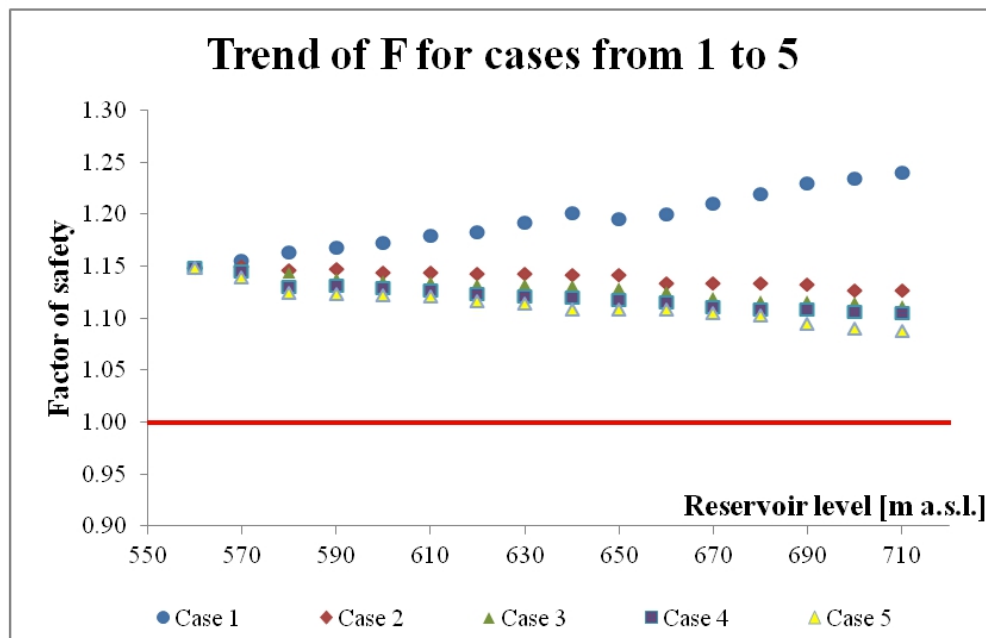


FIGURE 3.11: Trend of F for different cases for profile 1: in case 1 reservoir level increases; in case 2 reservoir and piezometric levels increase; in case 3 reservoir and piezometric levels increase and the cohesion varies from 20KPa to 10 KPa; in case 4 reservoir and piezometric levels increase and the angle of friction varies from 22° to 17° ; in case 5 reservoir and piezometric levels increase and the cohesion and the angle of friction vary. The red line highlights the critical condition of F equal to 1

Figs. 3.13 and 3.14 show the case 6 for both profiles: increasing the piezometric level means increasing the pore pressure. As viewed in the relation of Mohr-Coulomb, the pore pressure decreases the effective normal stress, which itself leads to a decrease of the shear stress. The final result is the reduction of the safety factor, but also in this case we do not reach the unstable conditions, even though we are very close.

The decisive role that breaks the weak equilibrium of the slope, is played by the lowering of the level of the basin that took place relatively rapidly compared to the time required for the soil to reach the hydrostatic conditions.

The red points in figs. 3.13 and 3.14 indicate the condition of instability, F less than 1, obtained after the lowering of the basin from 710 m down to 700 m and the increase of the piezometric level due also to the precipitation in the months preceding the landslide. The concomitant occurrence of these conditions, natural and due to human intervention, have varied the geological and structural conditions of the soil, leading to the failure of

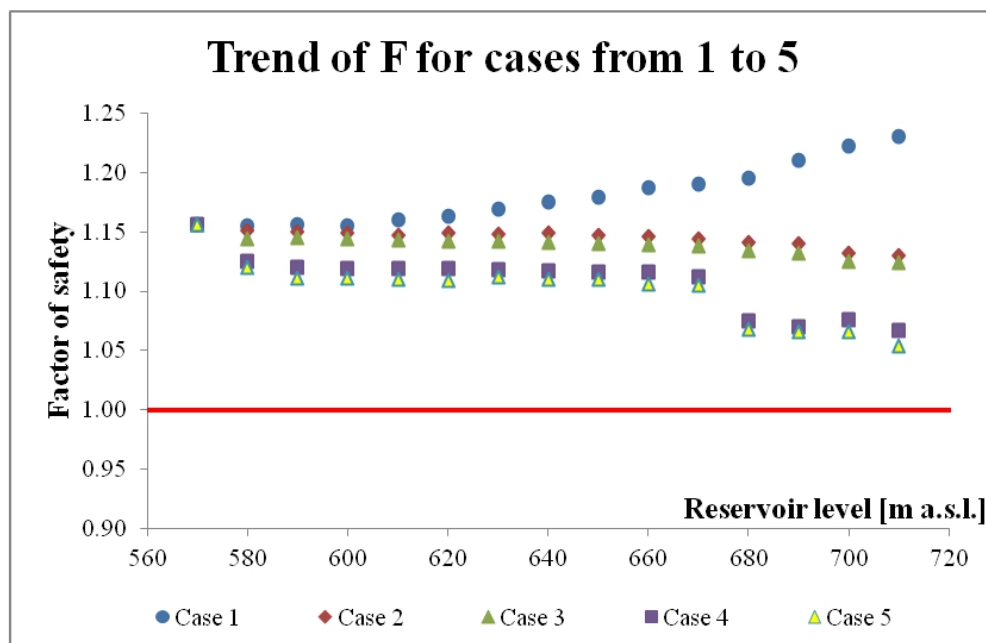


FIGURE 3.12: Trend of F for different cases from 1 to 5 for the profile 2: see fig. 3.12

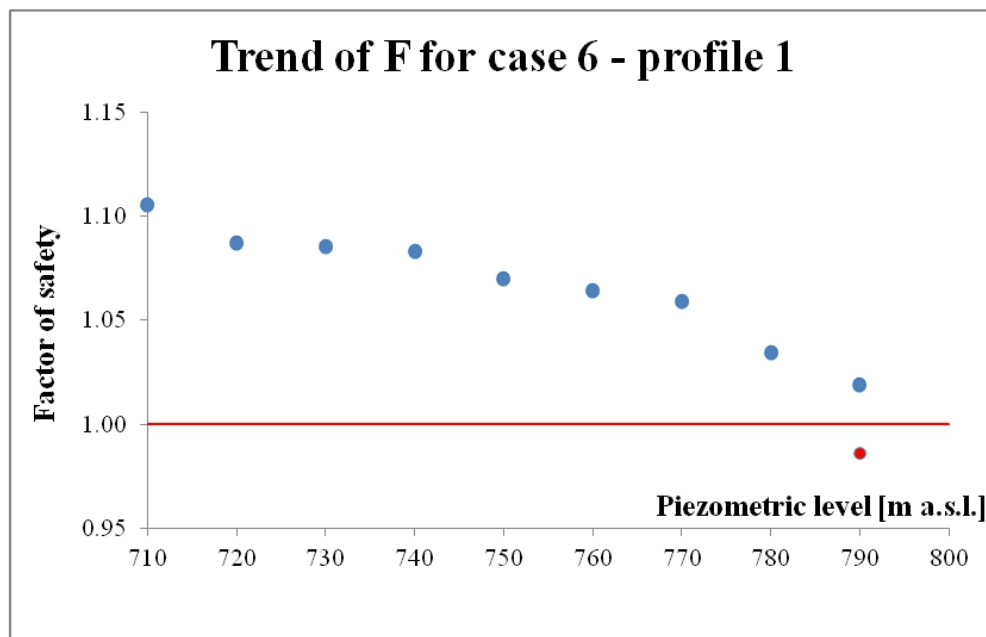


FIGURE 3.13: Trend of F for case 6, profile 1: we keep the reservoir level constant at 710 m and we raise the piezometric level to 790 m (Hendron and Patton, 1985), reaching the limit equilibrium. Lowering the level basin from 710 m to 700 m triggers the instability (red dot)

the Mount Toc flank, and on October 9th, 1963, 10:39 p.m., the giant landslide slipped in the Vajont lake.

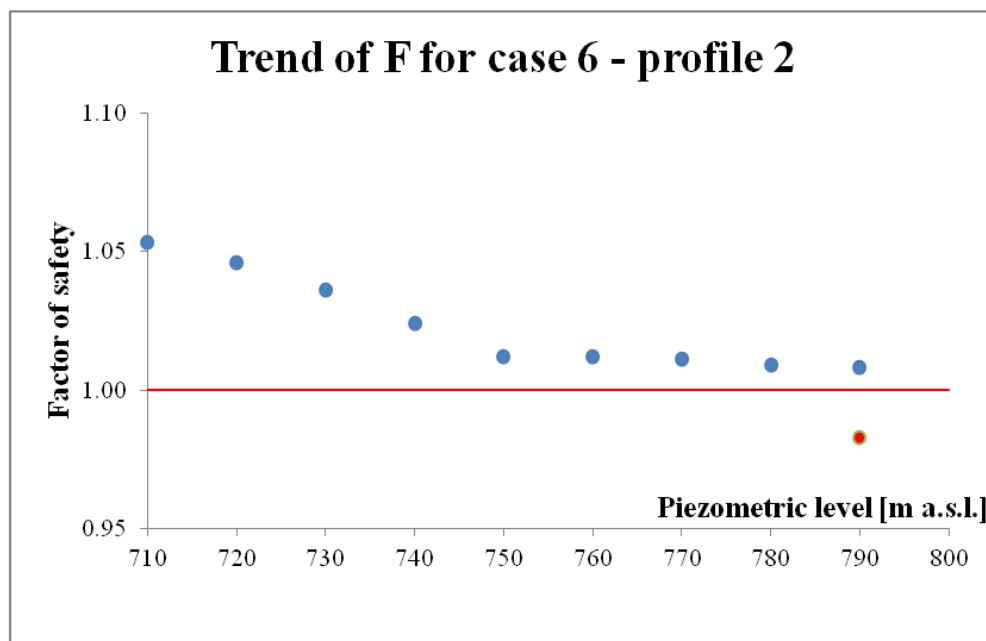


FIGURE 3.14: Trend of F for case 6, profile 2: as in profile 1, we keep the reservoir level constant at 710 m and we raise the piezometric level to 790 m (Hendron and Patton, 1985), reaching the limit equilibrium. Lowering the level basin from 710 m to 700 m triggers the instability (red dot).

3.3 Conclusions

The case of the Vajont is perfectly suitable to compare different analyses of slope stability with the limit equilibrium methods, showing the principal differences in line with the theory developed in the second chapter.

The main purpose of this chapter was to show our work in reconstructing the main processes that led to the instability of the flank of the Mount Toc: the safety factor varied greatly, depending on the conditions of the soil, saturated or unsaturated, and on the values of the geotechnical parameters of the soil along the slip surface (the angle of friction and cohesion). Finally, the slope collapsed due to the rise of pore pressure inside the ground due to the heavy rain precipitations and the quick lowering of the basin level from 710 m to 700 m.

All of these factors generated the landslide that detached and provoked the disaster of 9 October 1963.

Chapter 4

Analysis of two Norwegian sites

The purpose of the chapter 3 was to build the conditions that led to the Vajont landslide, using the *MLD* method and the large amount of data obtained from the continuous monitoring during the construction of the dam: the results obtained are able to explain the main factors causing the disaster.

In this chapter the main goal is to derive the equilibrium conditions of two sites along the Norwegian continental margin prone to landslides and to find what conditions would bring the two slopes to instability.

The cases treated in this chapter were provided by the Norwegian Geotechnical Institute (NGI) of Oslo, during my visit there. We can divide the work in two main parts based on the degree of steepness of the slopes. The first part takes into account a low-angle slope, specifically one of the landslides which affected the continental margin off the Lofoten and Vesterålen. The second part considers a slope with a high angle, namely the headwall scar of the Storegga slide.

Furthermore, another objective of this study is to compare the results obtained by means of the *MLD* technique with the results of the Morgenstern and Price (*M&P*) method, because the latter is one of the limit equilibrium methods that satisfies all of the problem conditions. In order to analyze the slope with the *M&P* method, the software GeoStudio2012 has been used that is one of the most important tools in the engineering field.

In particular the package Slope/W has been utilised, which is the specific section of the program GeoStudio2012 dedicated to the study of slope stability.

4.1 The Lofoten and Vesterålen analysis

Several geological and geophysical studies (Brekke, 2000, Doré et al., 1999, Mosar, 2003, Olesen et al., 1997, Talwani and Eldholm, 1977) show that the Norwegian continental margin can be divided into a series of segments: one of these is the selected area of Lofoten and Vesterålen, that belongs to the northernmost segment of the Norwegian continental margin (fig. 4.1,4.2).



FIGURE 4.1: Map of the Scandinavian Peninsula

We can identify several canyons along the shelf, eroded by ice streams during the glacial period. The flanks of these canyons have a slope of about 30° , while the sea floor dips gently with a gradient of 3° . Since also the sea floor is affected by landslides, our analysis focuses along a profile whose inclination varies from 2° to about $4^\circ - 5^\circ$ (fig. 4.3).

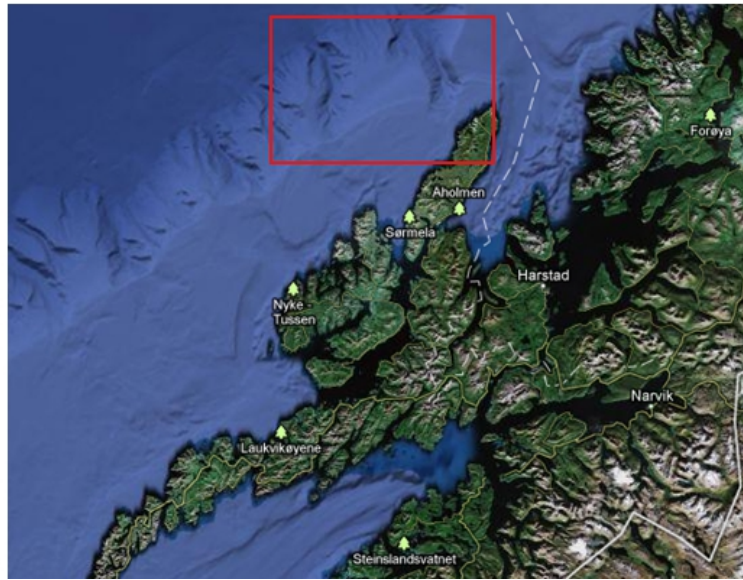


FIGURE 4.2: Lofoten and Vesterålen area: the red square indicates the analyzed zone

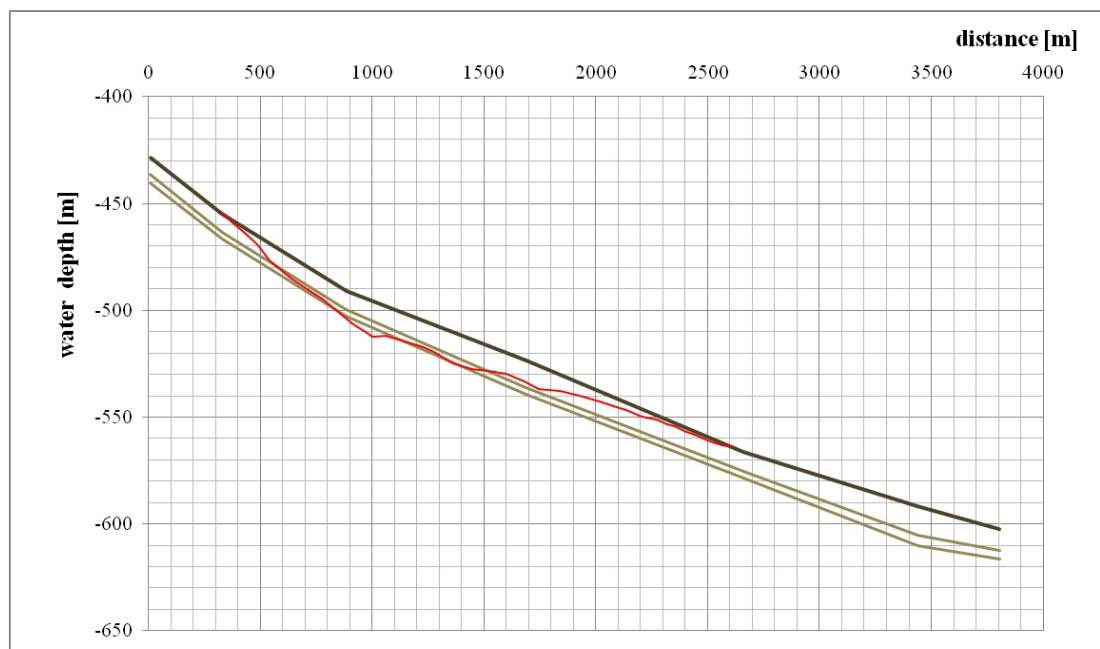


FIGURE 4.3: Profile used to compare the results obtained by means of the (*M&P*) and the MLD methods. The red line indicates the post-landslide surface, while the dark brown line indicates the reconstructed top surface of the slope. The light brown line indicates a thin layer of overconsolidated clay

Cohesion c	5 KPa
Unit weight γ of laminated clay	18.3 KN/m^3
Unit weight γ of sandy glacial clay	17.7 KN/m^3
Friction angle ϕ	$28^\circ - 30^\circ$

TABLE 4.1: Geotechnical parameters of the sediments

Geotechnical investigations show that the soil is composed of a series of layers of sandy clay and silty clay. The drained strength parameters of sediments have been determined from Triaxial and DSS tests (L'Heureux et al., 2013).

To get the conditions in which the slope currently is, we start from the simplest case of a homogeneous slope and we observe how the value of F changes, step by step, on varying the external loads.

To ensure the comparison of the results of the two methods, we divide this section into four parts, each one illustrates the following analysis:

- Homogeneous slope and circular surface without piezometric and basin levels
- Homogeneous slope and circular surface with piezometric and basin levels
- Homogeneous slope and circular surface changing the parameter r_u
- Homogeneous slope and circular surface with seismic load

4.1.1 Homogeneous slope and circular surface without piezometric and basin levels

We start with a simple case of a homogeneous slope in drained conditions. The trial surface has been selected on the basis of typical shapes of the scars left by landslides that have occurred. The slope has been divided into 50 slices.

The results show that the shapes of the inter-slice functions are different (figg. 4.5 4.6), in particular this is true for the function $X(x)$, just as observed in the Vajont case: its expression in the $M\&P$ method is a half-sine equation by assumption (2.43) while in the MLD method is a Fourier sine expansion truncated to the third term (2.44).

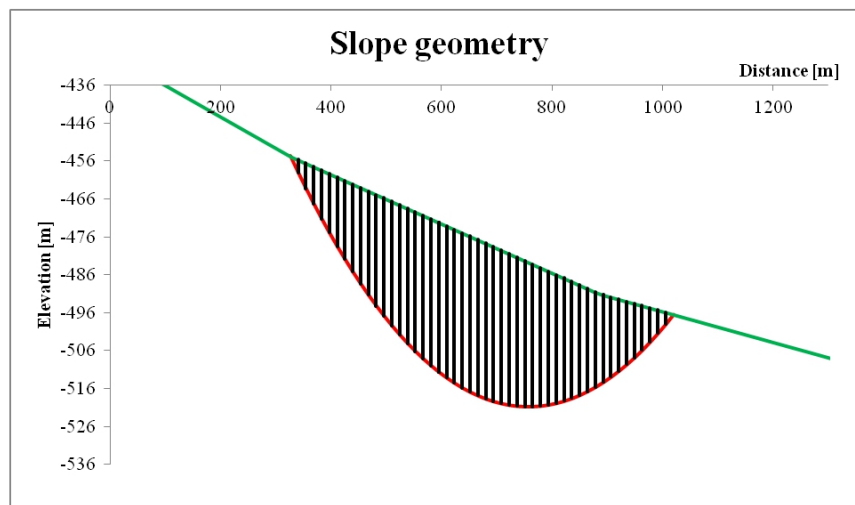


FIGURE 4.4: Cross-section and partition of the slide into 50 slices. The green line is the top of the slide and the red line is the trial circular slip surface

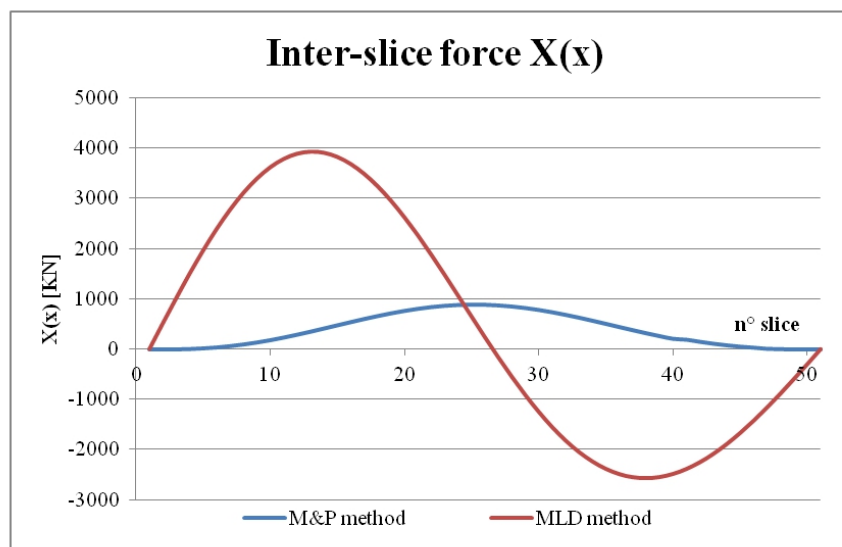


FIGURE 4.5: Comparison of the functions $X(x)$ obtained by means of the Morgenstern and Price and *MLD* methods

Small differences can be identified also in the shape of the normal and shear stresses (figs. 4.7, 4.8), the results for bottom pressures $P(x)$ and shear stresses $S(x)$ are very similar and the safety factor obtained with the two codes are also quite close to each other: $F_{M\&P} = 8.831$ and $F_{MLD} = 8.864$.

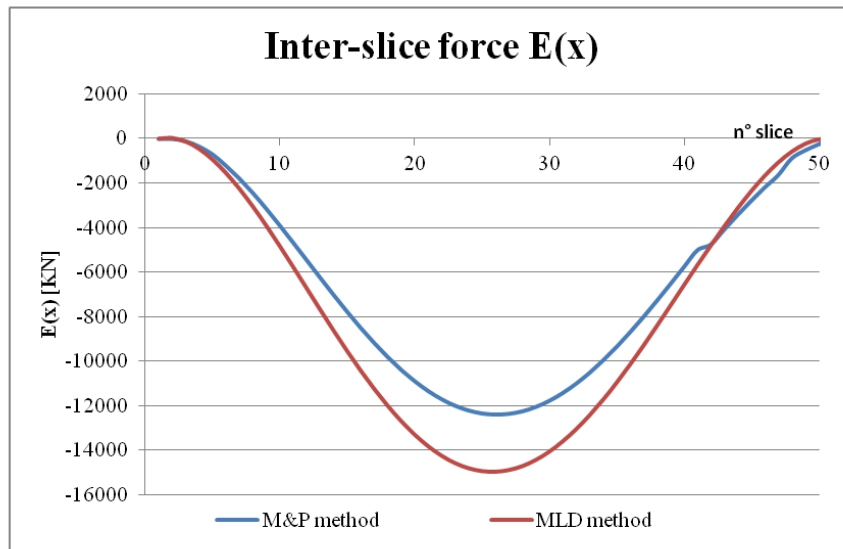


FIGURE 4.6: Comparison of the functions $E(x)$ obtained by means of the Morgenstern and Price and *MLD* methods

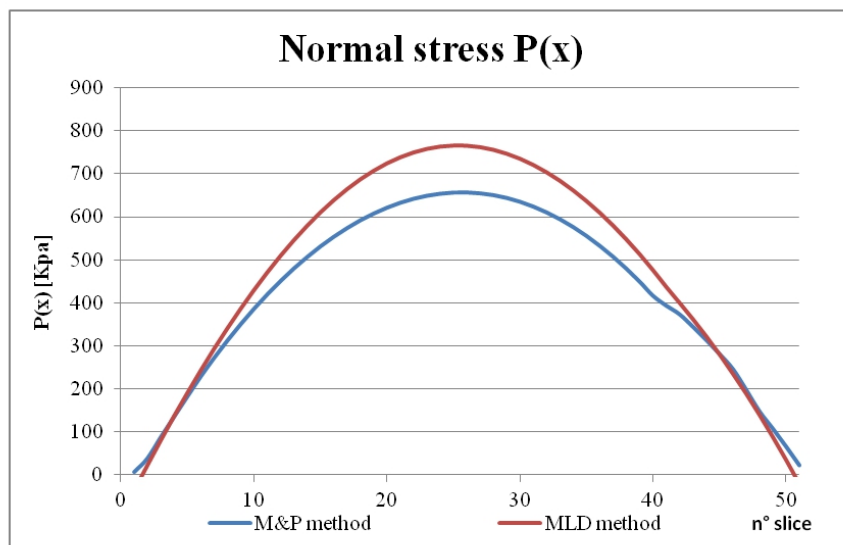


FIGURE 4.7: Comparison of the functions $P(x)$ obtained by means of the Morgenstern and Price and *MLD* methods

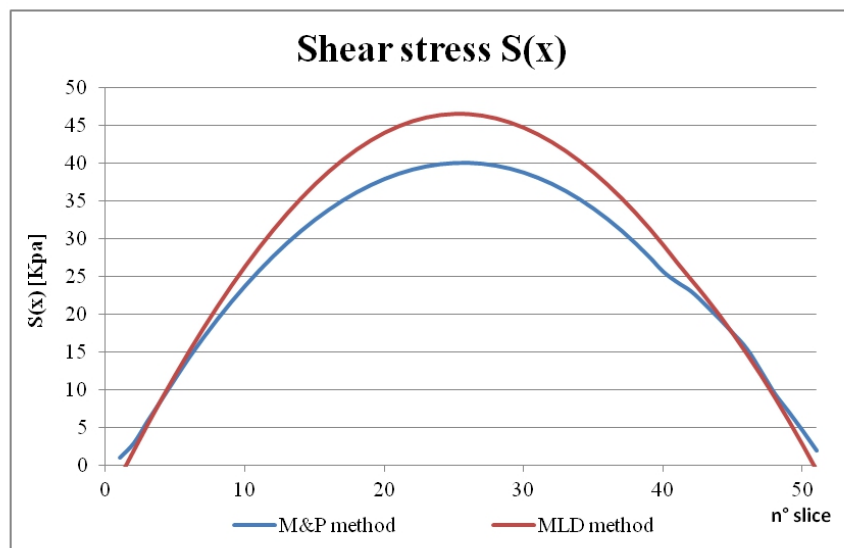


FIGURE 4.8: Comparison of the functions $S(x)$ obtained by means of the the Morgenstern and Price and *MLD* methods

4.1.2 Homogeneous slope and circular surface with piezometric and basin levels

In this second case we observe the behavior of F as a function of the piezometric and basin levels. We observe an initial lowering of the factor of safety and then a gradual rise of F on increasing the piezometric level, until reaching the value of about 9, when the entire profile is completely covered by water, fig. 4.9.

The final results when the basin level is 0 m a.s.l. are $F_{M\&P} = 9.069$ and $F_{MLD} = 8.979$ (fig. 4.9). Also in this case, the results are very close though not perfectly equal, with about 1% discrepancy. This is due to the fact that the two methods make use of different approaches to the solution of the problem: in the *MLD* method the contributions of the pore pressure $u(x)$ and the hydrostatic load $D(x)$ are considered separately: the first is taken into account inside the Mohr-Coulomb criterion 2.11, and the second inside the three equations of the limit equilibrium, 2.7, 2.6 and 2.8. In this way the pressure along the sliding surface is also a function of the height of the overlying water column. Instead the program Slope/W implementing the *M&P* method, considers the submerged weight of the slice, and the normal pressure turns out to be independent from the height of the water above the slope:

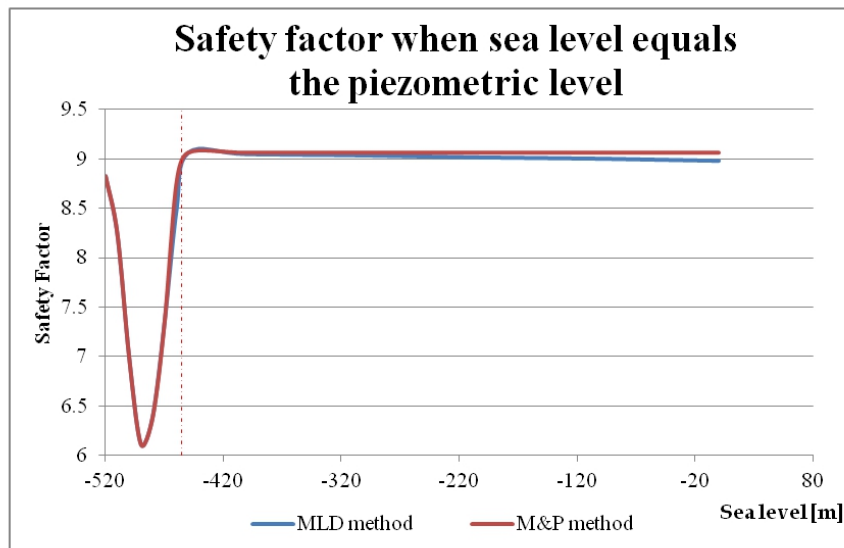


FIGURE 4.9: Trend of the safety factor as a function of the basin level: in this case the level of the sea and the piezometric level are coincident

$$P' = h_{slice}(\gamma_s - \gamma_w) \quad (4.1)$$

where h_{slice} is the height of the slice, γ_s is the unit weight of the soil and γ_w is the unit weight of the water.

Finally, we can say that if the level of the basin increases in the same manner as the piezometric level, the variations of the safety factor are consistent until the slope is completely submerged. Afterwards the soil reaches the hydrostatic condition. Indeed, if inside the *MLD* method we take into account only the effect of the buoyancy force, one obtains $F_{buoyancy} = 9.069$, perfectly identical to that obtained through Slope/W.

4.1.3 Homogeneous slope and circular surface changing the parameter r_u

The situation changes if we take into account the excess of pore pressure: it is expressed through the coefficient r_u , that is defined as the ratio of the pore-water pressure to the weight of the slice

$$r_u = \frac{u(x)}{w(x)} = \frac{(z_{piez} - z_1)\gamma_w}{(z_2 - z_1)\gamma_s} \quad (4.2)$$

If the value is 0, the soil is in hydrostatic conditions.

This parameter is not constant along the slope, but in Slope/W it is taken as constant since it is defined as

$$r_u = \frac{A_1 r_{u1} + A_2 r_{u2} + A_3 r_{u3} + \dots + A_n r_{un}}{A_1 + A_2 + A_3 + \dots + A_n} \quad (4.3)$$

where A_i is the area of the single slice and n the number of the vertical slices. Mathematically, r_u is an average value, and therefore the same value of r_u can be achieved by different combinations (Fredlund, 1974, Fredlund and Krahn, 1977). In the manual of Slope/W it is specified that the variable r_u within a slope makes it an impractical option in a software package like Slope/W. The r_u option is included in Slope/W mainly for historical reasons. However making use of this option is not recommended, except in some simple cases.

In the *MLD* method r_u is not defined, but we are allowed to assign the piezometric level point by point, which is equivalent to use a value of r_u depending on the horizontal distance. In fact it is possible to establish the following relationship between the piezometric level, z_{piez} and r_u :

$$z_{piez}(x) = z_1(x) + r_u(x) \frac{[z_2(x) - z_1(x)]\gamma_s}{\gamma_w} \quad (4.4)$$

Although r_u is not recommended, it is often used in the engineering field.

Fig. 4.10 shows as the factor of safety decreases with the rise of the excess pore pressure: the water inside the pores is not free to move and remains confined, in this case, below the sliding surface, generating a pressure that destabilizes the mass. In fact, we can see that the safety factor decreases significantly, though it does not reach the critical condition.

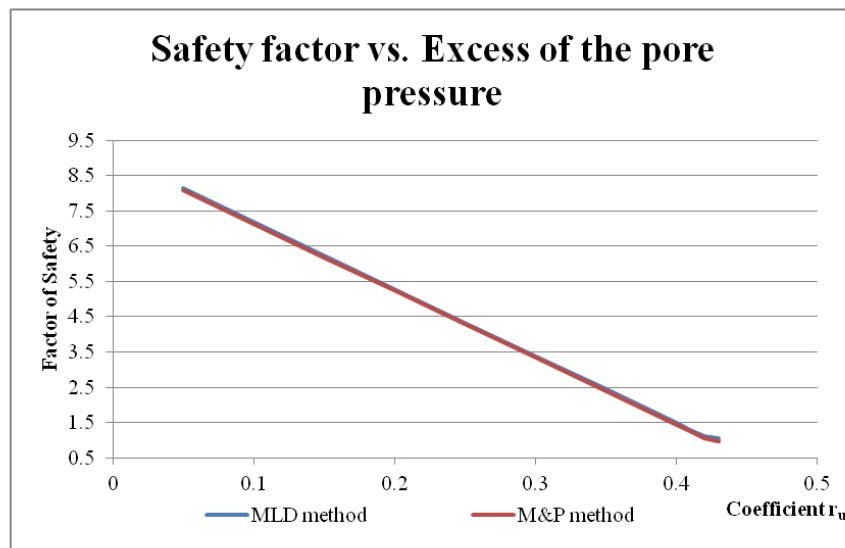


FIGURE 4.10: Trend of the safety factor as a function of the parameter r_u for a submerged slope

4.1.4 Homogeneous slope and circular surface with seismic load

In addition to the water and its pressure, there is another important external factor that can greatly influence the stability of a slope: the seismic load.

Though the examined area, as the whole Scandinavian zone, does not have frequent seismic records, it does not mean that the area is aseismic (fig. 4.13).

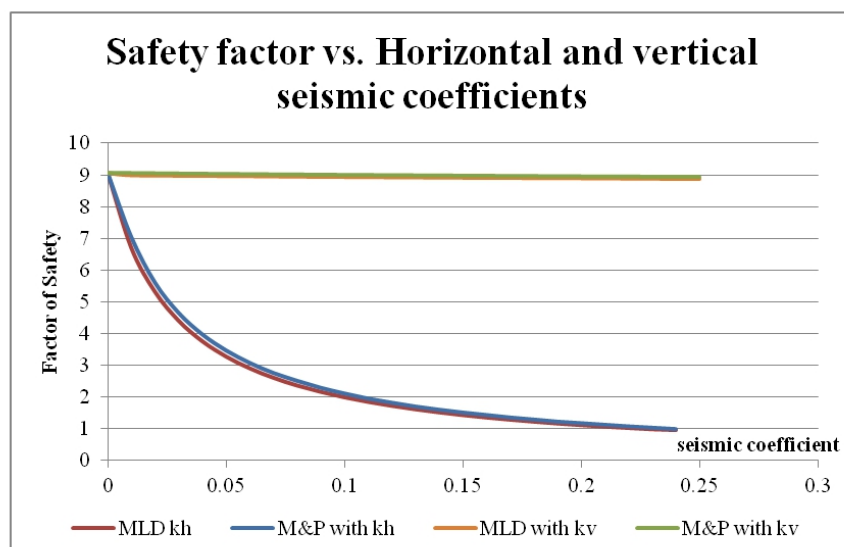


FIGURE 4.11: Trend of the safety factor as a function of the seismic coefficients k_h and k_v for a submerged slope.

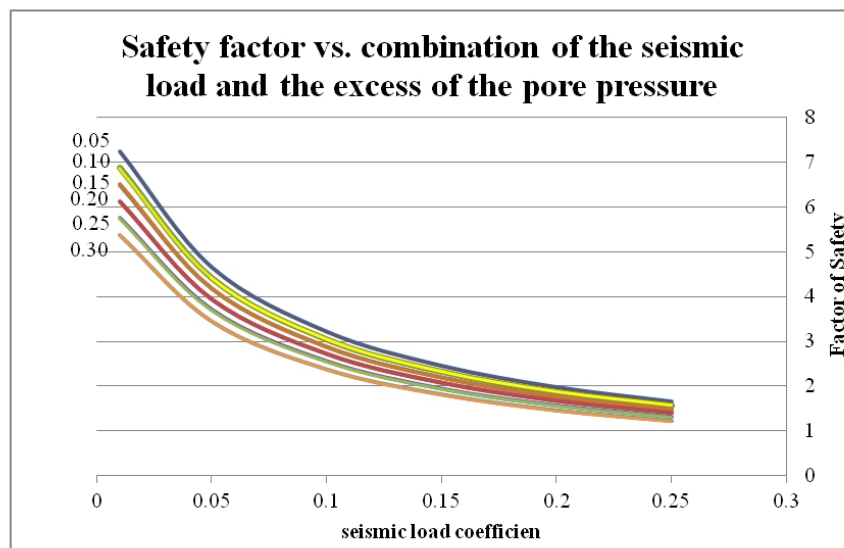


FIGURE 4.12: Trend of the safety factor as a function of the seismic coefficients and the excess of pore pressure

Although there are no seismic records, from geological studies and seismic analyses one can determine what types of earthquakes can occur in the area, their peak ground acceleration and their recurrence period.

Once this information is obtained, we can use the data of the real earthquakes that are close to those hypothesized. In the case of the Norway, three time series are suggested, recommended by NORSAR and NGI, Bungum (1998):

- Nahanni, Canada, 23-12-1985, occurred in the Nahanni region of the Mackenzie Mountains in the Northwest Territories. It is a mainshock with $M_w = 6.8$, fig. 4.14
- Imperial Valley, USA, 15-10-1979 occurred at the Mexico-United States border, with $M_w = 6.4$, fig. 4.15 (Johnson and Hutton, 1982)
- Tarcento, 11-09-1976, occurred in the Friuli region of Italy. It is an aftershock belonging to the famous Friuli seismic sequence recorded at Tarcento $M_w = 5.5$, fig. 4.16

Usually, in the engineering works one takes into account only the horizontal contribution of the soil acceleration of an earthquake, because the vertical contribution is

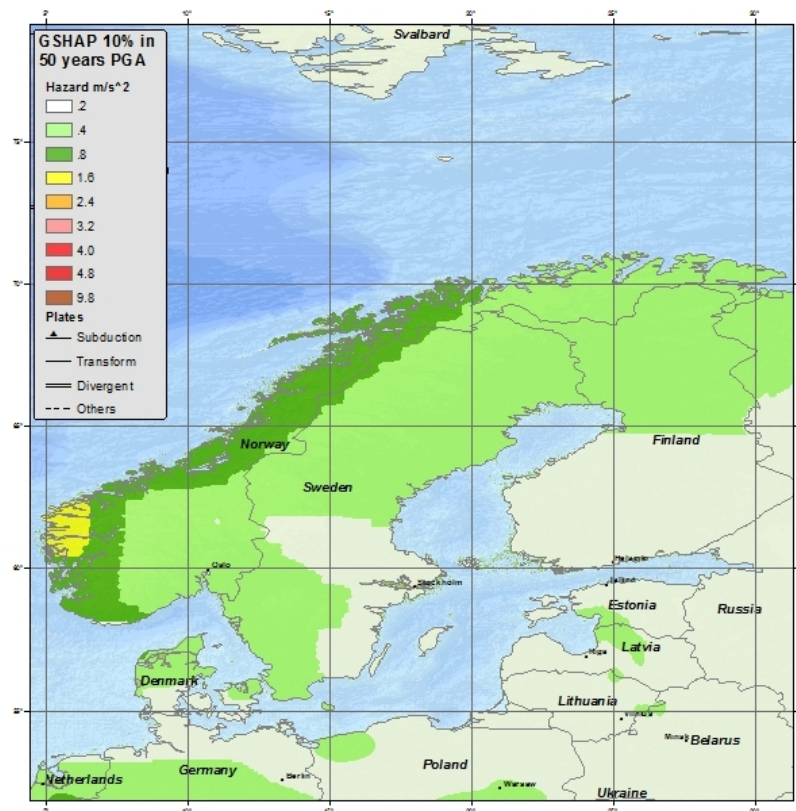


FIGURE 4.13: Seismic Hazard Map of the Norway (USGS site: <http://earthquake.usgs.gov/earthquakes/world/norway/gshap.php>)

believed to be smaller, as we can see in fig. 4.11. On changing the seismic coefficient from 0.01 to 0.22 (the maximum value of the PGA selected), in the vertical and horizontal directions, we can observe that the variation of F for k_v is about 1%, while for $k_h = 0.22$ one obtains the critical condition, $F = 1$. But if we take into account the joint effect of the horizontal seismic load and of the coefficient of pore pressure for a generic slope, we see the same trend of fig. 4.11, but with some slight difference. It seems that the water slightly increases the cohesion of the soil. This argument is very delicate, since many studies have shown that the effect of the excess pore is not immediate, but may appear after a certain period of time (even months) after the earthquake. This principle is the base of the liquefaction phenomenon, but this topic will not be addressed in this context.

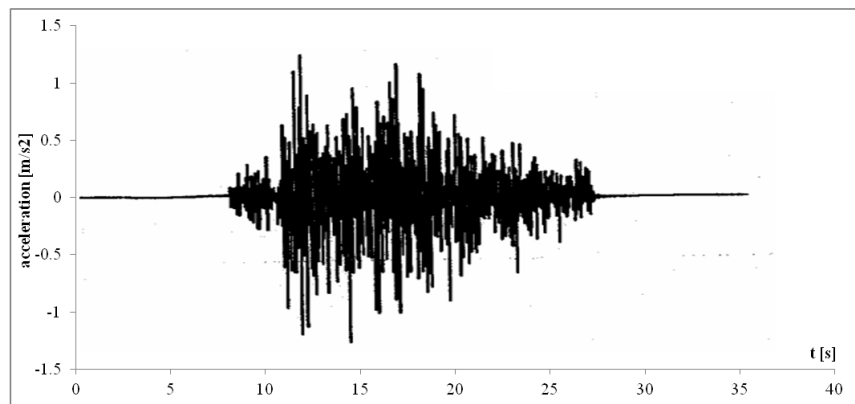


FIGURE 4.14: Acceleration time series of Nihanni: $k_h = 0.155$

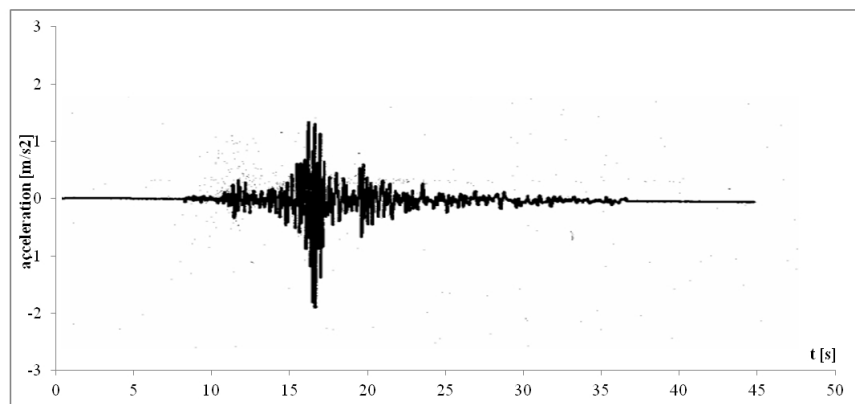


FIGURE 4.15: Acceleration time series of Imperial Valley: $k_h = 0.204$

4.1.5 Summary of Lofoten and Vesterålen analysis

We had two main objectives: the first was to compare our method with the *M&P* method implemented in the GeoSlope software, and the second was to assess what conditions could cause a destabilization of the slope. The analysis, performed on a typical Norwegian submerged slope with an inclination of about $2^\circ - 3^\circ$, shows that the discrepancy between the two methods (*MLD* and *M&P*) is very small for all the simple cases addressed here, with *F* values found in the range of 9.

To evaluate the conditions for the instability we took into account the pore pressure in hydrostatic conditions and an excess pore pressure due to a confined aquifer. Finally, we considered the seismic loads and used values of real earthquakes that, in line with

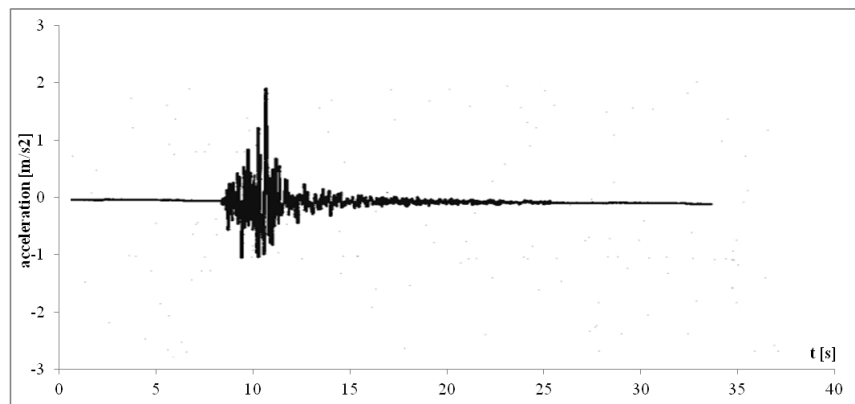


FIGURE 4.16: Acceleration time series of Friuli: $k_h = 0.220$

the studies of NORSAR and NGI, have a certain recurrence in Norway. It was found that in this case F can reach the value of 1.

In conclusion, for this flat slope we cannot highlight an evident difference between the *MLD* and the *M&P* method, and the slope can fail under a seismic load with $PGA = 0.22g$.

4.2 The Storegga Headwall analysis

We repeated the same analysis for a profile with a greater angle of inclination. The profile analyzed is a steep slope at the headwall of Storegga at the edge of the continental shelf of Norway (fig. 4.17 and 4.18). This area is part of the scar left by the Storegga landslide, one of the largest known landslides occurred underwater, causing a large tsunami in the Holocene.

The seismic analysis shows that the headwall is composed of a series of layers of glacial till and marine clay, linked to the main glaciations.

First we take into account the simple case of a homogeneous submerged slope, 4.19, without excess pore pressure and seismic load, as done in the previous analysis.

The geotechnical parameters values are equal to the Vesterålen slope, because the soil is composed of overconsolidated clay layers.



FIGURE 4.17: Map of the Scandinavian Peninsula.



FIGURE 4.18: Storegga area

Also in this case, the landslide has not occurred yet, and our goal is to find the potential slip surface with the smallest value of F . For each method about 2500 geometrical configurations have been analyzed. In fig. 4.20 we show the results of the first 140 surfaces: they seem to follow two independent regular trends, blue points for $M\&P$ method and red points for the MLD method, where the smaller values of F are $F_{M\&P} = 1.59$ and

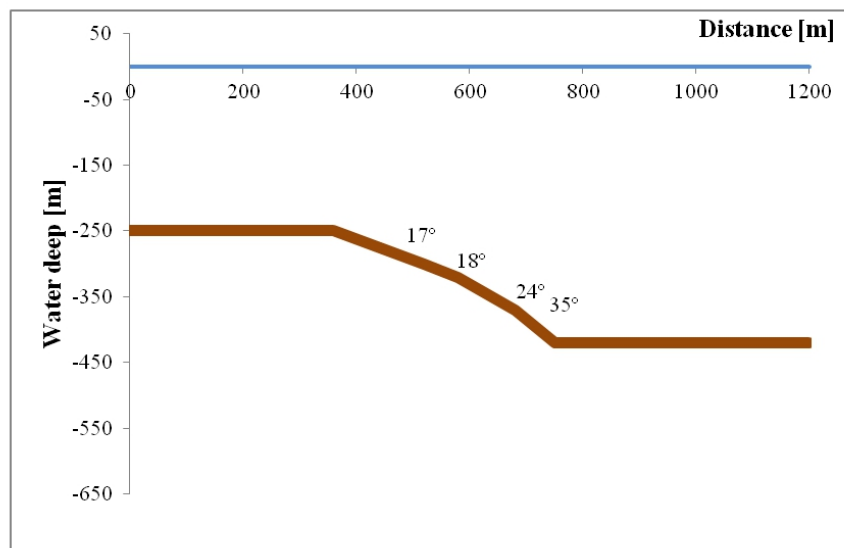


FIGURE 4.19: Section of the headwall of Storegga and average angles of the slope

$$F_{MLD} = 1.17.$$

Notice that these values do not correspond to the same slip surface. In fig. 4.21 we can see that for the *MLD* method the critical surface is deep (the blue dashed line), while for the *M&P* method the critical surface is shallow (the red line).

Starting from this observation, we investigated why there is such a big difference in the results, while this was not true for the analysis of the flat slope.

First of all, the problem is to understand if there are any differences in the single contributions of the forces taking into account that the module Slope/W uses the hydrostatic γ'

$$\gamma' = (\gamma_s - \gamma_w) \quad (4.5)$$

The plots 4.22, 4.23, 4.24 and 4.25 show that the functions $u(x)$, $D(x)$, $w(x)$ are the same and that $E(x)$ is similar. Instead the functions $X(x)$, (fig. 4.26), are totally different in the two methods, and such dissimilarity has origin exactly in the way the function $X(x)$ has been defined, 2.43 and 2.44.

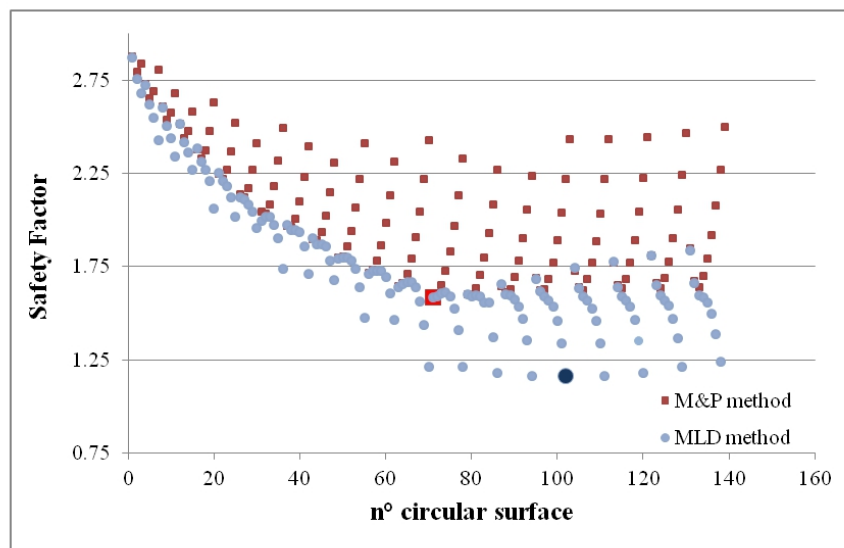


FIGURE 4.20: Trend of the safety factor obtained by changing the circular surface, that are numbered according to increasing radiuses. The blue and red highlighted points indicate the smallest value of F for the two methods: $F_{M\&P} = 1.59$ and $F_{MLD} = 1.17$

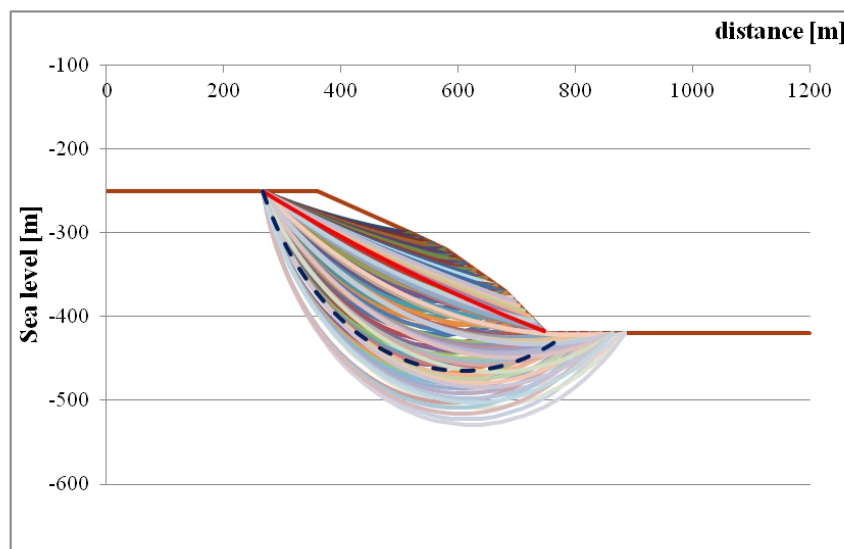


FIGURE 4.21: Circular trial surfaces: the red line is the critical surface for $M\&P$, the blue dashed line is the circular surface n.102 with $F=1.17$ (MLD)

The innovation of MLD method is to accept the multiplicity of possible values of F that can solve the equilibrium problem and to choose the correct value through the Minimum Lithostatic Deviation criterion, 2.6.

Indeed the solution obtained by using the $M\&P$ method is not wrong, but is one of the very many analyzed by the MLD method and rejected by the MLD criterion, since it

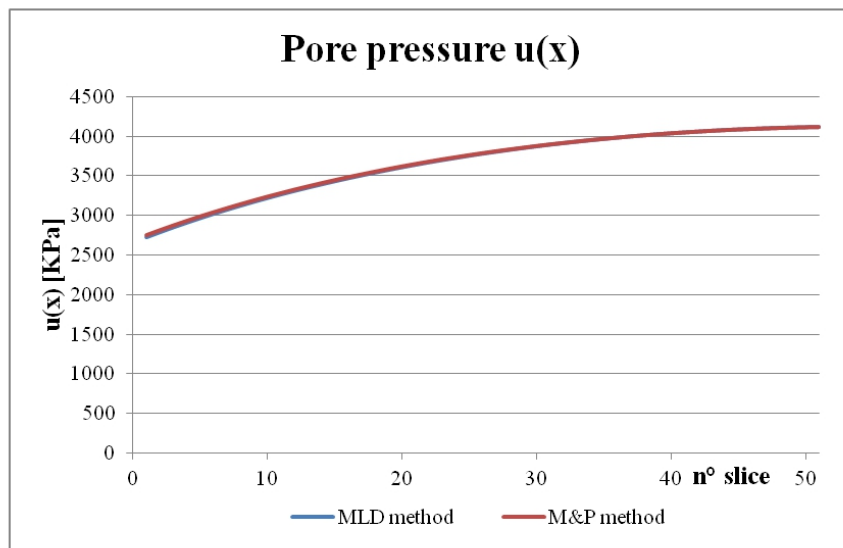
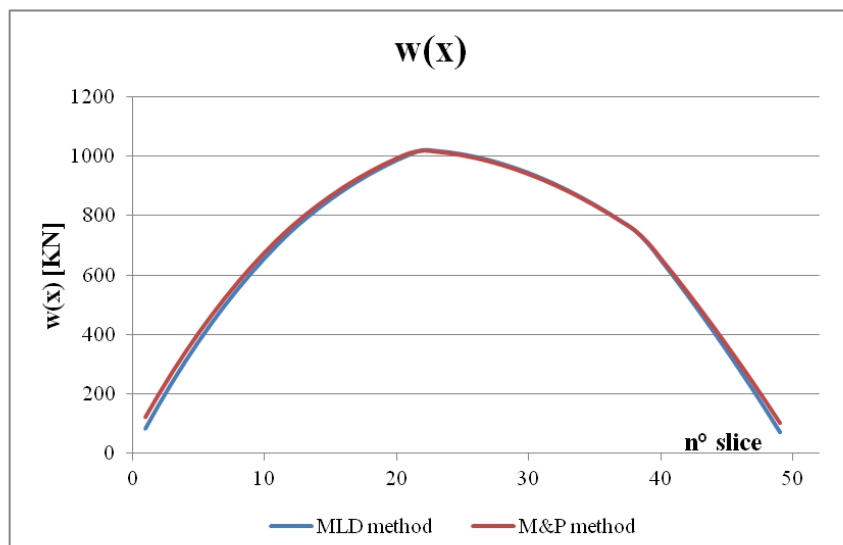
FIGURE 4.22: Comparison of the pore pressure $u(x)$ 

FIGURE 4.23: Comparison of the weight for every single slice

does not minimize the lithostatic deviation.

We can prove that if we truncate the expression of $X(x)$, that is given by

$$X(x, \lambda; F, q) = q \sin \left[\frac{\pi (x - x_i)}{L} \right] + \lambda_1 \sin \left[\frac{2\pi (x - x_i)}{L} \right] + \lambda_2 \sin \left[\frac{3\pi (x - x_i)}{L} \right] \quad (4.6)$$

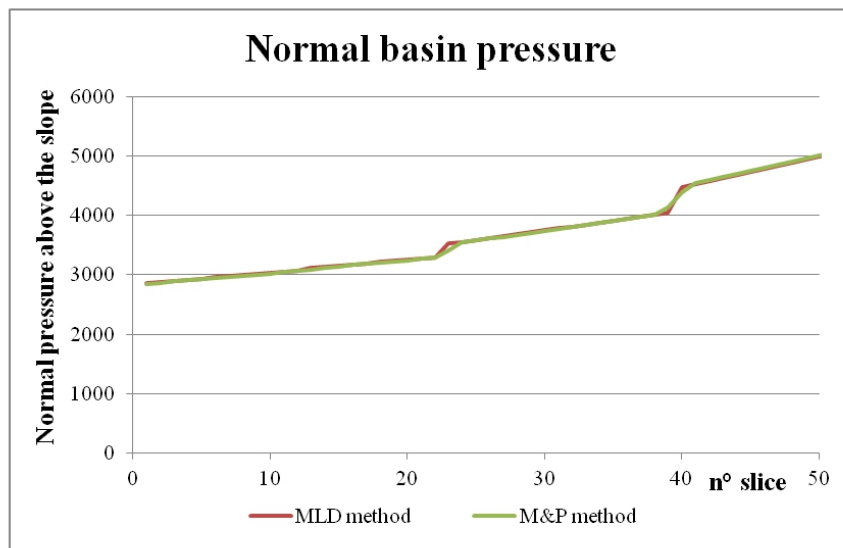
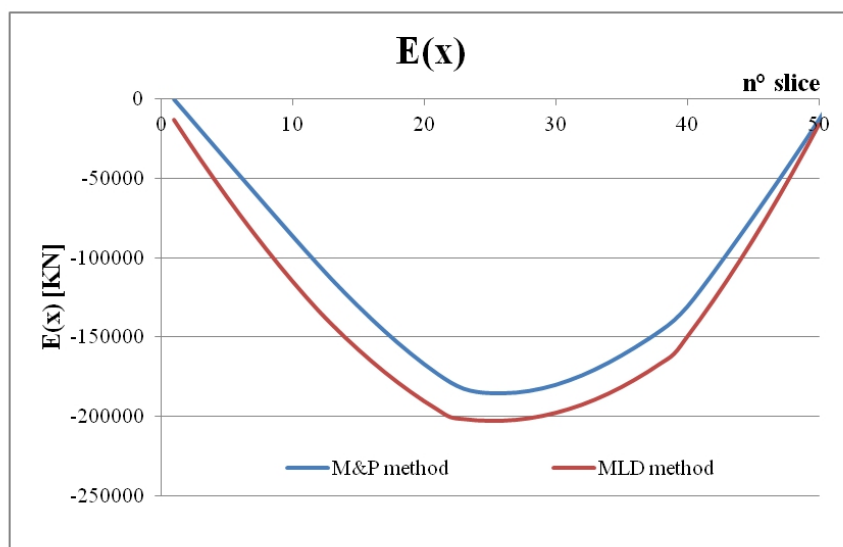


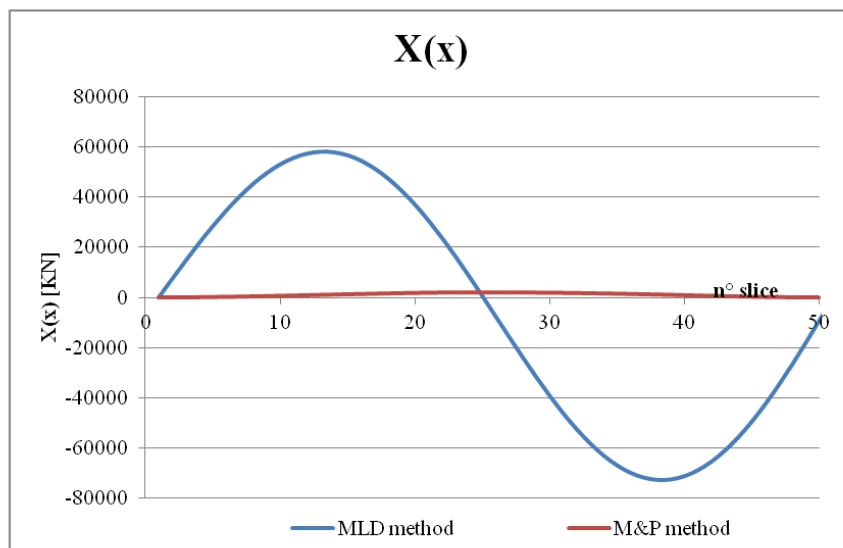
FIGURE 4.24: Normal pressure of the basin above the slope

FIGURE 4.25: Comparison of the functions $E(x)$

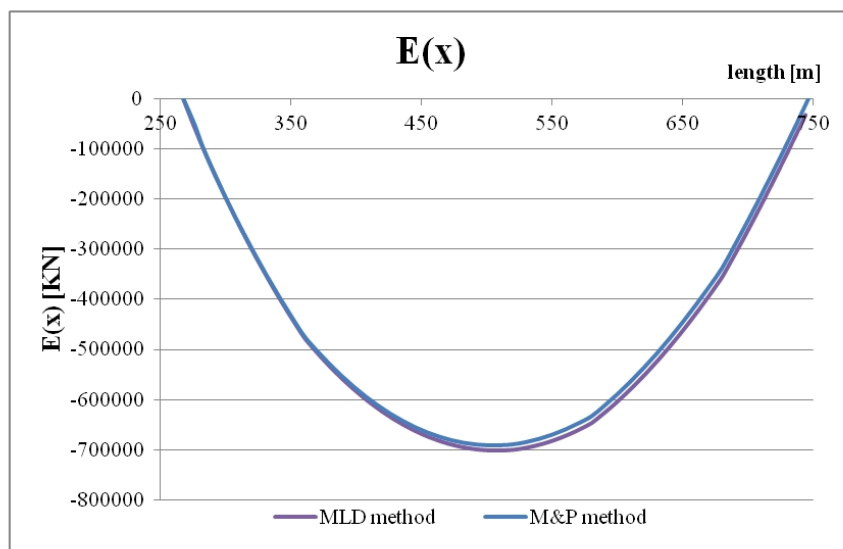
to the second term and we search a solution under the constraint that the $\lambda_1 = 0$, we obtain an expression of $X(x)$ more similar to the one of the *M&P* method.

So the values for the geometry n^o 102 (fig. 4.21), where $F_{MLD} = 1.17$, are

- $F_{M\&P} = 2.33$
- $F_{MLD\ modify} = 2.35$ with $\delta = 0.50194$

FIGURE 4.26: Comparison of the functions $X(x)$

Now the two F are similar, and if one compares the functions $X(x)$ and $E(x)$ of the two methods, one does not find big differences, 4.29 and 4.28

FIGURE 4.27: Comparison of the functions $E(x)$ with simplified MLD

But the values of δ are

- $\delta = 0.36273$ for $F_{MLD} = 1.17$
- $\delta = 0.50194$ for $F_{MLD\text{modify}} = 2.35$

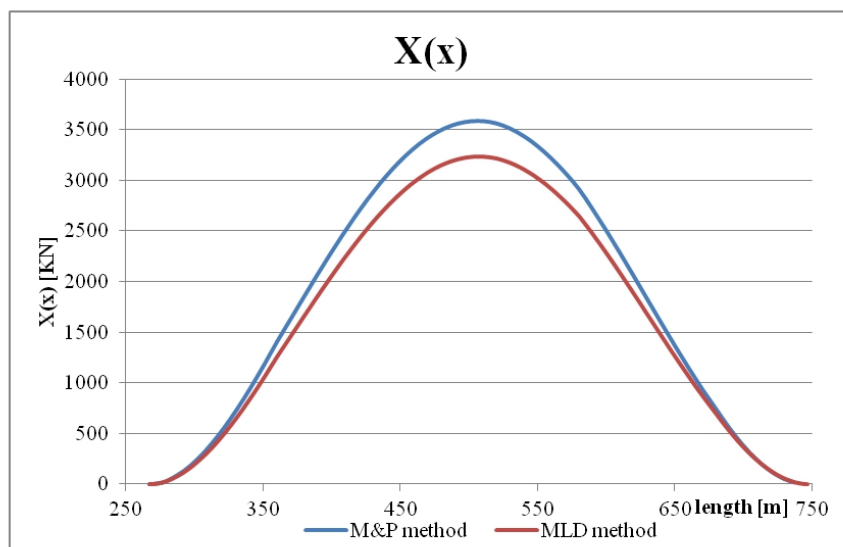


FIGURE 4.28: Comparison of the functions $X(x)$ with simplified *MLD*

and for this reason the *MLD* criterion selects the value $F=1.17$. This is an important result, given that the two values of F are different, and from the results obtained, we decided to continue our analysis only with the *MLD* method.

Another key feature of the *MLD* method is that it was also developed to study the stability of slopes with a complex stratigraphy. In the case of Lofoten, we have considered only a homogeneous body, but now, since the value of F is very low, it is worth to make a more accurate analysis and to take into account a profile in its present geological structure. As mentioned earlier, the crown of the Storegga landslide is composed of some layers made mainly of glacial sediments separated by overconsolidated clay. The presence of clay is particularly important, since numerous studies demonstrate that the likely sliding surface might be determined by the shape of the clay layers. As was observed in the analysis of the Vajont, one of the causes of failure for a slope is the destabilizing pressure along a clay layer, due to its low permeability and the increasing of the pore pressure for a saturated soil.

The results of F are 2.38 for the red circular surface and 1.57 for the blue circular surface: they indicate that the likely slip surface is of the shallow type, while the deep type is more stable.

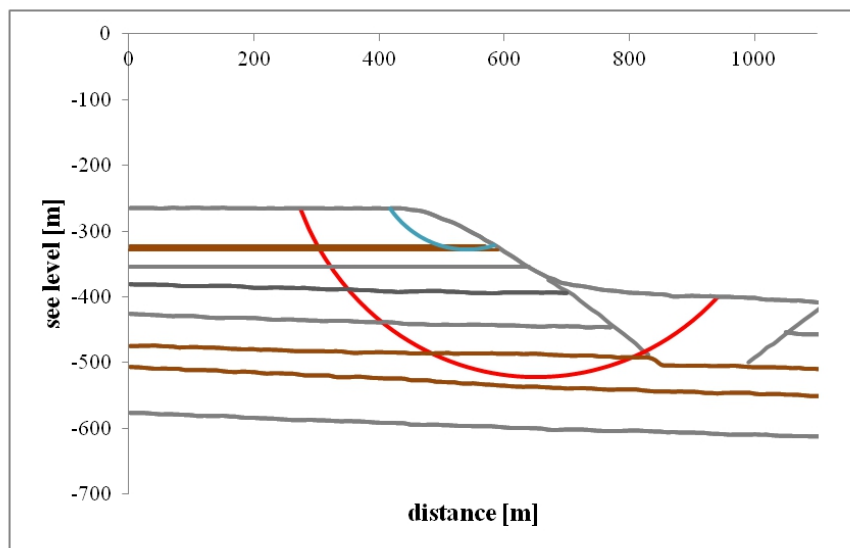


FIGURE 4.29: Typical cross-section of the headwall of Storegga: the succession of layers is composed by glacial till (grey lines) and marine clay (brown lines). The blue and red lines represent the trial slip surface that passes through the clay layers.

4.2.1 Summary of the analysis of the Storegga headwall

The main objectives of the previous section were to assess the present conditions of stability of the Storegga crown characterized by high slope angle, about 30° , and to observe if the use of the *MLD* method and of the *M&P* method lead to considerable differences in the results. The slope was considered first as a homogeneous soil and in a second stage as a series of layers: in both cases the value of F was greater than 1, confirming that in the current situation the slope is stable.

Regarding the second item, we found that the *M&P* method and the *MLD* methods provide substantially different results, but that the *MLD* method finds almost the same solution if certain constraints are imposed. In the *MLD* principle optics, however, the *M&P* solution is worse since it does not minimise the lithostatic deviation.

Chapter 5

The Stability Charts

In chapters 3 and 4 we have shown the comparison of the *MLD* method with other methods based on the limit equilibrium principle, and we have further noticed that some satisfy all of the boundary conditions (namely *MLD* and *M&P*), while others satisfy only some of them (namely *Bishop* and *Janbu*).

At this point we can say that the *MLD* method appears to be a very good tool for the stability analysis: it allows us to reconstruct the critical conditions in cases where the landslide has already occurred (see the Vajont case), and to investigate the current equilibrium conditions along slopes, even submarine, analysing the weight of potential destabilizing factors such as the seismic load or the excess pore pressure (see the Norwegian cases).

In this last chapter, we use the *MLD* method for the computation of stability charts, that is a well-known tool used in the engineering field. Our main goal is to explore the correctness and the adequacy of the commonly used stability charts. The main observation is that they are mainly exploited to estimate the stability of embankment, dikes and dams, and our scope is to consider if they are suitable also to analyse the stability of slopes of geophysical interest.

The preliminary phase is part of a work illustrated in a poster for the EGU 2013 General Assembly (Paparo and Tinti, 2013)

5.1 Taylor's stability charts

Stability charts are a known tool used to make preliminary estimation of the stability of a slope. The method is graphic and easy to use, without the need to make complicated calculations.

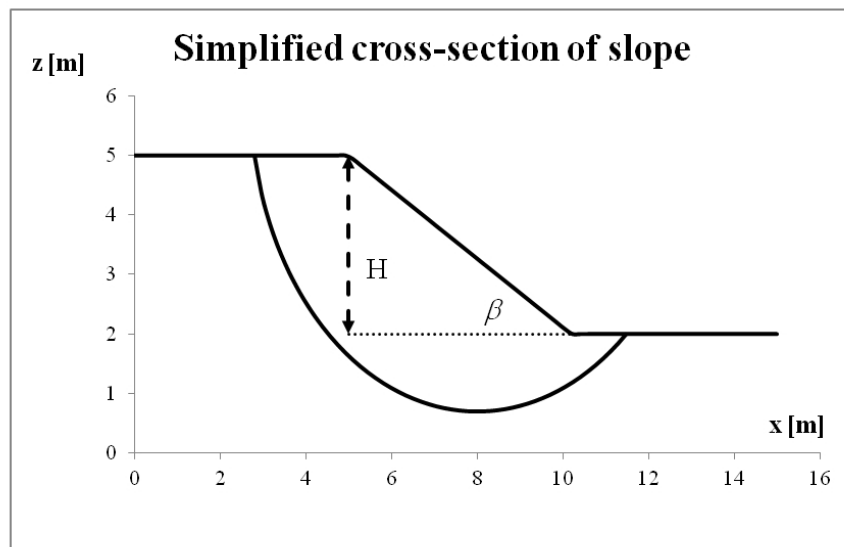


FIGURE 5.1: Example of 2-D slope: simplification of a sliding body for building stability charts: H is the height, β is the inclination of the slope.

The charts were introduced for the first time by Taylor (1937). They consist in a set of curves, drawn on the basis of some relations between the geometric and geotechnical parameters including the safety factor, and that were deduced both on experimental data and on calculations.

The geometry (fig. 5.1) of the slope is very simplified: it is a 2D plane incline with inclination angle β and height H . A further possible parameter in some models is the depth of an underlying stiff layer, that is assumed to resist to any failure, that is a layer into which the slip surface cannot propagate. However, we follow the original Taylor's model that takes into account only homodegenous soils with no stratification.

For the geotechnical component of soil, Taylor defines a mobilized cohesion

$$c_m = \frac{c}{F} \quad (5.1)$$

and a mobilized angle of friction

$$\tan\phi_m = \frac{\tan\phi}{F} \quad (5.2)$$

where F is the safety factor. For a frictional and cohesive soil, the mobilised parameters satisfy the trivial relation

$$F = \frac{c}{c_m} = \frac{\tan\phi}{\tan\phi_m} \quad (5.3)$$

Taylor calculated the factor of safety for a large number of slopes over a wide range of slope angles and for each of them computed also the slip surface. He found (which is the essence of the stability chart concept) that, given the mobilized friction angle ϕ_m , then the dimensionless number N_s defined as the ratio of the mobilized cohesion over the product γH is only a function of the slope angle β , that is:

$$\frac{c_m}{\gamma H} = N_s(\beta; \phi_m) \quad (5.4)$$

where $\gamma = \rho g$ is the unit weight of the soil. Taylor designated N_s as the stability number and in a Cartesian plane (N_s, β) he drew curves of N_s as a function of β for several different values of the mobilized friction angle, calling this a stability chart, since it condenses all the information needed to estimate the safety factor of a slope without repeating all calculations Taylor made.

In practice there are different ways to derive the value of F from the stability charts.

- The first is described by the following steps, (Tanpure and Koranne, 2012):
 1. for a given slope with β and H , we assume a trial value of F and calculate ϕ_m ;
 2. from the stability chart we read the value of N_s corresponding to β and ϕ_m ;

3. we use the inverse formula

$$H' = \frac{c_m}{\gamma N_s} \quad (5.5)$$

to calculate the trial slope height H' corresponding to the assumed factor of safety;

4. if the calculated value of H' is within an acceptable distance from the actual height H , the assumed value of the trial factor of safety represents the factor of safety of the slope;
 5. if the calculated value of H' is not within the desired acceptable range, the process is repeated with a new assumed value of the factor of safety until the recomputed value of H falls within that range.
- The second method is a simple graphical approach (Tanpure and Koranne, 2012):
 1. we take a reasonable F and calculate ϕ_m ;
 2. we read the corresponding value of the stability number N_s from the stability chart;
 3. we calculate c_m from N_s and then we calculate $F' = c/c_m$.
 4. we repeat the process for at least two other assumed values of F , so that at least three couples of F and F' are obtained.
 5. we plot the calculated points of F' vs. F in a (F', F) coordinates plane and draw a curve through the points;
 6. we draw the bisectrix of the first quadrant that represents the line where $F = F'$
 7. the searched factor of safety for the slope is the value corresponding to the intersection of the drawn line with the bisectrix.
 - The last method is another iterative procedure like the first method
 1. for a given slope with β and H , we assume a trial value of F^1 and calculate ϕ_m^1 , where the index 1 denotes the first element of the iteration
 2. we read the corresponding value of the stability number N_s^1 ;

3. since N_s and ϕ_m are linked by the following relationship:

$$N_s = \frac{c_m}{\gamma H} = \frac{c}{\gamma H F} = \frac{c}{\gamma H \tan \phi} \tan \phi_m \quad (5.6)$$

after introducing the parameter λ that is constant for a given slope:

$$\lambda = \frac{c}{\gamma H \tan \phi} \quad (5.7)$$

we can find the new value of ϕ_m^2 from the relationship:

$$\tan \phi_m^2 = N_s^1 / \lambda \quad (5.8)$$

and the new value of F^2 as:

$$F^2 = \frac{\tan \phi}{\tan \phi_m^2} \quad (5.9)$$

The above relations can be generalized for the k -th step of the iteration:

$$\tan \phi_m^k = \lambda^{-1} N_s^{k-1} \quad (5.10)$$

and

$$F^k = \frac{\tan \phi}{\tan \phi_m^k} \quad (5.11)$$

4. the iterations finish when

$$F^k \simeq F^{k-1} \quad (5.12)$$

In practice, as already explained above, a stability chart is a set of curves of N_S plotted vs. the slope angle β for constant ϕ_m , where the mobilized friction is seen as a parameter. However, one can also take ϕ_m as an independent variable and consider that the stability number is a function of two independent variables, i.e. $N_S \equiv N_S(\beta, \phi_m)$; and after a suitable procedure of curve fitting, one can show that N_S can be suitably approximated by a polynomial of third degree in β and of second degree in ϕ_m (Easa and Vatankhah, 2011), that is:

$$N_S = 0.042186 + 0.004905\beta - 6.44 \cdot 10^{-5}\beta^2 + 4.07 \cdot 10^{-7}\beta^3 - 0.00807\phi_m + 3.41 \cdot 10^{-5}\beta\phi_m + 5.94466 \cdot 10^{-5}\phi_m^2 \quad (5.13)$$

where the angles are expressed in degrees. After considering the expression 5.6 for N_S and using the approximation $\tan\phi_m \sim \phi_m$, one can rewrite the previous equation as:

$$\lambda\phi_m \frac{\pi}{180} = 0.042186 + 0.004905\beta - 6.44 \cdot 10^{-5}\beta^2 + 4.07 \cdot 10^{-7}\beta^3 - 0.00807\phi_m + 3.41 \cdot 10^{-5}\beta\phi_m + 5.94466 \cdot 10^{-5}\phi_m^2 \quad (5.14)$$

where λ was already introduced. Once β is known, this is a quadratic equation for ϕ_m , that can be easily solved:

$$\phi_m = \frac{-b - (b^2 - 4ac)^{\frac{1}{2}}}{2a} \quad (5.15)$$

where

- $a = 5.94466 \cdot 10^{-5}$
- $b = -0.00807 + 3.41 \cdot 10^{-5}\beta - \lambda \frac{\pi}{180}$
- $c = 0.042186 + 0.004905\beta - 6.44 \cdot 10^{-5}\beta^2 + 4.07 \cdot 10^{-7}\beta^3$

Knowing the value of ϕ_m , one finds eventually:

$$F = \frac{\tan\phi}{\tan\left[\frac{-b - (b^2 - 4ac)^{\frac{1}{2}}}{2a}\right]} \quad (5.16)$$

This procedure is straightforward and has the further advantage that it is not based on any graphical reading, but only on calculations.

Before concluding this section, it is worth pointing out that the safety factor of a slope that is computed by means of the stability charts has to be meant as the smallest safety factor for a slope. The idea is that, given a slope, one can consider an infinite number of potential slip surfaces, and every one of these surfaces is associated to its own safety factor. The charts provide the smallest value of F , that is associated to that slip surface that is closest to instability. If it results that $F > 1$, then all possible slip surfaces are stable and the slope itself is stable. On the contrary, if, by using the charts one finds that $F < 1$, then there is at least one slip surface that is unstable, and the slope is prone to fail. Therefore, in addition to knowing whether a slope is stable or not, it is also of value to obtain the geometry of the slip surface that is most prone to failure. This is the second essential piece of information and will be treated in the following section. Here we will follow the classical approach of Taylor, but we will also take into account the variants elaborated later and even in recent times Janbu (1954, 1973), Bishop (1955), Bishop and Morgenstern (1955), Morgenstern and Price (1965), Spencer (1967), Bell (1968), Sarma (1987), Michalowski (1999, 2002), Baker (2003), Baker and Tanaka (1999), Easa and Vatankhah (2011).

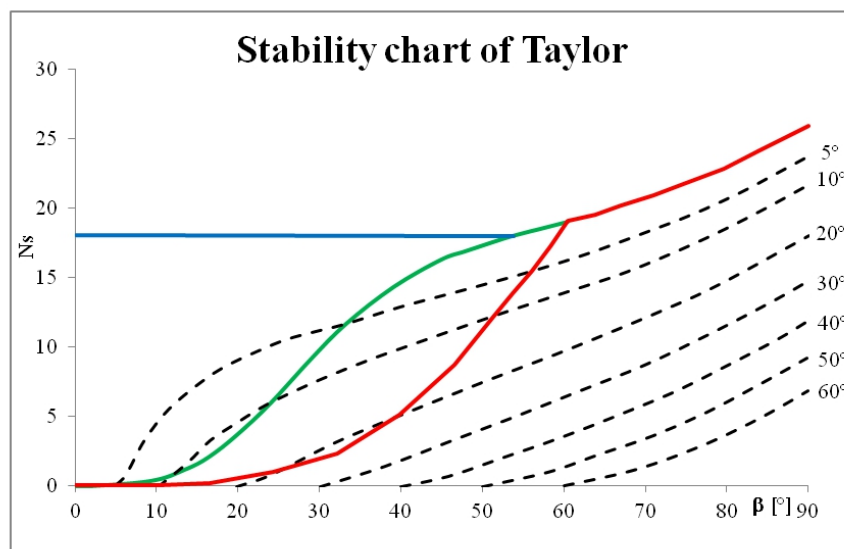


FIGURE 5.2: Taylor's stability chart for uniform slopes. The dashed lines are the Taylor's curve corresponding to a given value of ϕ_m . Colored lines delimit regions within which the critical slip surface takes a specific shape: between blue and green lines, slip surfaces are midpoint circles; between green and red lines, slip surfaces are deep toe circles and under the red line slip surfaces are shallow toe circles.

5.1.1 The geometry of the slip surface

The geometry of the slip surface can be an arc of circumference (Baker, 2003, Taylor, 1937) or a spiral (Michalowski, 2002). Following Taylor's analysis we identify two main classes of surfaces:

- Toe circles
- Midpoint (or base) circles

The toe circle is a failure surface that passes through the landslide toe. This category can be divided in two further sub-classes, according to the thickness of the slope: the shallow toe circle, whose deepest point, z_{min} coincides precisely with the toe (fig. 5.3), and the deep toe circle, whose deepest point z_{min} is located below the toe (fig. 5.4). Instead, if the failure surface passes over the toe, the critical circle is known as midpoint or base circle 5.5.

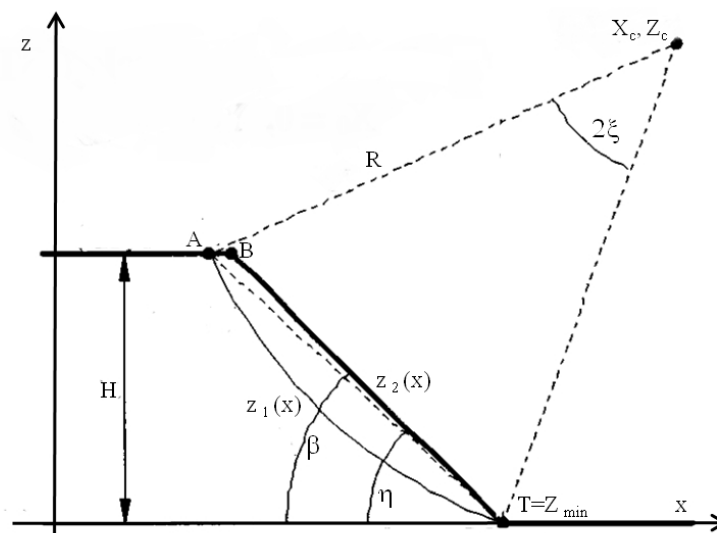


FIGURE 5.3: Shallow toe circle: $z_1(x)$ and $z_2(x)$ define respectively the bottom and upper curves of the landslide. R is the radius of the circular slip surface with center coordinates (X_c, Z_c) . H and β are the height and the inclination of the slope. T is the landslide toe, η is the inclination of the chord connecting the start- and end-point of the slip surface and 2ξ is the central angle of the chord AT (Baker, 2003).

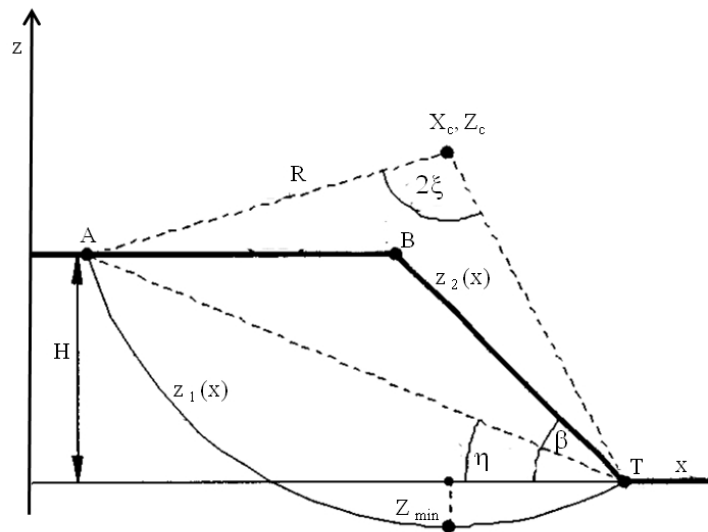


FIGURE 5.4: Deep toe circles: see fig. 5.3 , (Baker, 2003).

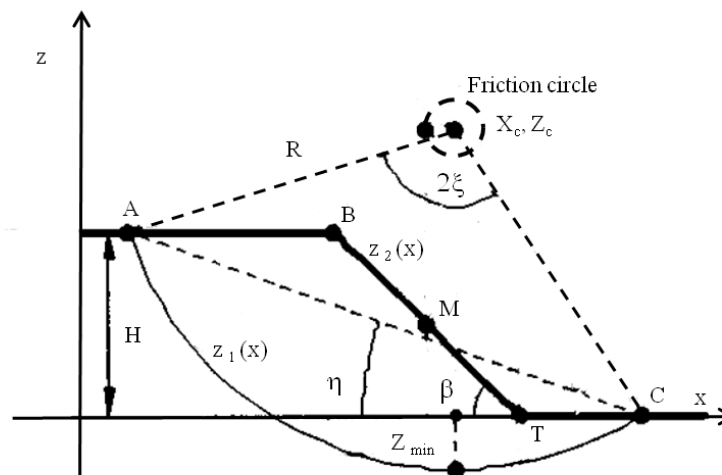


FIGURE 5.5: Base circle: see fig. 5.3. The particularity in this failure mode is in the end-point C that lies beyond the toe. The friction circle shows how much the center of the sliding surface is moved with respect to the center of the slope M, (Baker, 2003) .

Taylor defines the radius of the slip surface as

$$R = \frac{H}{2 \sin \eta \sin \xi} \tag{5.17}$$

and the z_c coordinate of the center as

$$z_c = R \cos(\eta - \xi) \quad (5.18)$$

while the x_c coordinate differs if we consider a toe or a midpoint circle. From the requirement that the toe circles pass through the toe point T of the slope, one gets

$$x_c = R \sin(\eta - \xi) \quad (5.19)$$

while for the midpoint circle, Taylor gives the expression:

$$x_c = \frac{R}{2 \tan \beta} - \sin \phi_m \quad (5.20)$$

This last relation for x_c is due to Taylor's observation, which is the consequence of the numerous calculations and experimental data, that the critical conditions for base circles occur when the friction circle is tangential to a vertical line passing through the midpoint M of the slope, 5.5 (Baker, 2003).

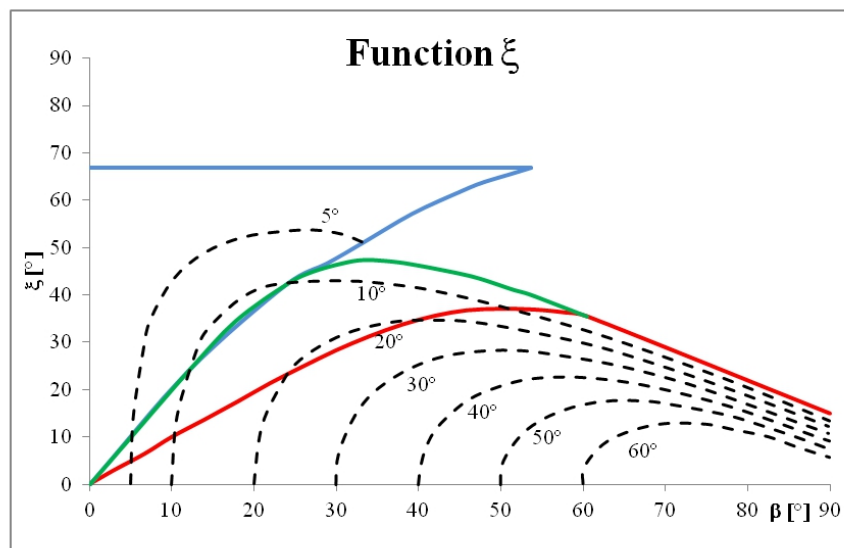


FIGURE 5.6: The function $\xi(\beta, \phi_m)$. The dashed lines are the Baker's curves corresponding to different values of ϕ_m . The colored lines bound regions with different shapes of the critical slip surface: between blue and green lines one finds base or midpoint circles, between green and red lines one finds deep toe circles, while under the red line one finds shallow toe circles

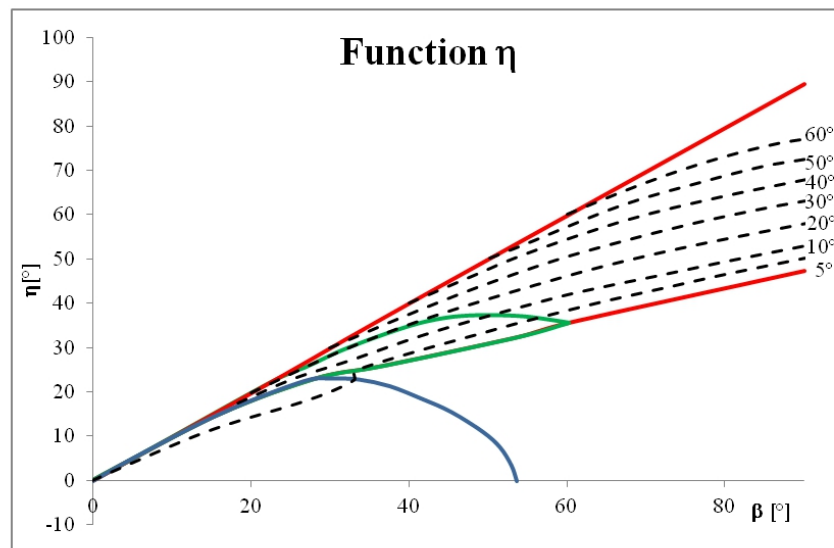


FIGURE 5.7: The function $\eta(\beta, \phi_m)$: see fig 5.6

In the previous formulas, the radius and the coordinates of the center of the slip surface are expressed in terms of the variables η and ξ , but Taylor did not specify the way to easily determine them for a given slope. This problem was addressed and solved only recently Baker (2003). Baker builds two charts where η and ξ are curves expressed in terms of the inclination β and the parameter ϕ_m (figs. 5.6 and 5.7). The procedure is simple: to estimate the smallest value of F for a slope, one first computes the value of ϕ_m 5.2. Through Baker's charts, one can use this value of ϕ_m also to read the values of ξ and η corresponding to a given value of the variable β and of the parameter ϕ_m , and eventually one computes the radius and the center. The solution is unique and identifies univocally the circular slip surface.

5.1.2 Analysis of Taylor's and Baker's charts

The charts of Taylor and Baker are based on the concept that for a simple slope one can define an adimensional number (the stability number N_S) that depends only on β and on ϕ_m . Though this is based on calculations and experimental data, this is indeed not strictly true since the equations 2.6, 2.7 and 2.8 are too complex to be amenable to the simple form of $N_S(\beta, \phi_m)$. The stability charts of Taylor can therefore be considered at most as a tool to find a first approximated value for the factor of safety. The question

is to evaluate how good this approximation is. In other words, for a given slope one can compute the value of F through the joint Taylor-Baker's charts and compute it also through a more accurate method and eventually compare the two solutions. In this work, we use the *MLD* method that we showed to provide reliable solutions for the safety factor. Our strategy here consists in taking a slope of the kind examined by Taylor (i.e. with a geometry univocally determined by the slope angle β and the height H) to compute the factor of safety F by means of the *MLD* method and to use the found value of F to compute the stability number N_S . Eventually this can be compared with the stability number one reads on the Taylor's stability chart, and evaluate the amount of the discrepancy. We will see that points that should belong to the same Taylor's curve result instead to be spread around the curve though they do not fall far from it. This confirms that Taylor's curve do not provide the correct solution, but only an approximate one.

A systematic exploration of all possible cases implicitly treatable through a stability chart approach would require too much computing time and is not feasible. In the second chapter we have seen that, given a slope and a preselected slip surface, the *MLD* method examines a number of configurations n expressed by 2.49 to find the safety factor.

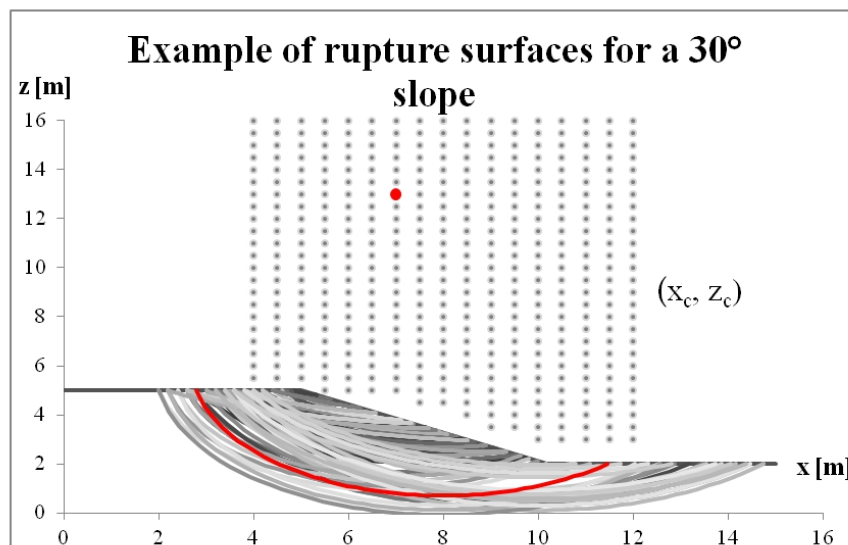


FIGURE 5.8: Circular rupture surfaces investigated for stability calculations. The gray points are the circumference centers. The center and the arc corresponding to the lowest value of F are in red. Notice that horizontal and vertical scales are different.

In the present case, the slip surface is not known a priori, but is one of the unknowns of the problem. In fact we want to find the one corresponding to the smallest value of F , which implies that we have to investigate a space of configurations by varying three more variables, namely the radius of the circumference and the two coordinates of the centers. Consequently, for a single point of the stability charts we should explore a total of N configurations,

$$N = n * nR * nC \quad (5.21)$$

where nR is the number of trial radiuses and nC is the number of the trial circle centers (x_c, z_c) , fig. 5.8. Considering that n is in the order of 10^5 , the final result is that N is reasonably in the order of 10^8 , which is too large to allow a systematic analysis.

For this reason, we have chosen to avoid recomputing the stability charts, but to analyse only some selected cases: in practice we have selected 4 cases for each curve of ϕ_m in correspondence of the inclination angles $\beta = 30^\circ$ and 60° .

Fig. 5.9 shows what we anticipated before: the four points, that in line with Taylor's theory should coincide and be placed perfectly along of the same curve, have slightly different values of N_s : the discrepancy is suggestively increasing with the slope inclination β and, if one considers the corresponding values of F , one sees that they vary from 5% to about 10% with respect to the expected values of Taylor. These differences are significant especially if slopes are close to critical conditions, that is close to instability.

As a conclusion, we can state that Taylor's charts are useful in a preliminary stage of stability analysis, because they enable one to make an acceptable estimate of F , but for a better accuracy, which is a need for critical slopes, one has to use more accurate methods, like the *MLD* method.

In light of these results, we have carried out further investigations with two main goals: the first is to understand which parameters affect most the equilibrium conditions; and the second how much the results vary if the stability charts are applied to cases of geophysical interest rather than cases of geotechnical interest.

We have chosen only one point of the curve, in correspondence of $\beta = 30^\circ$ and $\phi_m = 15^\circ$. For this first round of cases, the selected value of γ is equal to $25 \text{ KN}/\text{m}^3$. We

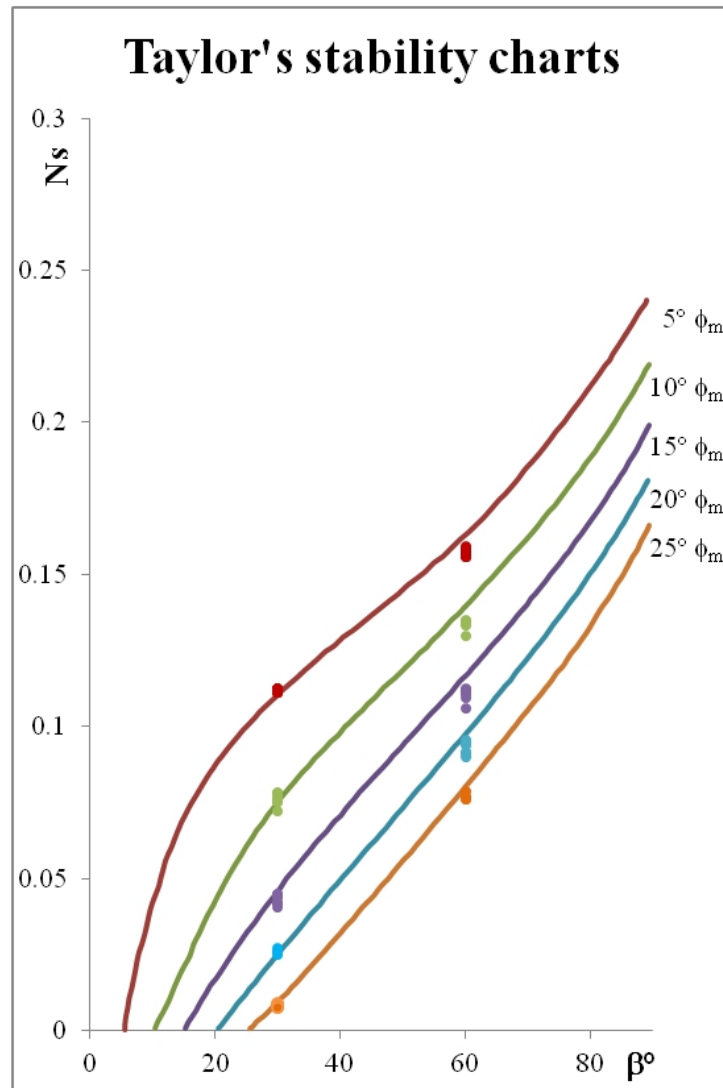


FIGURE 5.9: Comparison of the MLD results, colored points, with the curves of Taylor. The cases analyzed are in correspondence of $\beta = 30^\circ, 60^\circ$. We show that the resulting points do not fall exactly on the curves, also if they follow the curve's trend. The discrepancy grows with the increase of the inclination, from about 5% for $\beta = 30^\circ$, up to 10% for $\beta = 60^\circ$

have taken three different values for the slope height, i.e. $H \equiv [10\text{ m}, 75\text{ m}, 130\text{ m}]$. We have then selected values of cohesion by imposing that the slopes are close to instability conditions. To reduce the number of configurations to explore in order to find the slip surface we have made use of Baker's charts, according to which the values of ξ and η are respectively 35.09° and 22.27° . Consequently, with the aid of 5.17, 5.18, 5.19 and

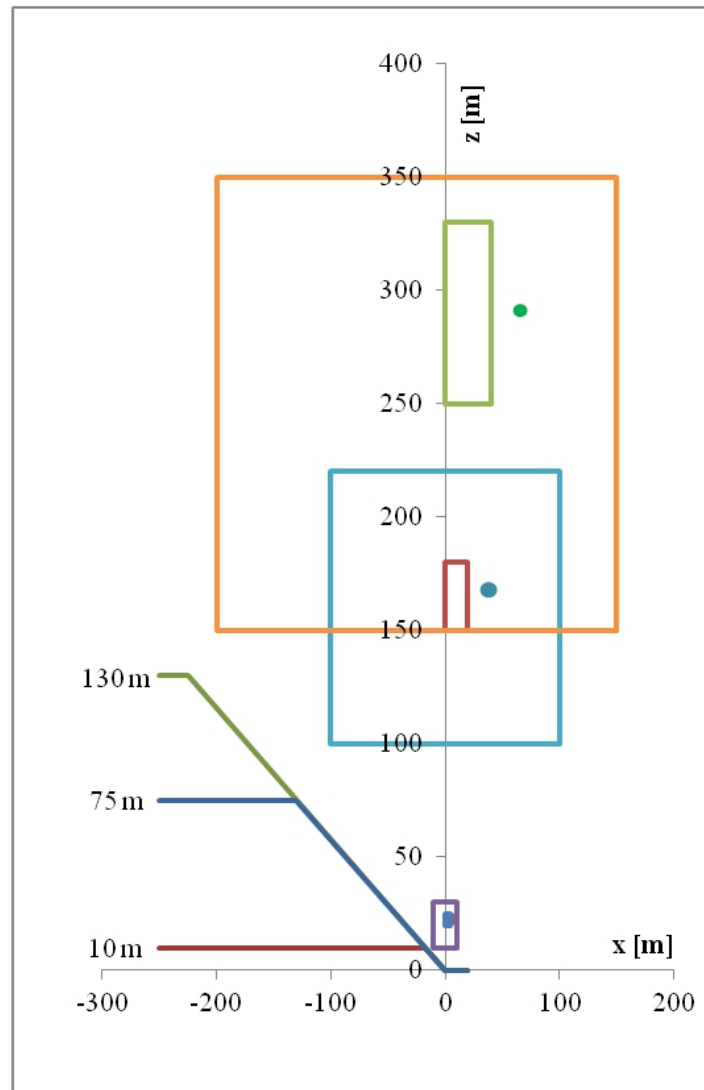


FIGURE 5.10: The three configurations with $\beta = 30^\circ$. The three marked points indicate the centers found through Baker's charts. The big rectangles (violet, blue and orange) are the areas explored to find MLD slip circle centers; the little rectangles (blue, red and green) are the zones swept to refine the MLD research. The last areas are shown in fig. 5.11

5.20, we have

- $H = 10 \text{ m}$

$$\begin{aligned} R &= 22.95 \text{ m} \\ x_c &= 5 \text{ m} \\ z_c &= 22.4 \text{ m} \end{aligned} \tag{5.22}$$

- $H = 75 \text{ m}$

$$\begin{aligned} R &= 172 \text{ m} \\ x_c &= 38 \text{ m} \\ z_c &= 167 \text{ m} \end{aligned} \tag{5.23}$$

- $H = 130 \text{ m}$

$$\begin{aligned} R &= 298 \text{ m} \\ x_c &= 66 \text{ m} \\ z_c &= 290 \text{ m} \end{aligned} \tag{5.24}$$

We have restricted the search for the slip surface in the neighborhood of the above Baker's solutions. Fig. 5.10 shows the three slopes, and the highlighted points are the centers of the Baker slip surfaces. The *MLD* search has been first carried out with low resolution in areas around the Baker's centers and then refined to find the one corresponding to the minimum value of the safety factor. If we analyze the three cases with the *MLD* method, we obtain the following solutions in the larger areas with rough resolution:

$$\begin{aligned} H = 10 \text{ m} \quad F_{Taylor} &= 0.96 \quad F_{MLD} = 0.947 \\ H = 75 \text{ m} \quad F_{Taylor} &= 0.96 \quad F_{MLD} = 0.955 \\ H = 130 \text{ m} \quad F_{Taylor} &= 0.96 \quad F_{MLD} = 0.962 \end{aligned} \tag{5.25}$$

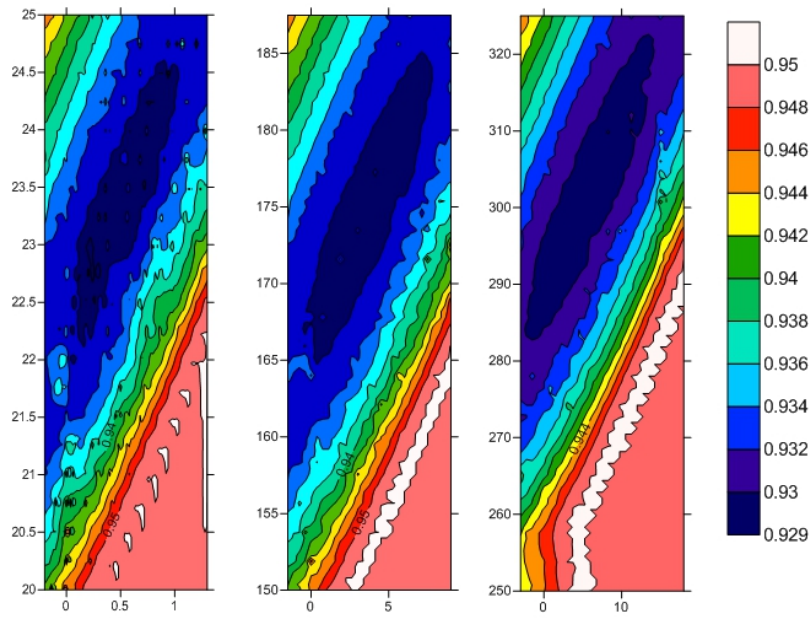


FIGURE 5.11: Rectangles (blue, red and green) shown in fig. 5.10. Each point in the rectangle represents the center coordinates of a set of trial slip surfaces with different radiuses. The value of F is the lowest value computed according to the *MLD* method. The first rectangle is for $H = 10\text{ m}$, the second for $H = 75\text{ m}$ and the third for $H = 130\text{ m}$. The slip surfaces are similar to the ones obtained by Taylor. The values of F are slightly smaller than those obtained with Taylor's chart

After we make a refinement of the search with improved resolution (fig. 5.10), we find even lower values of F , (figs. fig. 5.10 and 5.11):

$$\begin{aligned}
 H = 10\text{ m} \quad F_{Taylor} &= 0.96 \quad F_{MLD} = 0.929 \\
 H = 75\text{ m} \quad F_{Taylor} &= 0.96 \quad F_{MLD} = 0.931 \\
 H = 130\text{ m} \quad F_{Taylor} &= 0.96 \quad F_{MLD} = 0.931
 \end{aligned}
 \tag{5.26}$$

If we repeat the same analysis with a different value of γ (i.e. $\gamma = 15\text{ KN/m}^3$), we note a further significant lowering of the F values found with the *MLD* method

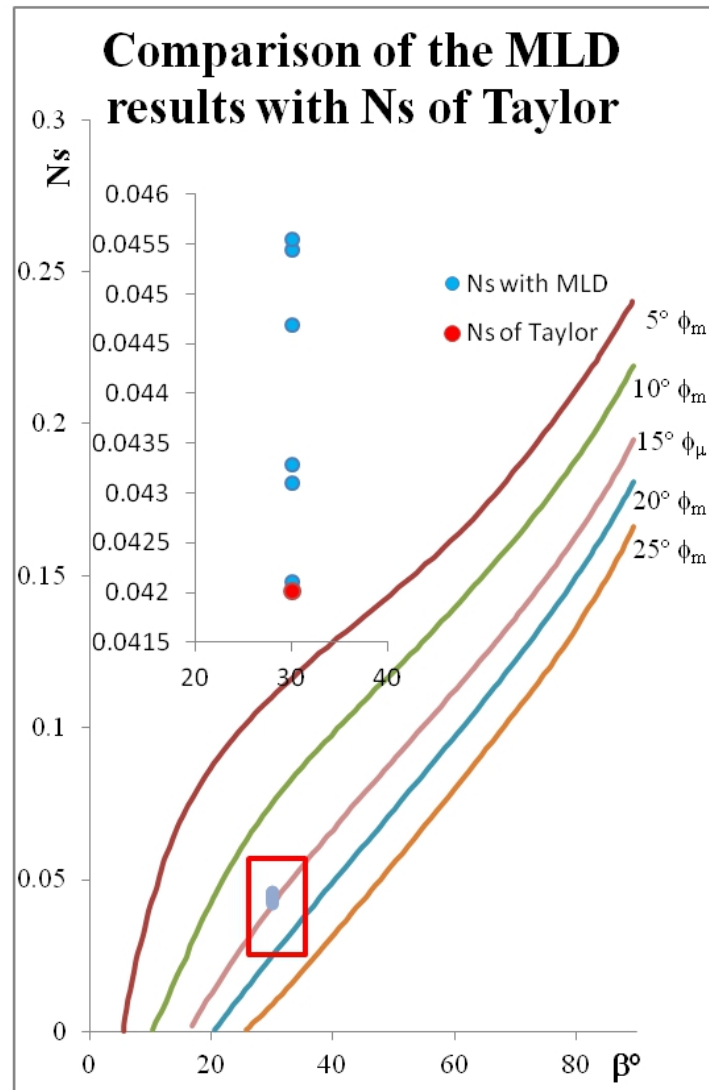


FIGURE 5.12: Numbers of stability obtained from values of F_{MLD} (blue dots) vs. $N_{sTaylor}$ (red dots). The cases explored are six: three corresponding to $\gamma = 15 \text{ KN/m}^3$ and three corresponding to $\gamma = 25 \text{ KN/m}^3$ and all sharing the same Taylor's $N_{sTaylor}$. The largest discrepancy is about 8%

$$\begin{aligned}
 H = 10 \text{ m} \quad F_{Taylor} = 0.96 \quad F_{MLD} = 0.883 \\
 H = 75 \text{ m} \quad F_{Taylor} = 0.96 \quad F_{MLD} = 0.885 \\
 H = 130 \text{ m} \quad F_{Taylor} = 0.96 \quad F_{MLD} = 0.898
 \end{aligned}
 \tag{5.27}$$

From the results obtained, we can draw two conclusions. First, the equilibrium conditions depend on the geometrical structure and the parameters of the soil, but the approach cannot be simplified so much as instead suggested by Taylor's stability charts. In Taylor's diagram, cases that should be represented by the same point are indeed well separated if the analysis is carried out with some more sophisticated method (like *MLD*) and safety factors are different as well. Second, changes of the geometrical scale (i.e. passing from $H = 10\text{ m}$ to $H = 130\text{ m}$) do change the stability number and the safety factor but much less than changes in the unit weight γ that seems to be a very important factor. In addition, since the general trend of Taylor's curves is confirmed, it is also confirmed the important role of the slope inclination and of the friction angle. In conclusion, Taylor's and Baker's charts are useful to highlight the relevance of certain parameters, but do obscure the relevance of others (like the unit weight), and have to be considered a rough approximation of the solution to the slope stability problem.

5.2 Michalowski's stability charts

As mentioned earlier, a huge amount of work has been done to improve the Taylor's stability charts. One of the most important contributions is that of Michalowski (1999, 2002) who produced his own charts. The main purpose of our analysis is to demonstrate that, also in this case, these charts represent an oversimplification of the stability analysis and provide rough estimates of the safety factor for the slope.

Michalowski built his charts by using a kinematic approach for the limit equilibrium analysis applied to a rigid rotational failure mechanism, and referring to (Chen et al., 1969), assumed that the slip surface is an arc of a logarithmic spiral.

Following an idea of Bell (1966), he wanted to build charts from which F can be derived directly, without any iterative process (Bell, 1966, Bishop and Morgenstern, 1955, Cousins, 1978, Singh, 1970). To this purpose he defined a new N_S independent from F , that he obtained from the N_S of Taylor by dividing it by the function $\tan \phi_m$, that is:

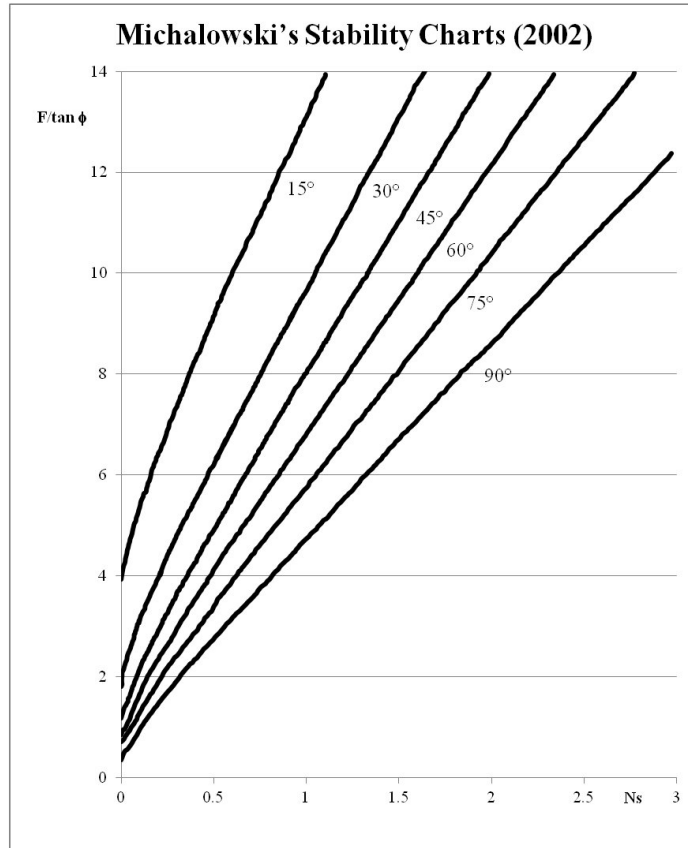


FIGURE 5.13: Stability charts of Michalowski for unsaturated soil

$$N_S = \frac{c}{\gamma H F \tan \phi_m} = \frac{cF}{\gamma H F \tan \phi} \quad (5.28)$$

which leads to the new N_S :

$$N_S = \frac{c}{\gamma H \tan \phi} \quad (5.29)$$

This new formulation allows Michalowski to write the new charts (fig. 5.13). For each value of the slope inclination β there is a curve (this means that β is taken as a parameter) The chart coordinates are the N_S in x-axis and the new parameter $\frac{F}{\tan \phi}$ in y-axis: so $y \equiv y(N_S)$ is a function of the new N_S and this implies that $F \equiv F(N_S)$.

We notice that, just because of the way the number N_S is defined, the charts cannot be applied to soils with $\phi = 0$, because N_S becomes singular.

Geometrical and geotechnical parameters	Range
Cohesion	0 - 35 KPa
Friction angle	$0^{\circ} - 30^{\circ}$
Unit weight	$15 - 25 \text{KN}/\text{m}^3$
Height	$3 - 200\text{m}$

TABLE 5.1: Ranges of the geotechnical and geometrical parameters used to study Michalowski's stability charts

Also for Mikalowski's charts, the amount of computing time that should be spent for a complete reconstruction of these charts is not in our favor and we were obliged to choose, as we did for Taylor's charts, some cases. The ranges of the parameters explored in our analysis are listed in the Tab. 5.1.

5.2.1 Numerical results

For the first phase of the analysis we have considered four values of the slope inclination, namely $\beta = 10^{\circ}, 30^{\circ}, 45^{\circ}, 60^{\circ}$, which means that we have considered four Michalowski's curves and we have varied the parameters within the ranges of Tab. 5.1 by taking into account a large number of configurations (more than in Taylor's charts analysis).

Figs. 5.14, 5.15, 5.16 show the results we obtained by applying the *MLD* method. The calculated points that should lie on the curves fall indeed in somewhat different positions and the discrepancy (measured in terms of the stability number F) ranges from 5% to about 20%.

From this first analysis it appears that Micalowki's charts can be interpreted as Taylor's charts. The Mikalowski's independent variable $\frac{F}{\tan \phi}$ has not a univocal dependence on the stability number N_s , and more accurately computed values result to be close to the theoretical curves but displaced and forming a cloud around the curves.

To understand better, as for the stability charts of Taylor, we have selected one curve, $\beta = 30^{\circ}$, and we have considered the same cases used in Taylor's curves analysis. The result is that the resulting points (that by purpose have the same stability number and

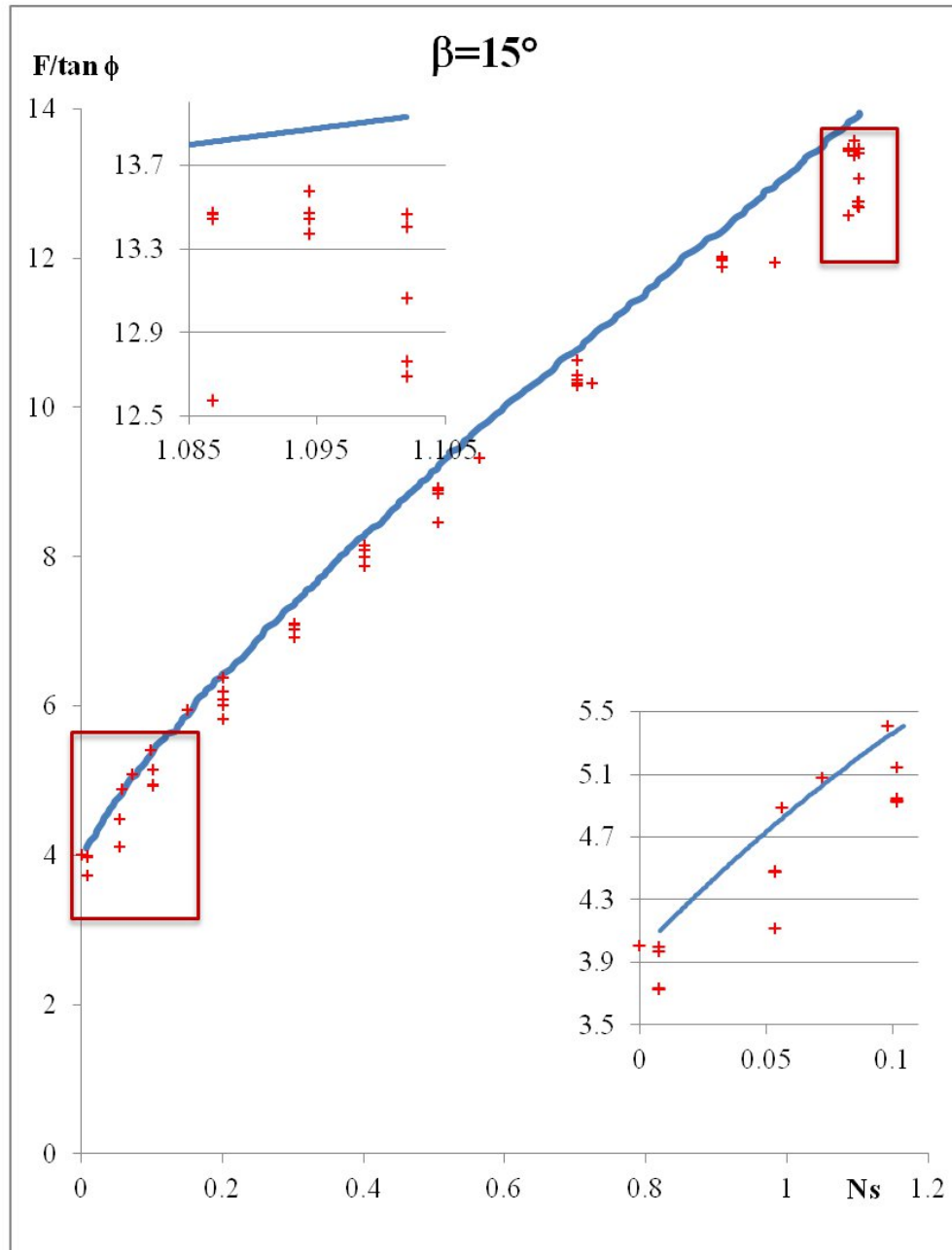


FIGURE 5.14: Mikalowski's curve of $\beta = 15^\circ$ compared with our results (red crosses). Discrepancies range from 5% to 15%.

therefore the same abscissa, are not located along the Michalowski curve, but under it fig. 5.18.

For a further analysis, we have considered four points of the Michalowski curve corresponding to different values of the abscissa. For each point we have considered two cases, corresponding to critical values of the safety factor, i.e. with $F \approx 1$. These cases differ only for the unit weight ($15 - 25 \text{KN}/\text{m}^3$) that was seen to have a very relevant

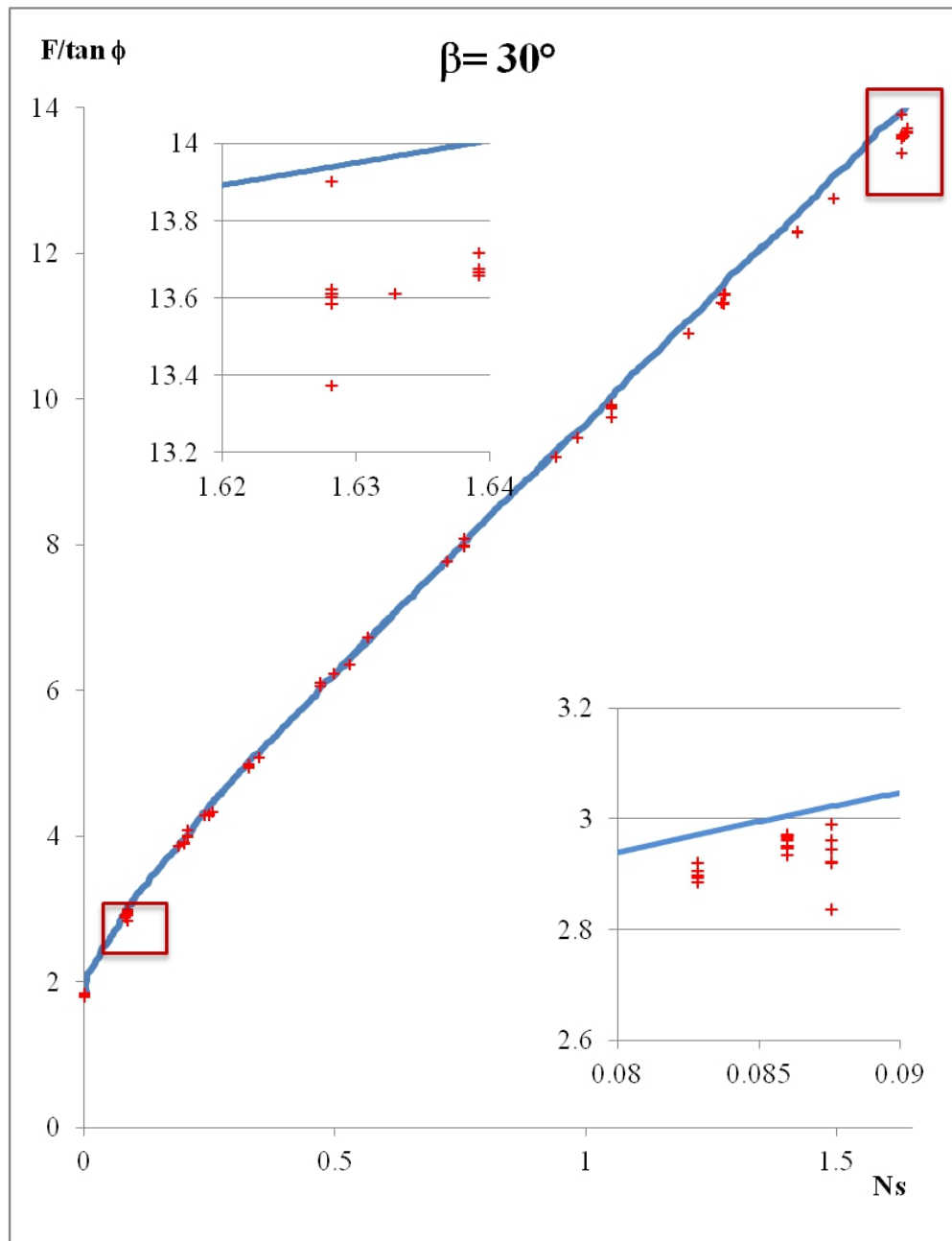


FIGURE 5.15: Mikalowski's curve of $\beta = 30^\circ$. The same as for Fig. 5.14

role in the previous section, while all other parameters are kept constant (i.e. friction angle $\phi = 15^\circ$ and slope geometry).

The results illustrated in fig. 5.19 show that if one varies only the unit weight, the points seem to be aligned along a curve (dashed red line for $\gamma = 25 \text{ KN/m}^3$ and green line for $\gamma = 15 \text{ KN/m}^3$), but in none of the two cases this curve identifies with the one by Michalowski, with the largest discrepancies being due to the lower unit weight. Though

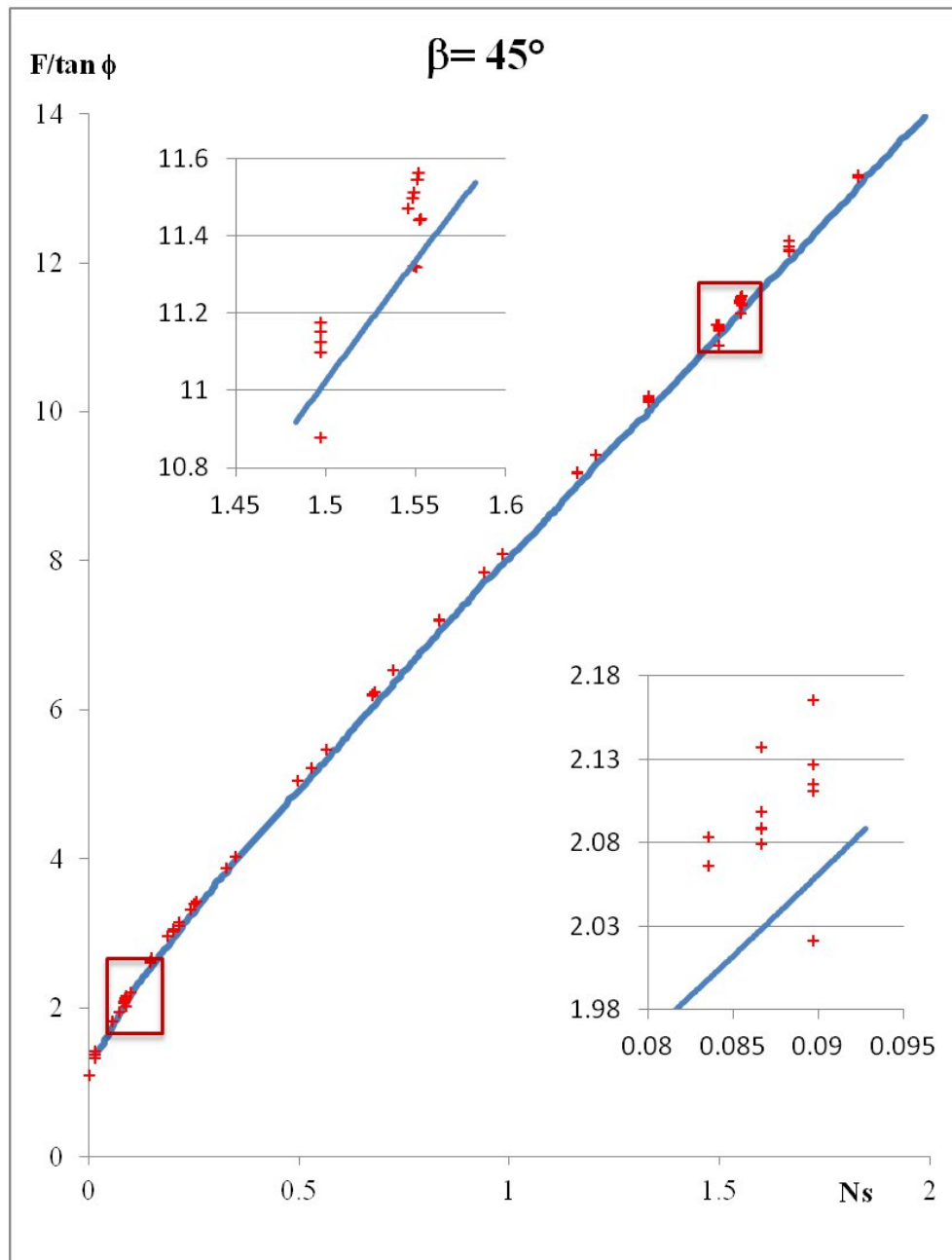


FIGURE 5.16: Mikalowski's curve of $\beta = 45^\circ$. Discrepancies range from 5% to 10%.

we have not conducted a systematic analysis, the results we obtained are suggestive that Mikalowski's chart tend to produce overestimations of the safety factor.

In conclusion, even Mikalowski's stability charts seem to be a too simplistic tool, and do not provide the right information about the soil conditions. A further observation is that, when soil is close to instability, even errors in the range of 10% – 15% cannot be considered tolerable, since one might evaluate as stable a slope that indeed is unstable.

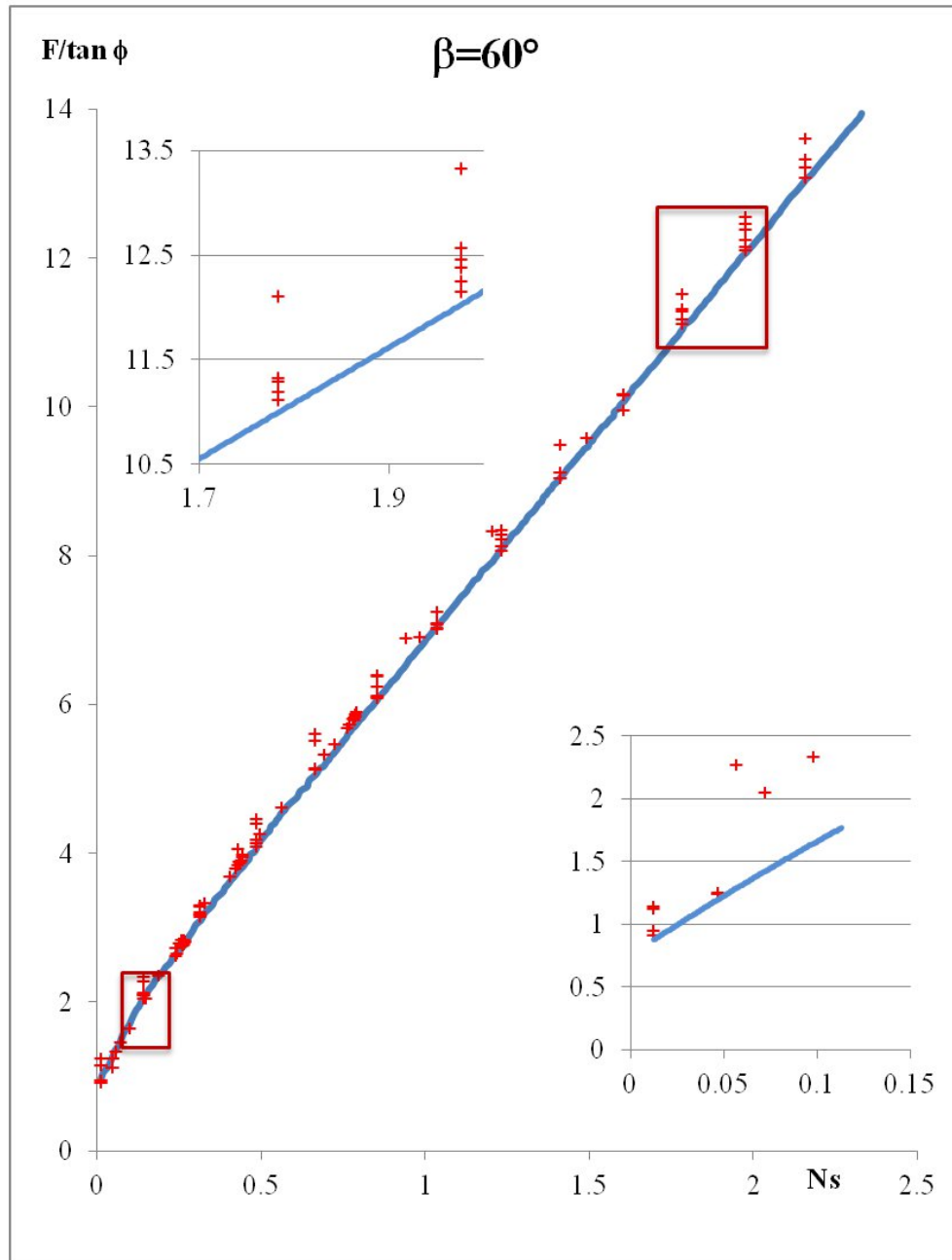


FIGURE 5.17: Mikalowski's curve of $\beta = 60^\circ$. Discrepancies range from 5% to 20%.

In addition to the traditional stability charts referred to homogeneous slopes, Michalowski introduced new charts where he took into account also the effect of pore pressure and seismic load. Here, we have focused only on the latter and in particular we analyzed the case for $\beta = 60^\circ$ with the horizontal seismic coefficient $k_h \equiv [0.1; 0.2; 0.3]$.

Results are displayed in Fig. 5.20 and show that introducing new factors, like the seismic load, leads to larger discrepancies (up to 35%) with respect to the *MLD* results,

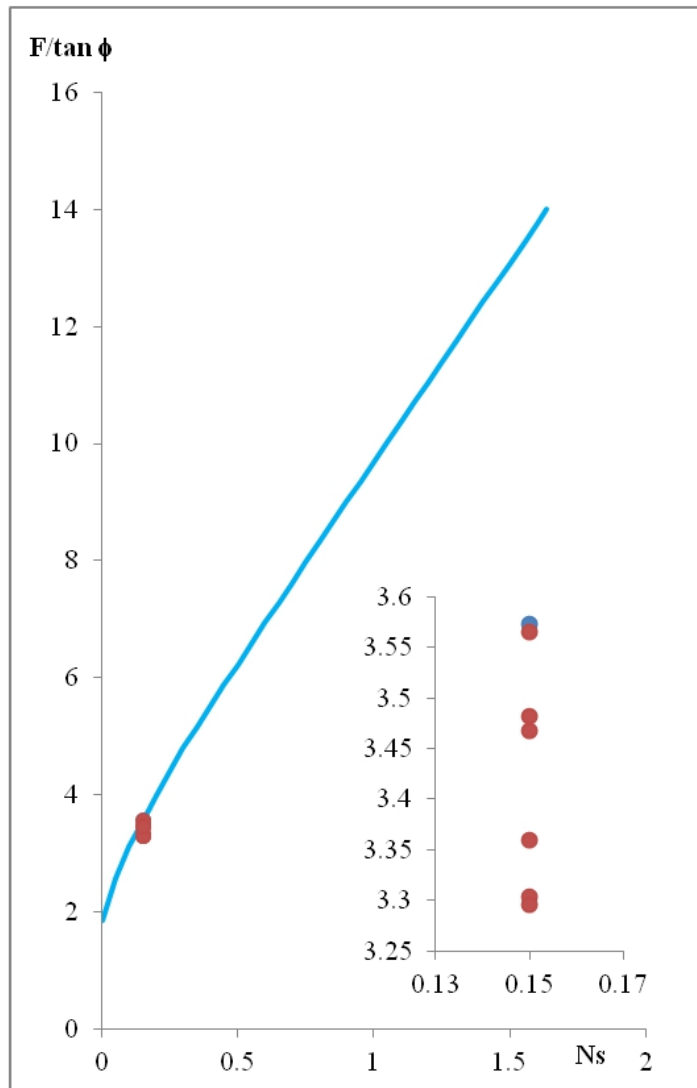


FIGURE 5.18: Chart of $\beta = 30^\circ$. Six different cases (red points) that should all correspond to the same point (blue dot) in Mikalowski's diagram. Discrepancies range from 2% to about 10%.

which makes the Michalowski's stability charts less reliable. In this case it seems that Mikalowski's curves tend to underestimate the value of the safety factor.

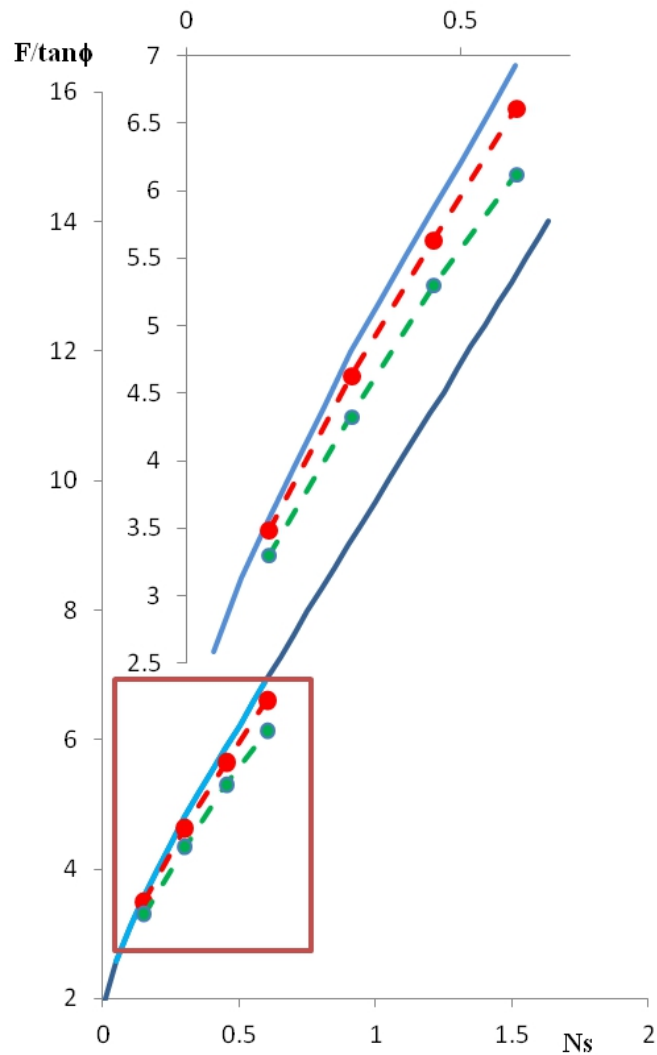


FIGURE 5.19: Chart of $\beta = 30^\circ$. We have selected 4 points and for each one we have defined 2 cases, varying the weight $\gamma = [15 \text{ (green points)} - 25 \text{ (red points)}] \text{KN}/\text{m}^3$. It seems that for a given value of the weight, the points are located along their own curve, that however is not the Michalowski curve. Discrepancies range from 5% to 15%.

5.3 Conclusion

In light of what is shown in this chapter, stability charts, which today are a tool extensively used in the engineering field, have to be used with caution, because they do not provide a correct information on the stability of a slope, but only a rough approximate

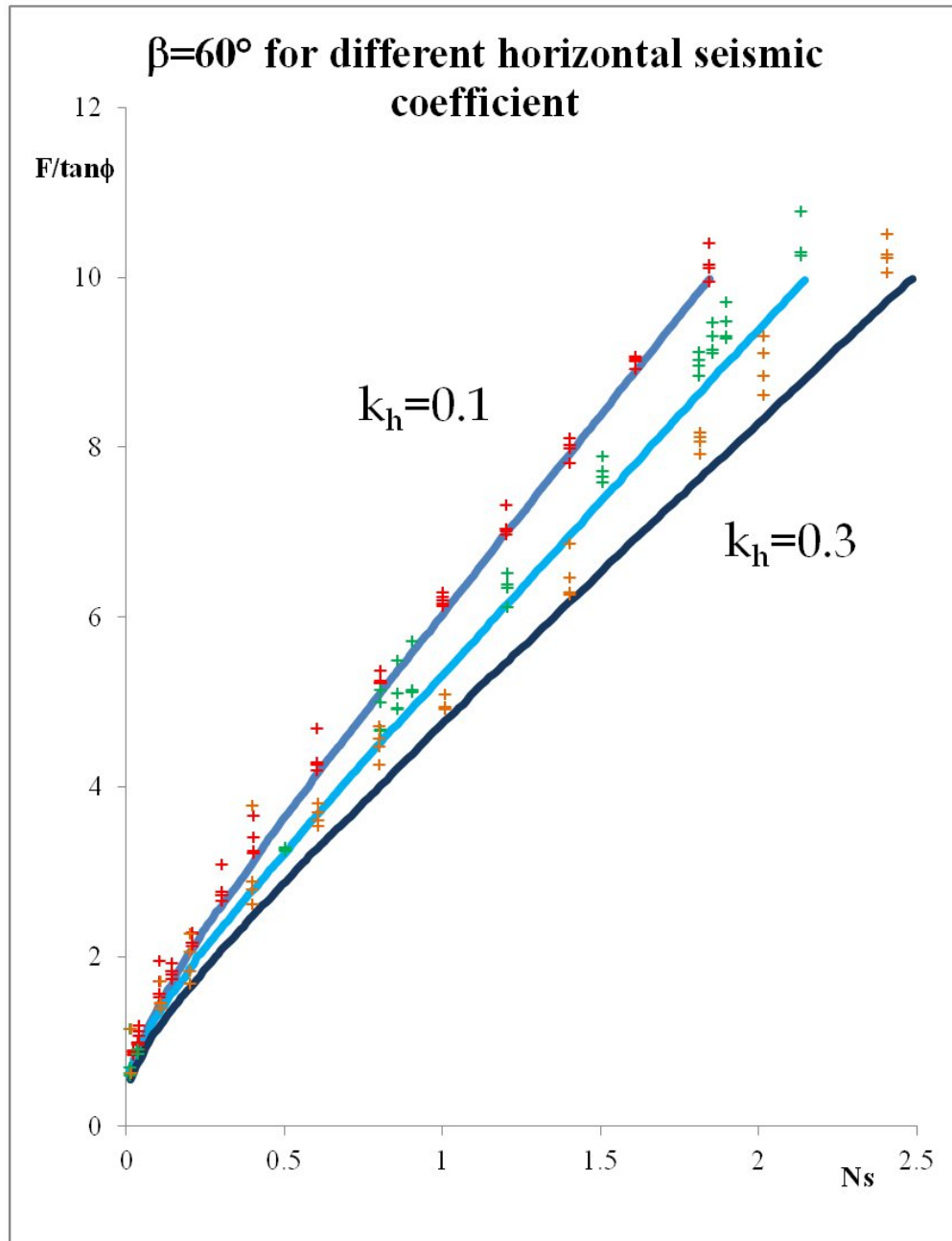


FIGURE 5.20: Chart of $\beta = 60^\circ$ with horizontal seismic load. Discrepancies range from 5% to 35%.

estimate. We have further shown that the unit weight of the slope is one of the parameters that most influence the value of the safety factor, more than the height of the slope. Stability charts cannot be considered a good instrument to solve the problem of the limit equilibrium, but they have to be integrated with, or better replaced by, more complex and complete instruments, like the *MLD* method.

Appendix A

A.1 The equilibrium equations

For a bi-dimensional body divided in slices, the equilibrium equations are derived from the local equilibrium of the stress matrix

$$\partial_x \sigma_{xx} + \partial_z \sigma_{xz} = -k_h \rho g \quad (\text{A.1})$$

$$\partial_x \sigma_{zx} + \partial_z \sigma_{zz} = (1 + k_v) \rho g \quad (\text{A.2})$$

where

$$\sigma_{zx} = \sigma_{xz} \quad (\text{A.3})$$

If the equations (A.1) and (A.2) are integrated over a surface Σ with a close boundary C , we obtain

$$\int_{\Sigma} (\partial_x \sigma_{xx} + \partial_z \sigma_{xz}) dx dz = - \int_{\Sigma} k_h \rho g dx dz = -k_h \rho g A \quad (\text{A.4})$$

$$\int_{\Sigma} (\partial_x \sigma_{zx} + \partial_z \sigma_{zz}) dx dz = \int_{\Sigma} (1 + k_v) \rho g dx dz = (1 + k_v) \rho g A \quad (\text{A.5})$$

where A is the area of the surface Σ . The density and the seismic coefficient are assumed to be constant over the surface.

A.1.1 The horizontal equilibrium equation

We derive the horizontal equation from A.4, that is the divergence of the vector $[\sigma_{xx}, \sigma_{xz}]$. Introducing the position

$$a_1 = \sigma_{xx}$$

$$a_2 = \sigma_{xz}$$

and remembering the Gauss theorem in which the surface integral is linked to the boundary integral with the expression

$$\int_{\Sigma} \partial_i a_i d\sigma = \oint_C a_i n_i dl \quad (\text{A.6})$$

we have

$$\oint_C (\sigma_{xx} n_x + \sigma_{xz} n_z) dl = -k_h \rho g A \quad (\text{A.7})$$

where \mathbf{n} is the outward pointing unit normal vector of the boundary C . The integral has no orientation and the element dl is always positive. The traction on the element dl orthogonal to the vector \mathbf{n} is

$$\mathbf{T}(\mathbf{n}) = (\sigma_{xx} n_x + \sigma_{xz} n_z) \mathbf{i} + (\sigma_{zx} n_x + \sigma_{zz} n_z) \mathbf{k} \quad (\text{A.8})$$

and its components n_x and n_z are

$$T_x(\mathbf{n}) = \sigma_{xx} n_x + \sigma_{xz} n_z \quad (\text{A.9a})$$

$$T_z(\mathbf{n}) = \sigma_{zx}n_x + \sigma_{zz}n_z \quad (\text{A.9b})$$

Considering one slice with infinitesimal area dA

$$dA = (z_2 - z_1)dx \quad (\text{A.10})$$

we can analyze the four sides of the slide separately, to write the line integral as the sum of the four contributions.

- Side 1: $\mathbf{n}_1 = (1, 0)$ $\mathbf{T}(\mathbf{n})i = \sigma_{xx}$

$$\int_{z_1(x+\frac{dx}{2})}^{z_2(x+\frac{dx}{2})} \sigma_{xx} dz = E \left(x + \frac{dx}{2} \right) \quad (\text{A.11})$$

where we used the expression (2.1). In the same way

- Side 3: $\mathbf{n}_3 = (-1, 0)$ $\mathbf{T}(\mathbf{n})i = -\sigma_{xx}$

$$\int_{z_1(x-\frac{dx}{2})}^{z_2(x-\frac{dx}{2})} -\sigma_{xx} dz = -E \left(x - \frac{dx}{2} \right) \quad (\text{A.12})$$

- Side 2: $\mathbf{n}_2 = (\sin \beta, \cos \beta)$

$$\int_{x-\frac{dx}{2}}^{x+\frac{dx}{2}} (\sigma_{xx}(x, z_2(x)) \sin \beta + \sigma_{xz}(x, z_2(x)) \cos \beta) dl = \sigma_{xx}(x, z_2(x)) \tan \beta + \sigma_{xz}(x, z_2(x)) \quad (\text{A.13})$$

with $dl = \frac{dx}{\cos \beta}$, and

- Side 4: $\mathbf{n}_4 = (-\sin \alpha, -\cos \alpha)$

$$\int_{x-\frac{dx}{2}}^{x+\frac{dx}{2}} (-\sigma_{xx}(x, z_1(x)) \sin \alpha + \sigma_{xz}(x, z_1(x)) \cos \alpha) dl = \sigma_{xx}(x, z_1(x)) \tan \alpha + \sigma_{xz}(x, z_1(x)) \quad (\text{A.14})$$

$$\text{with } dl = \frac{dx}{\cos \alpha}$$

All of the contributions compose the horizontal equilibrium equation, as

$$E \left(x + \frac{dx}{2} \right) - E \left(x - \frac{dx}{2} \right) + [\sigma_{xx}(x, z_2(x)) \tan \beta + \sigma_{xz}(x, z_2(x))] dx + [\sigma_{xx}(x, z_1(x)) \tan \alpha + \sigma_{xz}(x, z_1(x))] dx \quad (\text{A.15})$$

The stresses along the basis of the slice are the pressure P and the shear stress S , defined as

$$\mathbf{P} = -\mathbf{T}(\mathbf{n}_4) \cdot \mathbf{n}_4 \quad (\text{A.16a})$$

$$\mathbf{S} = \mathbf{T}(\mathbf{n}_4) \cdot \mathbf{t}_4 \quad (\text{A.16b})$$

where the normal \mathbf{n}_4 and tangential \mathbf{t}_4 unit vector are

$$\mathbf{n}_4 = (-\sin \alpha, -\cos \alpha) \quad (\text{A.17a})$$

$$\mathbf{t}_4 = (-\cos \alpha, \sin \alpha) \quad (\text{A.17b})$$

We can express the stress components of the equation (A.15) in terms of \mathbf{P} and \mathbf{S} . Since the couples of the unit vectors (\mathbf{i}, \mathbf{k}) and $(\mathbf{t}_4, \mathbf{n}_4)$ are orthonormal bases in (x, z) , the vector $\mathbf{T}(\mathbf{n}_4)$ can be expressed as:

$$\mathbf{T}(\mathbf{n}_4) = S\mathbf{t}_4 - P\mathbf{n}_4 = T_x(\mathbf{n}_4)\mathbf{i} + T_z(\mathbf{n}_4)\mathbf{k} \quad (\text{A.18})$$

After a scalar multiplication of (A.18) by \mathbf{i} , we have

$$T_x(\mathbf{n}_4) = St_{4x} - Pn_{4x} = -S \cos \alpha + P \sin \alpha \quad (\text{A.19})$$

and by \mathbf{k}

$$T_z(\mathbf{n}_4) = St_{4z} - Pn_{4z} = S \sin \alpha + P \cos \alpha \quad (\text{A.20})$$

Considering the expression (A.19) and (A.9), we can re-elaborate the expression (A.14) and write

$$-\sigma_{xx}(x, z_1) \sin \alpha - \sigma_{xz}(x, z_1) \cos \alpha = -S \cos \alpha + P \sin \alpha \quad (\text{A.21})$$

and, after dividing by $\cos \alpha$, we obtain

$$-\sigma_{xx}(x, z_1) \tan \alpha - \sigma_{xz}(x, z_1) = -S + P \tan \alpha \quad (\text{A.22})$$

We can follow the same mathematical steps for the side 2, introducing the hydrostatic pressure above the surface z_2 . We obtain

$$\mathbf{T}(\mathbf{n}_2) = T_x \mathbf{i} + T_z \mathbf{k} = -D \mathbf{n}_2 \quad (\text{A.23})$$

where

$$\mathbf{n}_2 = (\sin \beta, \cos \beta) \quad (\text{A.24})$$

and the components are

$$T_x(\mathbf{n}_2) = -D \mathbf{n}_2 \cdot \mathbf{i} = -D \sin \beta \quad (\text{A.25})$$

$$T_z(\mathbf{n}_2) = -D \mathbf{n}_2 \cdot \mathbf{k} = -D \cos \beta \quad (\text{A.26})$$

Finally the horizontal equilibrium equation becomes

$$E \left(x + \frac{dx}{2} \right) - E \left(x - \frac{dx}{2} \right) + (P \tan \alpha - S - D \tan \beta) dx + k_h w dx = 0 \quad (\text{A.27})$$

that in differential form can be written

$$\frac{dE}{dx} - S + P \tan \alpha - D \tan \beta + k_h w = 0 \quad (\text{A.28})$$

This is exactly the equation (2.6).

A.1.2 The vertical equilibrium equation

Also in this case, the line integral is the sum of the four contributions of the each side of the slice

- Side 1: $\mathbf{n}_1 = (1, 0)$ $\mathbf{T}(\mathbf{n}) \cdot \mathbf{k} = \sigma_{zx}$

$$\int_{z_1(x+\frac{dx}{2})}^{z_2(x+\frac{dx}{2})} \sigma_{zx} dz = X \left(x + \frac{dx}{2} \right) \quad (\text{A.29})$$

where we used the equation (2.2).

- Side 3: $\mathbf{n}_3 = (-1, 0)$ $\mathbf{T}(\mathbf{n}) \cdot \mathbf{k} = -\sigma_{zx}$

$$\int_{z_1(x-\frac{dx}{2})}^{z_2(x-\frac{dx}{2})} -\sigma_{zx} dz = -X \left(x - \frac{dx}{2} \right) \quad (\text{A.30})$$

- Side 2: $\mathbf{n}_2 = (\sin \beta, \cos \beta)$ $\mathbf{T}(\mathbf{n}_2) \cdot \mathbf{k} = \sigma_{zx} \sin \beta + \sigma_{zz} \cos \beta$

$$\int_{x-\frac{dx}{2}}^{x+\frac{dx}{2}} (\sigma_{zx}(x, z_2(x)) \sin \beta + \sigma_{zz}(x, z_2(x)) \cos \beta) dl_2 = \sigma_{zx}(x, z_2(x)) \tan \beta + \sigma_{zz}(x, z_2(x)) \quad (\text{A.31})$$

with $dl_2 = \frac{dx}{\cos \beta}$, and

- Side 4: $\mathbf{n}_4 = (-\sin \alpha, -\cos \alpha)$ $\mathbf{T}(\mathbf{n}_4) \cdot \mathbf{k} = -\sigma_{zx} \sin \alpha + \sigma_{zz} \cos \alpha$

$$\int_{x-\frac{dx}{2}}^{x+\frac{dx}{2}} (-\sigma_{zx}(x, z_1(x)) \sin \alpha - \sigma_{zz}(x, z_1(x)) \cos \alpha) dl_4 = (-\sigma_{zx}(x, z_1(x)) \tan \alpha - \sigma_{zz}(x, z_1(x))) \quad (\text{A.32})$$

with $dl_4 = \frac{dx}{\cos \alpha}$.

All of the four contributions summed together lead to:

$$\begin{aligned} X \left(x + \frac{dx}{2} \right) - X \left(x - \frac{dx}{2} \right) + (\sigma_{zx}(x, z_2(x)) \tan \beta + \sigma_{zz}(x, z_2(x))) dx + \\ + (-\sigma_{zx}(x, z_1(x)) \tan \alpha - \sigma_{zz}(x, z_1(x))) dx - (1 + k_v) \rho g (z_2 - z_1) dx = 0 \end{aligned} \quad (\text{A.33})$$

By taking into account S and P given in (A.20) and D given in (A.26), we obtain the vertical equilibrium equation

$$X \left(x + \frac{dx}{2} \right) - X \left(x - \frac{dx}{2} \right) + T_z \frac{dx}{\cos \alpha} - D dx - (1 + k_v) w dx = 0 \quad (\text{A.34})$$

that in differential form becomes

$$\frac{dX}{dx} + P + S \tan \alpha - D - (1 + k_v) w = 0 \quad (\text{A.35})$$

This is exactly the equation (2.7).

A.2 The moment equation

The system is in static equilibrium if the sum of all the forces is zero

$$\sum_k \mathbf{F}_k = 0 \quad (\text{A.36})$$

and the total moment with respect to a given point O is also zero, that is

$$\mathbf{M} = \sum_k [\mathbf{r}_k \times \mathbf{F}_k] = 0 \quad (\text{A.37})$$

where \mathbf{r}_k is the vector that joins the point O to the application point of the force F_k . But for a system in equilibrium the moment is independent from the reference system and we can define it with respect to any point O' that is displaced by a distance R from the point O . We indicate \mathbf{r}'_k the vector that joins O' with the application point of the k th force, and we obtain

$$\mathbf{r}'_k = \mathbf{r}_k + R \quad (\text{A.38})$$

and

$$\mathbf{M}' = \sum_k [\mathbf{r}'_k \times \mathbf{F}_k] = \sum_k [\mathbf{r}_k \times \mathbf{F}_k] + \sum_k [R \times \mathbf{F}_k] = \mathbf{M} + R \times \sum_k \mathbf{F}_k \quad (\text{A.39})$$

From (A.36), we have that

$$\mathbf{M}' = \mathbf{M} \quad (\text{A.40})$$

So we can choose any point, and in our analysis we impose that the point O coincides with the middle point of the slice base $M(x, z_M)$. As we have done for the analysis of the equilibrium equations for the forces, we take into account separately the contributions of the moment for slice sides and for each one we define the following vectors

$$\mathbf{r}_1(z) = [z - z_1(x)]\mathbf{k} + \frac{dx}{2}\mathbf{i} \quad \text{con} \quad z_1\left(x + \frac{dx}{2}\right) \leq z \leq z_2\left(x + \frac{dx}{2}\right) \quad (\text{A.41})$$

$$\mathbf{r}_2(x_i) = [z_2(x_i) - z_1(x)]\mathbf{k} + (x_i - x)\mathbf{i} \quad \text{con} \quad x - \frac{dx}{2} \leq x_i \leq x + \frac{dx}{2} \quad (\text{A.42})$$

$$\mathbf{r}_3(z) = [z - z_1(x)]\mathbf{k} - \frac{dx}{2}\mathbf{i} \quad \text{con} \quad z_1\left(x - \frac{dx}{2}\right) \leq z \leq z_2\left(x - \frac{dx}{2}\right) \quad (\text{A.43})$$

$$\mathbf{r}_4(x_i) = [z_1(x_i) - z_1(x)]\mathbf{k} + (x_i - x)\mathbf{i} \quad \text{con} \quad x - \frac{dx}{2} \leq x_i \leq x + \frac{dx}{2} \quad (\text{A.44})$$

In order to take into account the moment of the volume forces that act on the center of mass of the slide, let us also introduce the vector

$$\mathbf{r}_B = (z_B - z_1(x))\mathbf{k} \quad (\text{A.45})$$

where the index B indicates the barycenter. Using the stress matrix components, for each side we have

- Side 1: considering (A.41) with (A.11) and (A.29),

$$\begin{aligned}
\mathbf{M}_1 &= \int_{z_1(x+\frac{dx}{2})}^{z_2(x+\frac{dx}{2})} \frac{d\mathbf{M}_1}{dz} dz = \int_{z_1(x+\frac{dx}{2})}^{z_2(x+\frac{dx}{2})} \left(\mathbf{r}_1 \times \frac{\mathbf{f}_1}{dz} \right) dz = \\
&= \int_{z_1(x+\frac{dx}{2})}^{z_2(x+\frac{dx}{2})} \left\{ \left\{ [z - z_1(x)]\mathbf{k} + \frac{dx}{2}\mathbf{i} \right\} \times [\sigma_{xx}\mathbf{i} + \sigma_{zx}\mathbf{k}] \right\} dz = \quad (\text{A.46}) \\
&= \int_{z_1(x+\frac{dx}{2})}^{z_2(x+\frac{dx}{2})} \left\{ [z - z_1(x)]\sigma_{xx}\mathbf{j} + \frac{dx}{2}\sigma_{zx}(-\mathbf{j}) \right\} dz
\end{aligned}$$

- Side 2: considering (A.42) with (A.13) and (A.31) and remembering (A.23),

$$\begin{aligned}
\mathbf{M}_2 &= \int_{x-\frac{dx}{2}}^{x+\frac{dx}{2}} \left\{ \left\{ [z_2(x') - z_1(x)]\mathbf{k} + (x' - x)\mathbf{i} \right\} \times [(-D \tan \beta)\mathbf{i} + (-D)\mathbf{k}] \right\} dx' = \\
&= \int_{x-\frac{dx}{2}}^{x+\frac{dx}{2}} \left\{ [z_2(x') - z_1(x)](-D \tan \beta)\mathbf{j} + (x' - x)(-D)(-\mathbf{j}) \right\} dx' \\
&\quad (\text{A.47})
\end{aligned}$$

- Side 3: using (A.12) and (A.30)

$$\begin{aligned}
\mathbf{M}_3 &= \int_{z_1(x-\frac{dx}{2})}^{z_2(x-\frac{dx}{2})} \frac{d\mathbf{M}_3}{dz} dz = \int_{z_1(x-\frac{dx}{2})}^{z_2(x-\frac{dx}{2})} \left(\mathbf{r}_3 \times \frac{\mathbf{f}_3}{dz} \right) dz = \\
&= \int_{z_1(x-\frac{dx}{2})}^{z_2(x-\frac{dx}{2})} \left\{ \left\{ [z - z_1(x)]\mathbf{k} - \frac{dx}{2}\mathbf{i} \right\} \times [-\sigma_{xx}\mathbf{i} - \sigma_{zx}\mathbf{k}] \right\} dz = \quad (\text{A.48}) \\
&= \int_{z_1(x-\frac{dx}{2})}^{z_2(x-\frac{dx}{2})} \left\{ [z - z_1(x)](-\sigma_{xx})\mathbf{j} + \left(-\frac{dx}{2}\right)(-\sigma_{zx})(-\mathbf{j}) \right\} dz
\end{aligned}$$

- Side 4: with the expressions (A.14), (A.32) and (A.18)

$$\begin{aligned}
\mathbf{M}_4 &= \int_{x-\frac{dx}{2}}^{x+\frac{dx}{2}} \left\{ \left[z_1(x') - z_1(x) \right] \mathbf{k} + (x' - x) \mathbf{i} \right\} \times \left[(P \tan \alpha - S) \mathbf{i} + (S \tan \alpha + P) \mathbf{k} \right] dx' = \\
&= \int_{x-\frac{dx}{2}}^{x+\frac{dx}{2}} \left\{ \left[z_1(x') - z_1(x) \right] (P \tan \beta - S) \mathbf{j} + (x' - x) (S \tan \alpha + P) (-\mathbf{j}) \right\} dx'
\end{aligned} \tag{A.49}$$

Summing all of the contributions we obtain the moment of the forces acting along the slice boundary. The volume forces, as weight and seismic load, act on the center of mass (x_B, z_B) , and the corresponding moment is

$$\mathbf{M}_B = (z_B(x) - z_1(x)) \mathbf{k} \times [k_h \rho g (z_2(x) - z_1(x)) dx \mathbf{i} - k_v \rho g (z_2(x) - z_1(x)) dx \mathbf{k}] \tag{A.50}$$

Simplifying

$$\int_{z_1(x+\frac{dx}{2})}^{z_2(x+\frac{dx}{2})} [z - z_1(x)] \sigma_{xx} \mathbf{j} dx = \int_{z_1(x+\frac{dx}{2})}^{z_2(x+\frac{dx}{2})} z \sigma_{xx} \mathbf{j} dx - z_1(x) \int_{z_1(x+\frac{dx}{2})}^{z_2(x+\frac{dx}{2})} \sigma_{xx} \mathbf{j} dx \tag{A.51}$$

and defining the first-order moment of the normal stresses as

$$\mathbf{A}(x) = \left[\int_{z_1(x)}^{z_2(x)} z \sigma_{xx} dz \right] (\mathbf{j}) \tag{A.52}$$

the total moment is

$$\begin{aligned}
\mathbf{M} = & \left[A \left(x + \frac{dx}{2} \right) - z_1(x) E \left(x + \frac{dx}{2} \right) - \frac{dx}{2} X \left(x + \frac{dx}{2} \right) + \right. \\
& - A \left(x - \frac{dx}{2} \right) + z_1(x) E \left(x - \frac{dx}{2} \right) - \frac{dx}{2} X \left(x - \frac{dx}{2} \right) + \\
& + \int_{x - \frac{dx}{2}}^{x + \frac{dx}{2}} \{ [z_2(x') - z_1(x)] (-D \tan \beta) + (x' - x) D \} dx' + \\
& + \int_{x - \frac{dx}{2}}^{x + \frac{dx}{2}} \{ [z_1(x') - z_1(x)] (P \tan \beta - S) + (x' - x) (-S \tan \alpha - P) \} dx' + \\
& \left. + k_h \rho g (z_B(x) - z_1(x)) (z_2(x) - z_1(x)) dx \right] \mathbf{j} = 0
\end{aligned} \tag{A.53}$$

and has to be equal to zero.

Since we can write:

$$\frac{dA}{dx} = \frac{A \left(x + \frac{dx}{2} \right) - A \left(x - \frac{dx}{2} \right)}{dx} \tag{A.54}$$

$$-z_1(x) \frac{dE}{dx} = -z_1(x) \frac{E \left(x + \frac{dx}{2} \right) - E \left(x - \frac{dx}{2} \right)}{dx} \tag{A.55}$$

thus the moment equilibrium equation can be given the form:

$$\frac{dA}{dx} - z_1(x) \frac{dE}{dx} - \frac{1}{2} \left[X \left(x + \frac{dx}{2} \right) + X \left(x - \frac{dx}{2} \right) \right] - D \tan \beta (z_2 - z_1) + k_h w (z_B - z_1) = 0 \tag{A.56}$$

that finally becomes

$$\frac{dA}{dx} - z_1(x) \frac{dE}{dx} - X - (z_2 - z_1) D \tan \beta - k_h w (z_B - z_1) = 0 \tag{A.57}$$

identical to the 2.8

Appendix B

In this section we show some mathematical developments for the methods of Fellenius and Bishop.

B.1 The Ordinary method

The system of equations is composed of:

$$\begin{cases} P \tan \alpha - S - D \tan \beta = -k_h w \\ P + S \tan \alpha - D = (1 + k_v) w \end{cases} \quad (\text{B.1})$$

$$\begin{cases} S = P \tan \alpha - D \tan \beta + k_h w \\ P + [P \tan \alpha - D \tan \beta + k_h w] \tan \alpha - D = (1 + k_v) w \end{cases} \quad (\text{B.2})$$

$$\begin{cases} S = P \tan \alpha - D \tan \beta + k_h w \\ P(1 + \tan^2 \alpha) = [D \tan \beta - k_h w] \tan \alpha + D + (1 + k_v) w \end{cases} \quad (\text{B.3})$$

$$\begin{cases} S = P \tan \alpha - D \tan \beta + k_h w \\ P = \frac{[D \tan \beta - w k_h] \tan \alpha + D + (1 + k_v) w}{(1 + \tan^2 \alpha)} \end{cases} \quad (\text{B.4})$$

Knowing that

$$\frac{1}{(1 + \tan^2 \alpha)} = \cos^2 \alpha$$

we have

$$\begin{cases} S = P \tan \alpha - D \tan \beta + k_h w \\ P = [D \tan \beta \tan \alpha - k_h w \tan \alpha + D + (1 + k_v)w] \cos^2 \alpha \end{cases} \quad (\text{B.5})$$

$$\begin{cases} S = [D \tan \beta \sin \alpha \cos \alpha - k_h w \sin \alpha \cos \alpha + [D + (1 + k_v)w] \cos^2 \alpha] \tan \alpha - D \tan \beta + w k_h \\ P = D \tan \beta \sin \alpha \cos \alpha - k_h w \sin \alpha \cos \alpha + [D + (1 + k_v)w] \cos^2 \alpha \end{cases} \quad (\text{B.6})$$

$$\begin{cases} S = D \tan \beta \sin^2 \alpha - k_h w \sin^2 \alpha + [D + (1 + k_v)w] \cos \alpha \sin \alpha - D \tan \beta + w k_h \\ P = D \tan \beta \sin \alpha \cos \alpha - k_h w \sin \alpha \cos \alpha + [D + (1 + k_v)w] \cos^2 \alpha \end{cases} \quad (\text{B.7})$$

and with

$$\sin^2 \alpha = 1 - \cos^2 \alpha$$

we obtain

$$\begin{cases} S = -D \tan \beta \cos^2 \alpha + k_h w \cos^2 \alpha + [D + (1 + k_v)w] \cos \alpha \sin \alpha \\ P = D \tan \beta \sin \alpha \cos \alpha - k_h w \sin \alpha \cos \alpha + [D + (1 + k_v)w] \cos^2 \alpha \end{cases} \quad (\text{B.8})$$

Putting the expressions of P and S in the Mohr-Coulomb relationship, we find

$$F = \frac{c^* + [D \tan \beta \sin \alpha \cos \alpha - k_h w \sin \alpha \cos \alpha + [D + (1 + k_v)w] \cos^2 \alpha] \tan \phi}{[D + (1 + k_v)w \cos \alpha \sin \alpha - D \tan \beta \cos^2 \alpha + k_h w \cos^2 \alpha]} \quad (\text{B.9})$$

The expression (B.9) depends on the geotechnical parameters (c , u , ϕ , ρ), on the geometry (z_1 , z_2 , α , β), and on the external loads (D , k_h , k_v). Dividing by $\cos \alpha$ and integrating the numerator and denominator, we obtain exactly the expression (2.19).

B.2 The Bishop's method

With our notation, using the expression of the moment and the Mohr-Coulomb criterion, the equation of Bishop can be expressed as

$$\int_{x_i}^{x_f} \{(-D \tan \beta + k_h w) \cos \alpha + [D + (1 + k_v)w] \sin \alpha\} dx + \frac{1}{R} \int_{x_i}^{x_f} [D \tan \beta (z_2 - z_1) - k_h w (z_B - z_1)] dx = \int_{x_i}^{x_f} \frac{1}{F \cos \alpha} \left\{ c + (P - u) \tan \phi \right\} dx \quad (\text{B.10})$$

and P can be obtained from the vertical equilibrium equations of the forces

$$P = \frac{D - \frac{dX}{dx} + (k_v + 1)w - \frac{c^*}{F} \tan \alpha}{\left(1 + \frac{\tan \phi \tan \alpha}{F}\right)} \quad (\text{B.11})$$

Inserting the equation (B.11) in (B.10), we have

$$\begin{aligned}
& \int_{x_i}^{x_f} \left[\left(-D \tan \beta + k_h w \right) \cos \alpha + \left(D + (1 + k_v) w \right) \sin \alpha \right] dx + \\
& \frac{1}{R} \int_{x_i}^{x_f} [D \tan \beta (z_2 - z_1) - k_h w (z_B - z_1)] dx = \\
& = \int_{x_i}^{x_f} \frac{1}{F \cos \alpha} \left\{ c^* + \left(\frac{D - \frac{dX}{dx} + (1 + k_v) w - \frac{c^*}{F} \tan \alpha}{1 + \frac{\tan \phi \tan \alpha}{F}} \right) \tan \phi \right\} dx
\end{aligned} \tag{B.12}$$

Since F is a constant parameter, we can write

$$\begin{aligned}
& \int_{x_i}^{x_f} \frac{1}{\cos \alpha} \left\{ \frac{c^* + [D - \frac{dX}{dx} + (1 + k_v) w] \tan \phi}{1 + \frac{\tan \phi \tan \alpha}{F_0}} \right\} dx \\
F = & \frac{\int_{x_i}^{x_f} \left(D + (1 + k_v) w \right) \sin \alpha dx + \frac{1}{R} \int_{x_i}^{x_f} [D \tan \beta (z_2 - z_0) - k_h w (z_B - z_0)] dx}{\int_{x_i}^{x_f} \frac{1}{\cos \alpha} \left\{ \frac{c^* + [D - \frac{dX}{dx} + (1 + k_v) w] \tan \phi}{1 + \frac{\tan \phi \tan \alpha}{F_0}} \right\} dx}
\end{aligned} \tag{B.13}$$

Bibliography

- R. Baker. A second look at Taylor's stability chart. *Journal of Geotechnical and Geoenvironmental engineering*, 129:1102–1108, 2003.
- R. Baker and Y. Tanaka. A convenient alternative representation of Taylor's stability chart. *Proc., Int. Symp. Slope Stability Eng.*, 1:253–257, 1999.
- J. M. Bell. Dimensionless parameters for homogeneous earth slopes. *J. Soil Mech. Found. Div., Am. Soc. Civ. Eng.*, 92:51–65, 1966.
- J. M. Bell. General slope stability analysis. *J. Soil Mech. and Found. Div.*, 94:1253–1270, 1968.
- A. W. Bishop. The use of slip circle in the stability analysis of earth slopes. *Geotéchnique*, 5:1, 1–7, 1955.
- A. W. Bishop and N. R. Morgenstern. Stability coefficient for earth slopes. *Geotéchnique*, 10:4, 129–147, 1955.
- E. D. Brekke. The tectonic evolution of the norwegian sea continental margin with emphasis on the Vøring and Møre basins. *Geol. Soc. Spec. Publ.*, 167:327–378, 2000.
- L. Broili. New knowledge on the geomorphology of the vaiont slide slip surfaces. *Rock Mechanics Eng. Geol., Jour. Int. Soc. Rock Mechanics.*, 5:38–88, 1967.
- H. Bungum. Seismotectonics on- and offshore in mid Norway, with emphasis on the correlation between mapped earthquakes and mapped faults. *29th Nordic Seminar on Detection Seismology*, 1998.

- M. Carli. Thesis of geological structural mapping and geoelectrical investigation of the North-Occidental portion of the Vajont landslide in the Venetian Prealps. *Dipartimento di Scienze Geologiche, Università degli Studi di Padova*, 2011.
- G. Carloni and R. Mazzanti. Aspetti geomorfologici della frana del Vaiont. *Riv. Geogr. It.*, 73:201–231, 1964.
- W. F. Chen, M. W. Giger, and H. Y Fang. On the limit analysis of stability of slopes. *Soils Found.*, 9:23–32, 1969.
- B. F. Cousins. Stability charts for simple earth slopes. *J. Geotech. Eng. Div., Am. Soc. Civ. Eng.*, 104:267–279, 1978.
- B. R. Crawford, D. R. Faulkner, and E. H. Rutter. Strength, porosity, and permeability development during hydrostatic and shear loading of synthetic quartz-clay fault gouge. *Journal of Geophysical Research*, 113, 2008.
- A.G. Doré, E.R. Lundin, L.N. Jensen, Ø. Birkeland, P.E. Eliassen, and C. Fichler. Principal tectonic events in the evolution of the northwest European Atlantic margin. *Petroleum Geology of Northwest Europe: Proceedings of the Fifth Conference*, 1: 41–61, 1999.
- S. M. Easa and A. R. Vatankhah. Explicit equation for safety factor of simple slopes. *IJRRAS*, 7:70–76, 2011.
- D. R. Faukker and E. H. Rutter. Comparisons of water and argon permeability in natural clay-bearing fault gouges under high pressure at 20° C. *Journal of Geophysical Research*, 105:16415–16426, 2000.
- W. Fellenius. Erdstatische Berechnungen mit Reibung und kohaesion und unter Annahme kreiszylindrischer Gleitflaechen [statistical analysis of earth slopes and retaining walls considering both friction and cohesion and assuming cylindrical sliding surfaces]. W. Ernst und Sohn, Berlin, 1927.
- W. Fellenius. Calculation of the stability of the earth dams. *Proceeding of the second congress of large dams*, 4:445–463, 1936.

- R. Francese, M. Giorgi, W. Bohm, A. Bondesan, A. Bistacchi, M. Massironi, and R. Genevois. Comprehensive 3d geophysical modelling of the Vajont landslides and of its surroundings. *Ital. J. Eng. Geol. and Envir.*, 6:555–565, 2013.
- D. G. Fredlund. Slope stability analysis. *Dept. of Civil Engineering*, 1974.
- D. G. Fredlund and J. Krahn. Comparison of slope stability methods of analysis. *Can. Geotech. Jour.*, 14:429–439, 1977.
- R. Genevois and Ghirotti M. The 1963 Vaiont Landslide. *Giornale di Geologia Applicata*, 1:41–53, 2005.
- M. Ghirotti. Nuovi dati sulla frana del Vaiont e modellazione numerica. *Geol Rom*, 30: 207–215, 1993.
- F: Giudici and E. Semenza. Studio geologico del serbatoio del Vajoint. *Unpublished report for S.A.D.E.*, 1960.
- A. J. Hendron and F. D. Patton. The Vaiont slide, a geotechnical analysis based on new geologic observations of the failure surface. I, II, Technical Report gl-85-5. *U.S. Army Eng. Waterways Experiment Station*, 1985.
- B. L. M. Highland and P. Bobrowsky. The landslide handbook — a guide to understanding landslides. *Reston, Virginia, U.S. Geological Survey*, Circular 1325, 2008.
- O. Hungr, S. Lerouelli, and L. Picarelli. The Varnes classification of landslides types, an update. *Landslides*, 2013. URL <http://dx.doi.org/10.1007/s10346-013-0436-y>.
- N. Janbu. Application of composite slip surface for stability analysis. *Proceeding of the European Conference on Stability of Earth Slopes*, 3:43–49, 1954.
- N. Janbu. Slope stability computations. embankment dam engineering. *Casagrande*, 1973.
- C. E. Johnson and L. K. Hutton. The 15 October, 1979 Imperial Valley, earthquake: a study of aftershocks and prior seismicity. *U.S. Geolog. Surv. Profess. Paper 1254*, pages 59–76, 1982.

- H. Kaneko, H. Tanaka, and Y. Kudoh. Slope stability consisting of two different layers caused by rainfall. Prediction and simulation methods for geohazard mitigation. *Murakami and Kimoto (eds.)*, 2009.
- J. Kim, S. Jeong, S. Park, and J. Sharma. Influence of rainfall-induced wetting on the stability of slopes in weathered soils. *Engineering Geology*, 75:251–262, 2004.
- S. G. Lee and M. H. De Freitas. A revision of the description and classification of weathered granite and its application to granites in Korea. *Quarterly Journal of Engineering Geology*, 22:31–48, 1989.
- J.S. L'Heureux, M. Vanneste, Rise L., Brendryen J., Forsberg C. F., O. Nadim F. and Longva, S. Chand, H. Hafliðason, and T. J. Kvalstov. Stability, mobility and failure mechanism for landslides at the upper continental slope off Vesterålen. *Marine Geology*, 346:192–207, 2013.
- M. Massironi, L. Superchi, D. Zampieri, A. Bistacchi, R. Ravagnan, A. Bergamo, M. Ghirotti, and R. Genevois. Geological structures of the Vajont landslide. *Ital. J. f Eng. Geol. and Envir.*, 6:573–582, 2013.
- R.L. Michalowski. Stability of uniformly reinforced slopes. *J. Geotech. Geoenviron. Eng.*, 125:84–86, 1999.
- R.L. Michalowski. Stability chart for uniform slopes. *J. Geotech. Geoenviron. Eng.*, 128:351–355, 2002.
- N. R. Morgenstern and V. E. Price. The analysis of the stability of general slip surface. *Geotechnique*, 15:79–83, 1965.
- N. R. Morgenstern and V. E. Price. A numerical method for solving the equations of stability of general slip surface. *Computer Journal*, 9:388–393, 1967.
- J. Mosar. Scandinavia's North Atlantic passive margin. *J. Geophys. Res.*, 108: doi:10.1029/2002JB002134, 2003.
- L. Müller. The rock slide in the Vaiont valley. *Felsmech. Ingenieurgeol.*, 2:148–212, 1964.

- L. Müller. New considerations on the Vaiont slide. *Rock Mech. Eng. Geol.*, 6:1–91, 1986.
- A. Nadai. Theory of flow and fracture of solids. *New York, McGraw-Hill Book Co.*, 1950.
- O. Olesen, E. Torsvik, T.H. and Tveten, K.B. Zwaan, T. Løseth, and T. Henningsen. Basement structure of the continental margin in Lofoten-Lopphavet area, northern Norway: constraints from potential field data, on-land structural mapping and palaeo-magnetic data. *Nor. Geol. Tidsskr.*, 77:15–30, 1997.
- M. A. Paparo. Sviluppo e applicazione di un codice numerico per l'analisi della stabilità dei versanti mediante il metodo dell'equilibrio limite. *Tesi di Laurea Magistrale*, 2010.
- M. A. Paparo and S. Tinti. Sensitivity analysis and stability charts for uniform slopes computed via the MLD method in the frame of the limit equilibrium theory. *EGU General Assembly 2013*, 2013.
- M. A. Paparo, F. Zaniboni, and S. Tinti. The Vajont landslide, 9th october 1963: limit equilibrium model for slope stability analysis through the minimum lithostatic deviation method. *Ital. J. f Eng. Geol. and Envir.*, 6:583–592, 2013.
- Van De Reep. Permeability of limestone-dolomite composite fracture surfaces. *Honour Thesis*, 2009.
- D. Rossi and E. Semenza. Carte geologiche del versante settentrionale del M. Toc e zone limitrofe, prima e dopo il fenomeno di scivolamento del 9 ottobre 1963, scala 1:5000. *Istituto di Geologia, Università di Ferrara*, 1965.
- S.K. Sarma. Stability analysis of embankments and slopes. *Géotechnique*, 37:107–111, 1987.
- E. Semenza. Sintesi degli studi geologici sulla frana del Vajont dal 1959 al 1964. *Memorie del Museo Tridentino di Scienze Naturali*, 16:1–52, 1965.

- E. Semenza and M. Ghirotti. History of 1963 Vaiont slide. the importance of the geological factors to recognise the ancient landslide. *Bull. Eng. Geol. Env.*, 59:87–97, 2000.
- A. Singh. Shear strength and stability of man-made slopes. *J. Soil Mech. Found. Div., Am. Soc. Civ. Eng.*, 96:1879–1892, 1970.
- E. Spencer. A method of analysis of the stability of embankments assuming parallel inter-slice forces. *Géotechnique*, 17:11–26, 1967.
- M. Talwani and O. Eldholm. Evolution of the Norwegian-Greenland sea. *Geological Society of America Bulletin*, 83:969–999, 1977.
- N. M. Tanpure and S. S. S. Koranne. Use of graphical technique for stability analysis of embankment. *J. Mech. Civ. Eng.*, 3:1–10, 2012.
- D. W. Taylor. Stability of earth slopes. *J. Boston Soc. Civil Eng.*, 24:337–386, 1937.
- S. Tinti and A. Manucci. Gravitational stability computed through the limit equilibrium method revisited. *Geophys. J. Int.*, 164:1–4, 2006.
- S. Tinti and A. Manucci. A new computational method based on the minimum lithostatic deviation (MLD) principle to analyse slope stability in the frame of the 2D limit-equilibrium theory. *NHESS*, 8:671–683, 2008.
- D. J. Varnes. Landslide types and processes. *Eckel EB (ed) Landslides and engineering practice, Special Report 28*, 1954.
- D. J. Varnes. Slope movement types and processes. *Schuster RL, Krizek RJ (eds) Landslides, analysis and control, special report 176: Transportation research board, National Academy of Sciences, Washington, DC.*, 1978.
- F. Zaniboni and S. Tinti. Numerical simulations of the 1963 Vajont Landslide, Italy: Application of 1D Lagrangian Modelling. *Natural Hazards*, 70:567–592, 2014.
- F. Zaniboni, M. A. Paparo, and S. Tinti. The 1963 Vajont landslide analysed through numerical modeling. *Ital. J. f Eng. Geol. and Envir.*, 6:623–632, 2013.

Acknowledgements

This work would not have been possible without the help and encouragement of many people and I would like to express my thanks to them. First of all I would like to thank my supervisor Professor Stefano Tinti. I am particularly grateful for his assistance and advice given during the planning and development of this research work.

I express my sincere appreciation for the hospitality and learning opportunities to the Norwegian Geotechnical Institute of Oslo. A special thanks to Dr. Carl B. Harbitz for his support, for his time and for the experience I had at the NGI, for what I learned, for the people I met.

In addition I would thank for his kindness Dr. Luigi Migliaccio, executive director of the Casa Editrice Università La Sapienza, who authorized the inclusion of parts of my paper on the Vajont case.

I have a great debt of gratitude to my colleagues and coworkers in the University of Bologna: Alberto, Filippo, Gianluca, Lidia and Katharina.

Un immenso grazie alla mia famiglia, in particolare ai miei genitori e a mio fratello, che da lontano hanno supportato e sopportato questa lunga esperienza. Ai miei nonni, a chi mi incoraggia ogni giorno e a chi invece mi protegge dall'alto. A Franca e Lino che mi hanno accolto come una figlia.

A Lara, alla mia miciona Leila, a tutti quei poveri ragazzi da me arbitrati a cui devo dire grazie per le fantastiche domeniche passate sotto la pioggia, fango o sole cocente. Al gruppo arbitrale dell'Emilia Romagna. A Morena, Noemi, Maria, Riccardo, Mario, Annamaria, Merianna, Ramona, Nunzio, Federica, Rosa, Franco, Celeste, Francesca, Alessandra, Antonio, Erika, Giuseppe, Giulia, Sara, Elmenr, Alberto, Fausto, Elia, Mirco, Andrea, Stefano, Giovanni, Kursat, Erjona, Valentina, Julie, Letizia, Tommy.

E alla fine ringrazio la persona più importante della mia vita, Fabrizio.